Performance of the ATLAS Hadronic Endcap Calorimeter Modules to Electrons and Pions

by

Dominique Fortin

B.Sc., McGill University, 1998

A Dissertation Submitted in Partial Fulfillment of the
Requirements for the Degree of

MASTER OF SCIENCE

in the Department of Physics and Astronomy.

We accept this dissertation as conforming
to the required standard.

Dr. M Lefebvre, Supervisor (Dept. of Physics and Astronomy)

Dr. R. Keeler, Departmental Member (Dept. of Physics and Astronomy)

Dr. R. Kowalewski, Departmental Member (Dept. of Physics and Astronomy)

Dr. P. Wan, Outside Member (Dept. of Chemistry)

Dr. D. Axen, External Examiner (Dept.‘ of Physics and Astronomy, UBC)

© Dominique Fortin, 2000
University of Victoria

All rights reserved. This dissertation may not be reproduced in whole or in part,

by photocopying or other means, without the permission of the author.

Supervisor: Dr. M. Lefebvre

ABSTRACT

During the summer of 1999, the first six production modules of the Hadronic Endcap Calorimeter were assembled and installed in a beam test cryostat at CERN. In this thesis, the performance of the calorimeter is assessed in terms of its response and resolution to electrons and pions. The calorimeter is evaluated at five impact points and over an energy range of 10 to 200 GeV. The linearity of the response to electrons is observed to be within approximately one percent, and the average electromagnetic scale constant is measured to be $\alpha_{em} = (3.82 \pm 0.04)$ GeV/nA. The intrinsic energy resolution (not including the electronic noise) obtained is $\frac{\sigma}{E} = \frac{(23.29 \pm 0.09)\%}{\sqrt{E_0(\mathrm{GeV})}} \oplus (0.00 \pm 0.13)\%$ for electrons, and $\frac{\sigma}{E} = \frac{(76.2 \pm 09)\%}{\sqrt{E_0(\mathrm{GeV})}} \oplus (6.68 \pm 0.09)\%$ for pions, where E_0 is the incident particle energy. Comparison with Monte Carlo simulations and the effect of the electronics calibration procedure are discussed. Finally, the ratio of electromagnetic to hadronic response, e/h, is measured to be $e/h = (1.509 \pm 0.021)$.

Examiners:

Dr. M. Lefebvre, Supervisor (Department of Physics and Astronomy)

Dr. R. Keeler, Departmental Member (Department of Physics and Astronomy)

Dr. R. Kowalewski, Departmental Member (Department of Physics and Astronomy)

Dr. P. Wan, Outside Member (Department of Chemistry)

Dr. D. Axen, External examiner (Department of Physics and Astronomy, UBC)

Contents

Abstract **ii**

Table of Contents **iii**

List of Figures **vi**

List of Tables **viii**

Acknowledgments **ix**

Dedication **x**

1 Introduction **1**

2 The ATLAS experiment at the LHC **4**

2.1 The Large Hadron Collider 4

2.2 The ATLAS experiment 6

2.2.1 Goals 6

2.2.2 Overview of the detector 7

2.2.3 The ATLAS calorimetry system 8

3 The ATLAS Hadronic Endcap Calorimeter **11**

3.1 Principle of calorimetry 11

3.1.1 Electromagnetic showers 11

3.1.2 Hadronic showers 13

3.1.3 Sampling calorimetry 15

3.1.4 Liquid argon calorimetry 17

3.1.5 Resolution 18

3.2 Design 19

3.2.1 Copper plate absorbers 19
3.2.2 The liquid argon gaps 21
3.2.3 Performance goals 22

4 Beam Tests 23

4.1 Setup 24
4.1.1 Modules layout 24
4.1.2 Trigger system 26
4.1.3 Readout and calibration 28
4.1.4 Beam production 30
4.2 Signal reconstruction 31
4.2.1 Pedestal computation 34
4.2.2 Digital filtering 34
4.3 Electronic noise 36
4.4 Monte Carlo simulation 43
4.4.1 Electron simulation 43
4.4.2 Pion simulation 44

5 Analysis of Electron Beam Test Data 45

5.1 Trigger cuts 46
5.2 Clustering 46
5.3 Response and α_{em} constant 48
5.4 Beam contamination 52
5.5 Resolution 56
5.6 Uniformity 61

6 Analysis of Pion Beam Test Data 65

6.1 Trigger cuts 65
6.2 Clustering 66
6.3 Response 68

6.4 Resolution 71
6.5 Determination of e/h 74

7 Conclusions **81**

Bibliography 83

A The Elementary Particles **87**

B Layout Geometry of the HEC Readout Cells **89**

C Error Analysis for the Intrinsic Energy Resolution **92**

List of Figures

2.1 The injector complex and the LHC ring 5
2.2 The ATLAS detector 9
2.3 The ATLAS calorimetry system 10

3.1 Fractional energy loss for electrons interacting in lead. 12
3.2 Schematic drawing of a liquid argon (LAr) ionization chamber. 18
3.3 Three dimensional view of the HEC 20
3.4 The liquid argon gaps structure 21

4.1 Geometric layout of the readout cells (z=1) 25
4.2 Pointing geometry of the HEC 26
4.3 Setup of the HEC beam tests. 27
4.4 HEC beam test electronic chain 29
4.5 Average signal shape for a readout cell 32
4.6 Comparison between pedestals computed from physics and random events 35
4.7 Example of electronic noise distribution in readout cells 37
4.8 Electronic noise distribution for a cluster 38
4.9 Electronic noise vs reconstructed energy for a cluster 39
4.10 Cluster electronic noise and most probable current for all electron runs 41
4.11 Cluster electronic noise and most probable current for all pion runs . 42

5.1 Layout of a cluster designed for electron runs. 47
5.2 HEC response for various electron energies. 49

5.3 Relative energy response to electrons vs beam energy 50
5.4 Pion energy distribution using an electron cluster 53
5.5 Electron energy distribution using a function for the pion contamination 54
5.6 147.8 GeV electron energy distribution 55
5.7 Electron energy resolution for the 5 impact points studied 56
5.8 Electron intrinsic resolution for the 5 impact points studied 58
5.9 Combined electron intrinsic resolution vs beam energy at impact points F, G and H 59
5.10 Spatial uniformity of the response (X-scan) 62
5.11 Two cell cluster response 63
5.12 Spatial uniformity of the response (Y-scan) 64

6.1 Layout of a cluster designed for pion runs. 67
6.2 HEC response for various pion energies 69
6.3 Relative energy response vs pion beam energy 70
6.4 Pion energy resolution vs beam energy for the 5 impact points studied 71
6.5 Pion intrinsic resolution vs beam energy at the 5 impact points studied 73
6.6 Combined pion intrinsic resolution vs beam energy at impacts B and C 75
6.7 Combined pion intrinsic resolution vs beam energy at impacts F, G and H 76
6.8 Energy dependence of e/π *before* energy leakage corrections 77
6.9 Energy dependence of e/π *after* energy leakage corrections 79
6.10 Individual measurements of e/h *after* energy leakage corrections . . . 79

B.1 Geometric layout of the readout cells for the second depth of the front wheel modules (z=2) 90
B.2 Geometric layout of the readout cells of the rear wheel modules . . . 91

List of Tables

4.1 Electromagnetic depth weights 33
4.2 High voltage correction factors 34

5.1 Electromagnetic scale constant for the 5 studied impact points 51
5.2 Electron resolution parameters for the 5 impact points studied 60

6.1 Pion resolution parameters for the 5 impact points studied 74
6.2 Evaluation of e/h with and without energy leakage corrections 78

A.1 The three fermion families. 87
A.2 The vector gauge bosons. 88

Acknowledgments

This thesis would not have been possible without the help of a number of people. First of all, I would like to thank Christopher Oram for taking me as a summer student at TRIUMF, and for the good advices about graduate studies. This was probably the most determining event in my career.

I would like to thank my supervisor, Michel Lefebvre, for the opportunity he gave me to work at CERN, for all the things I have learnt while being a member of the ATLAS-HEC Collaboration, and for the numerous hours he spent proofreading this work. I would also like to thank Richard Keeler and Robert Kowalewski, for the time they spent on this thesis and for their insights.

I would also like to thank my collegues of the ATLAS-HEC Collaboration who have helped me in the analysis and understanding of the beam tests: Andrei Kiryunin, Leonid Kurchaninov, Andrei Minaenko, Peter Schacht, Hasko Stenzel and Pavol Strizenec.

Many thanks to Dugan O'Neil and Matt Dobbs for helping me in debugging Fortran codes, writing kumacs, and for all the useful conversations. Dugan, you were really busy finishing your thesis during fall 1999, but you were kind enough to spend lots of time helping me. You have been like a second supervisor to me. Matt, thank you for the time we have spent together at CERN and around Geneva. These are good memories.

Thank you Angela for the wonderful year we have spent together. Thank you for your understanding, your support and your love.

Jack, I wouldn't have made it without you. Thank you for your friendship. Sometimes things went wrong but you were always there for me.

A Jacques et Martine, mes parents...

Chapter 1

Introduction

In an effort to explain all the phenomena of particle physics, three theories were united in what is now referred to as the Standard Model (SM). It describes all of the known fundamental particles and their interactions via three of the four forces: electromagnetism, the weak and the strong forces. Quantum Electrodynamics (QED) was the first theory developed and describes electromagnetic phenomena. Later, in the late 1960's, the weak and electromagnetic interactions were unified in the theory of electroweak interactions proposed by Glashow, Weinberg and Salam [1-3]. The Glashow-Weinberg-Salam (GWS) theory incorporates QED processes and provides a description of the weak force through the exchange of massive vector bosons. The third theory, Quantum Chromodynamics (QCD), describes the interactions of quarks through the strong "colour" field. Gravity is by far the weakest of the four forces, and is not part of the Standard Model.

There are three types of elementary particles in the SM: the spin-$\frac{1}{2}$ fermions (leptons and quarks) that constitute all matter, the spin-1 gauge bosons that mediate the three forces, and the spin-0 Higgs boson. The electroweak force acts on all of the 12 fermions [1], via the exchange of vector gauge bosons (γ, $W^{\pm}$, Z^0). The strong force is mediated by the exchange of coloured gluons, which bind quarks to produce colourless particles called hadrons. In the SM, the masses of the fermions and gauge bosons are generated after spontaneous symmetry breaking of the vacuum via the

[1] and their antiparticles (see Appendix A).

Higgs mechanism, producing a massive neutral scalar Higgs boson [2-3].

Today, no experimental result has been conclusively shown to disagree with the predictions of the Standard Model. With the discoveries of the $W^{\pm}$ [4] [5] and Z^0 [6] [7] bosons at their expected masses in 1983 at CERN [2], and of the top quark in 1995 [8] by CDF [3], the Higgs boson is the only remaining particle of the SM which has not been found. High energy hadron colliders which have center of mass energies in the multi-TeV range, such as the LHC [4], have the best potential for future discovery.

The ATLAS [5] experiment [9] [10] is one of the two multipurpose experiments at the LHC. It has been designed to detect the high energy decay products of the LHC's proton-proton collisions. The ATLAS detector is made up of several sub-detectors, each optimized to measure specific quantities. Canada is heavily involved in the ATLAS calorimetry system, including the design and construction of the Hadronic Endcap Calorimeter (HEC). In 1996, the first prototype of the HEC was tested in particle beams at CERN. Since then, the ATLAS group at the University of Victoria has been involved in the monitoring and analysis of the beam test data.

The goal of this work is to assess the performance of the first 6 production modules of the HEC in terms of their energy response and resolution to electrons and pions through an analysis of the 1999 beam test data. In order to cover the experiment, the physical processes involved and the techniques used for the analysis, this work has been divided in six Chapters. A short overview of the LHC and of the ATLAS experiment is made in Chapter 2. Chapter 3 reviews the principles of calorimetry and describes the Hadronic Endcap Calorimeter. The beam test experimental setup, the energy reconstruction procedure, the electronic noise and the simulation of events are described in Chapter 4. Chapters 5 and 6 present the

[2] CERN (the Centre Européen de Recherche Nucléaire) is the largest particle physics research facility in the world, and is located in Geneva, Switzerland.

[3] The CDF detector (Collider Detector at Fermilab) is a multipurpose detector used to exploit the Tevatron's proton-antiproton collider at Fermilab, near Chicago (Illinois).

[4] The LHC (Large Hadron Collider) is a proton-proton collider with 14 TeV center of mass energy under construction at CERN.

[5] A ToroidaL ApparatuS.

results obtained for electron and pion beams respectively, along with comparisons with Monte Carlo simulations. The conclusion summarizes the most important results.

Chapter 2

The ATLAS experiment at the LHC

The Large Hadron Collider (LHC) is now under construction at CERN. It will achieve higher collision energy and luminosity than any existing accelerators [11]. ATLAS is one of the two multipurpose experiments making use of the LHC. In this chapter, an overview of the LHC is presented, followed by a brief description of the ATLAS experiment, with emphasis on the calorimetry system.

2.1 The Large Hadron Collider

In December 1994, delegates representing the 19 member states of CERN unanimously approved the construction of the Large Hadron Collider. The LHC will be installed in CERN's existing 27-kilometer circular tunnel built for the Large Electron-Positron (LEP) collider. Constructed from more than one thousand 8.5 T superconducting magnets, the LHC will achieve proton-proton collisions at a center of mass energy of $\sqrt{s} = 14$ TeV with beams of unsurpassed brightness, recreating conditions which prevailed in the universe only 10^{-12} seconds after the Big Bang. The LHC will be filled with protons delivered from the SPS [1] and its pre-accelerators at 450 GeV (see Figure 2.1). Two superconducting magnetic channels will accelerate the protons to 7-on-7 TeV, after which the beams will counter-rotate for several hours, colliding at the experiments, until the beam degradation is such that the

[1] Super Proton Synchrotron.

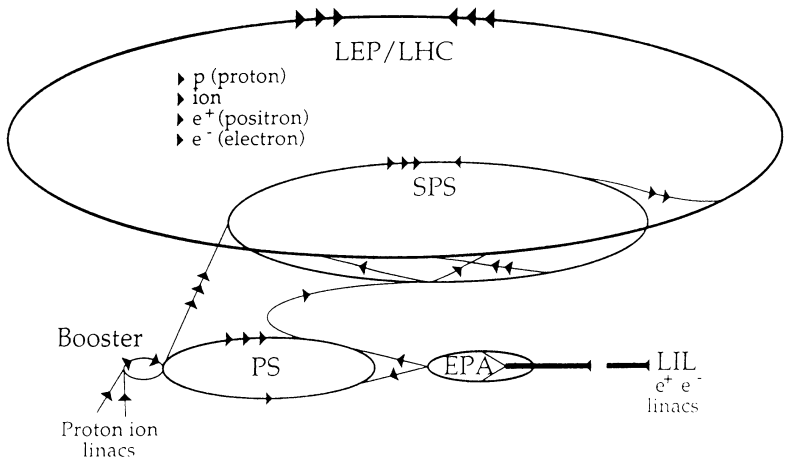

Figure 2.1: The LHC injector complex and main LHC ring are pictured here. The energies of each injection stage are as follows: linacs (50 MeV), PS booster (1.4 GeV), PS (26 GeV), SPS (450 GeV).

machine has to be emptied and refilled [12].

The use of protons as projectiles will offer several advantages over electrons and antiprotons. First, the synchrotron radiation losses for protons are much less than for electrons of the same energy [13]. Furthermore, protons are easier to produce than antiprotons and at high energies, the cross sections for pp and $p\overline{p}$ collisions are equal. Finally, the nature of the collisions in a hadron collider offers an excellent discovery potential. At high energies, the proton momentum is split between gluons and quarks which allow for a diverse spectrum of center of mass energies of proton constituent collisions.

Point-like cross sections decrease as $1/s$, and hence become very small at high energy. Therefore, it is necessary to examine a very large number of collisions in order to detect rare high energy processes. This requires an extremely high potential particle collision rate, or luminosity [2], in order to produce enough events of interest in a reasonable time (a few years of operation). The LHC has thus been designed to run with a luminosity of $10^{34}\mathrm{cm}^{-2}\mathrm{s}^{-1}$.

The LHC experimental programme is composed of two large multipurpose detec-

[2]The luminosity is defined as the rate of particles per unit area.

tors: ATLAS and CMS [3] [14]. Two other detectors will make use of the accelerator: LHC-B [4] [15] dedicated to B-physics, and ALICE [5] [16], which will study the collisions of heavy ions. The calorimeter modules studied in this work are part of the Hadronic Endcap Calorimeter of the ATLAS detector.

2.2 The ATLAS experiment

The ATLAS project was formally approved by CERN in January 1996. More than 1850 physicists from 34 countries are taking part in the design and building of the ATLAS detector [6]. In the following sections, the main goals of this experiment are presented. A short overview of the detector is made, with emphasis on the calorimetry system.

2.2.1 Goals

The ATLAS detector is designed to exploit the full discovery potential of the Large Hadron Collider. Several goals have been defined [9], the main one being the understanding of the mechanism of electroweak symmetry breaking. This goal guided the detector design. The desire to probe the origin of the electroweak scale led to a major focus on the Higgs boson; ATLAS was designed to be sensitive to it over the full range of allowed masses. The investigation of CP violation in B decays and the precision measurements of W and top-quark masses and triple gauge boson couplings are also important components of the ATLAS physics programme. ATLAS will also offer the opportunity to search for other phenomena possibly related to symmetry breaking, such as particles predicted by supersymmetric or technicolour theories, as well as new gauge bosons and evidence for composite quarks and leptons [17].

[3] Compact Muon Solenoid experiment.

[4] The LHC-B (Large Hadron Collider Beauty) detector is a forward collider detector dedicated to the study of CP violation and other rare phenomena in the decays of Beauty particles.

[5] A Large Ion Collider Experiment.

[6] In September 2000.

2.2.2 Overview of the detector

In order to maximize the chance of observing new physics, ATLAS is designed to operate at high luminosity with sensitivity to as many different physics signatures as possible (e, μ, γ, jet [7], E_T^{miss} [8], b-tagging...). The LHC's 25 ns bunch crossing necessitates fast signal readout, and the detector must be resistant to a high radiation environment, especially in the forward regions.

An ideal detector would reconstruct the 4 momentum $(E, \vec{p})$ of, and identify all particles produced in every event. Hence, the ATLAS detector is composed of several sub-detectors, each optimized to detect various aspects of a collision event. They are grouped in three main systems:

- The inner detector (tracker) measures the path and the momentum $(\vec{p})$ of charged particles, and also locates vertices;
- The calorimetry system measures the energy of electrons, photons and pions, while providing particle identification and direction. It is also sensitive to muon energy loss;
- The muon spectrometer identifies and measures the momentum $(\vec{p})$ of muons.

Figure 2.2 shows the location of these systems, and displays the familiar tracker-calorimeter-muon chamber onion skin configuration. The magnet system is also presented, and consists of outer super-conducting air-core toroids (4.2 T peak field), complemented by an inner super-conducting solenoid, which produces a magnetic field of 2 T. The ATLAS detector must be large to measure high energy particles: it is approximately 30 m long by 22 m in diameter (making ATLAS about the same height as an 8 story building), and has a total weight of 7000 tons.

An in-depth description of the different systems and sub-detectors is presented in [18]. The calorimetry system is of interest and will be described in more detail in

[7] A jet is composed of highly collimated secondary particles observed in the detector.

[8] E_T^{miss} is the transverse missing energy, the magnitude of the component of the total event momentum vector that is a perpendicular to the beam axis.

the following section.

2.2.3 The ATLAS calorimetry system

Many important physics processes require the identification and reconstruction of the energy of electrons, photons and jets as well as a measurement of the missing transverse energy (E_T^{miss}). The ATLAS calorimetry system is designed to meet these requirements in the very high luminosity environment of the LHC, with an acceptance covering the region $|\eta| < 4.9$ in pseudorapidity [9]. The calorimeters will also provide fast signals used to decide whether to read out the detector or not, a process known as triggering.

Liquid argon technology was chosen for the regions of the calorimetry system closest to the beam, mainly due to its fast signal readout capabilities, radiation hardness, and ease of calibration. It is used for all of the electromagnetic calorimeters, and the hadronic endcap and forward calorimeters. The principle of liquid argon calorimetry, and the design of the Hadronic Endcap Calorimeter is presented in Chapter 3. The large barrel hadronic calorimeter uses scintillating tiles as the active material. Detailed designs of the calorimeters are available in the ATLAS Liquid Argon Technical Design Report [19], and in the ATLAS Tile Calorimeter Technical Design Report [20]. The layout of the calorimetry system is presented in Figure 2.3.

[9] The pseudorapidity (η) is defined as $\eta = -\ln(\tan\frac{\theta}{2})$, where θ is the polar angle measured from the beam axis.

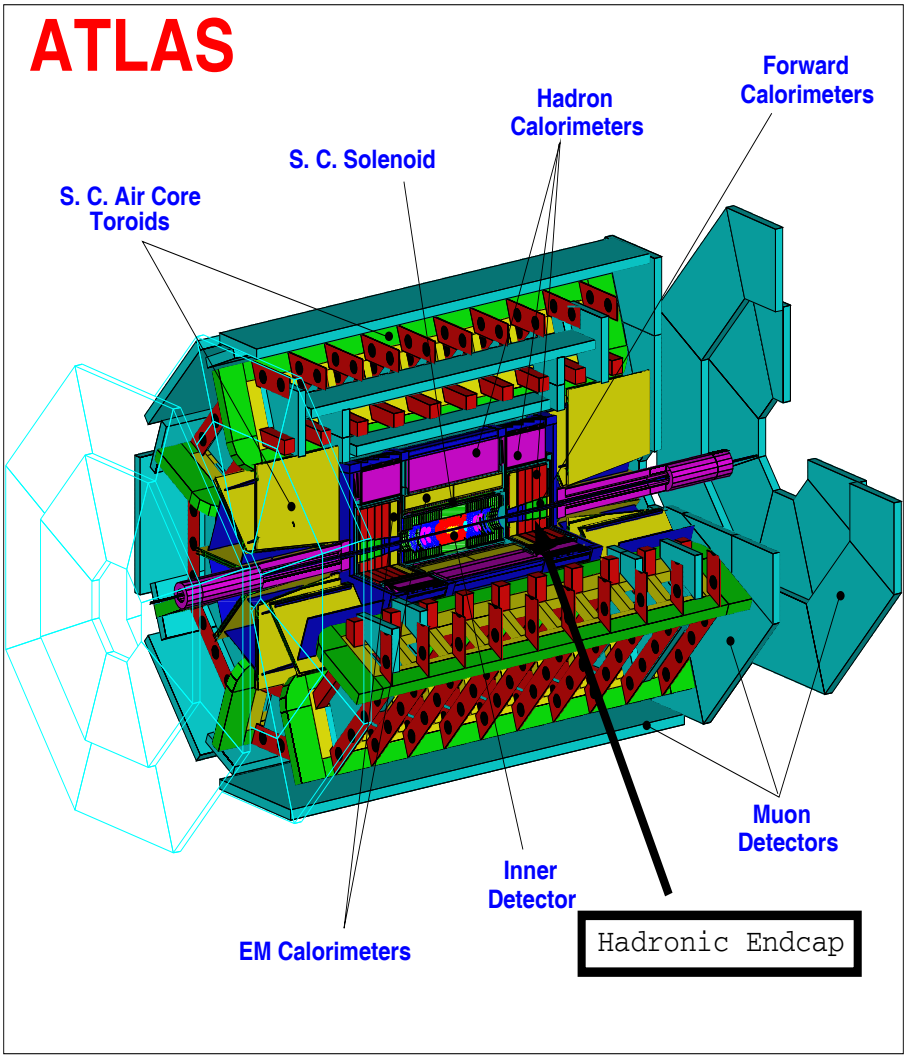

Figure 2.2: Layout of the ATLAS detector. The dimensions of the detector are of approximately 30 m in length by 22 m in diameter. The location of the Hadronic Endcap Calorimeter is also indicated.

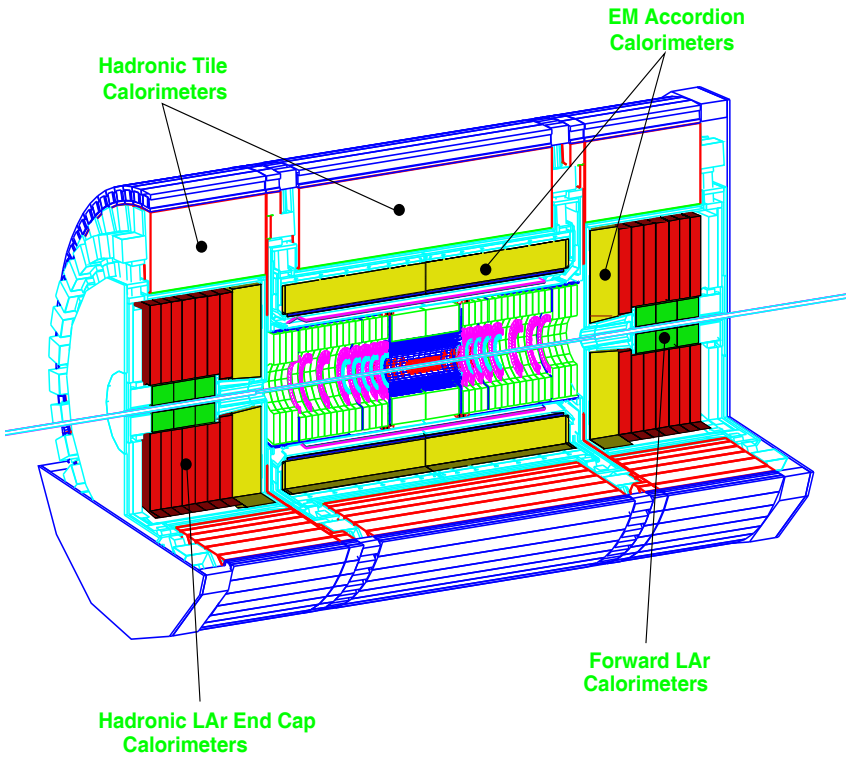

Figure 2.3: Three dimensional view of the ATLAS calorimetry system. The total length of the system is about 13 m and has a radius of 8 m.

Chapter 3

The ATLAS Hadronic Endcap Calorimeter

Calorimeters are of great importance in modern high energy physics experiments. In this chapter, the physical processes and techiques used in calorimetry are reviewed, followed by a detailed presentation of the ATLAS Hadronic Endcap Calorimeter.

3.1 Principle of calorimetry

In high energy physics, particles lose energy in matter through various mechanisms, mediated by the electromagnetic, strong or weak force. A calorimeter is a device that absorbs this energy and produces a signal proportional to it. In the following sections, the electromagnetic and hadronic processes of energy deposition in matter are presented. The principle of liquid argon and sampling calorimetry is then reviewed, followed by a discussion of the calorimeter resolution.

3.1.1 Electromagnetic showers

The energy loss of an electron (or positron) incident on a block of matter depends on the electron's initial energy. As shown in Figure 3.1, the dominant interaction for electrons with energy above 10 MeV in dense matter is Bremsstrahlung. In this process, the incident electron interacts with the coulomb field of a nucleus of charge Ze, and by scattering emits an energetic photon (E_γ). If this photon has sufficient energy (above 10 MeV), it will interact with the electromagnetic field of a nucleus or

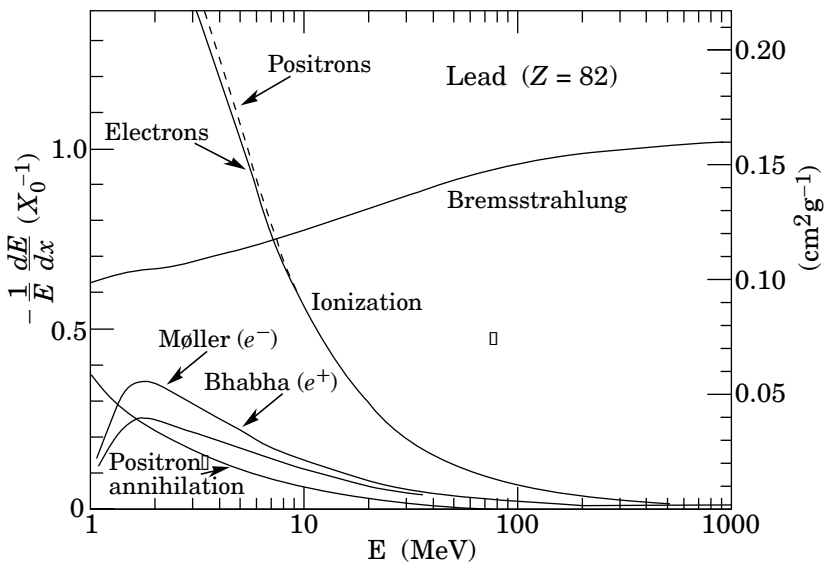

Figure 3.1: Fractional energy loss per radiation length for electrons interacting in lead [21].

electron and produce an e^+e^- pair. Both the e^+ and e^- may be capable of emitting a photon via bremsstrahlung. Thus, a cascade of particles can be produced by a single electron traveling through matter. This phenomenon is known as an electromagnetic shower.

Throughout this showering process, the energy of the original electron is lost. It is therefore useful to measure material thicknesses in units of radiation length X_0, the mean distance over which the impinging electron's energy is reduced to $1/e$ of its initial value by radiation loss [1]. This important parameter is dependent on the density of the material used and can be approximated by

$$X_0 = \frac{716.4A}{Z(Z+1)\ \ln(287/\sqrt{Z})}\text{g/cm}^2, \tag{3.1}$$

where Z is the atomic number, and A is the atomic mass of the absorbing material. This expression yields $X_0 = 1.43$ cm for copper, and $X_0 = 14$ cm for liquid argon [21]. For photons, this characteristic attenuation length is slightly different, and is referred to as the absorption length $X_p = \frac{9}{7}X_0$.

[1] In other words, $E(x) = E_0 e^{-\frac{x}{X_0}}$.

Energy loss by bremsstrahlung dominates until the energy of the electrons drops to a threshold called the critical energy (ϵ_c). At this point, the energy loss via ionization becomes equal to the energy loss via bremsstrahlung. This energy threshold can be found by applying the following empirical law [22]:

$$\epsilon_c = \frac{800 \text{ MeV}}{Z + 1.2}. \tag{3.2}$$

Below ϵ_c, ionization mostly dominates, and the shower dies. The rate of energy loss by this mechanism, for a particle of mass M and charge ze, is given by the Bethe-Bloch equation [23]

$$\frac{dE}{dx} = \frac{4\pi N_0 z^2 e^4}{m\beta^2}\frac{Z}{A}\left[\ln\left(\frac{2m\beta^2}{I(I-\beta^2)}\right) - \beta^2\right], \tag{3.3}$$

where m is the electron mass and β is the velocity of the particle. N_0 is Avogadro's number, Z and A are the atomic number and weight of the atoms in the medium, x is the path length multiplied by the density of the medium and E is the energy loss. Finally, I is the global ionization potential and is approximatively given by $10Z$ eV.

The transverse spread of the electromagnetic shower also needs to be considered. It is characterized by the Molière Radius which is defined as

$$R_m = \frac{21\text{MeV}}{E_c} X_0 \tag{3.4}$$

where E_c is the Rossi critical energy [2] and X_o is the radiation length. About 95% of a shower is contained laterally in a cylinder of radius 2 R_m [24].

3.1.2 Hadronic showers

Hadronic showers can be generated when baryons and mesons interact in matter via the strong force. Although hadronic showers are qualitatively similar to electromagnetic ones, their shower development is far more complex because many different processes contribute to the inelastic production of secondary hadrons [3]. No simple analytical description exists, however the elementary processes have been well studied.

[2] Rossi defined the critical energy as the energy at which the ionization loss per radiation length is equal to the electron energy. It is approximately the same as ϵ_c.

[3] Over 300 reactions have been observed with branching ratio of 0.1% or more.

Typically, about half of the available energy in hadronic cascades is spent in multiple particle production with transverse momentum $< p_T > \approx 0.35$ GeV/c. The remainder of the energy is carried by fast, forward-going particles [25]. These secondary particles are mostly pions and nucleons.

A considerable fraction of these secondaries are neutral pions (π^0). Electromagnetic subshowers can thus be formed since π^0 decay almost exclusively to two photons [4] [21]. Wigmans [26] has parameterized this electromagnetic fraction as

$$f_{\pi^0} \approx 0.11 \ln E(\mathrm{GeV}), \tag{3.5}$$

for energies in the range of a few to several hundred GeV. In other words, an incident 10 GeV $\pi^{\pm}$ would produce a hadronic shower with a fractional electromagnetic component of $f_{\pi^0} \approx 25\%$, whereas for a 200 GeV $\pi^{\pm}$, $f_{\pi^0} \approx 58\%$. This transfer of energy from the hadronic to the electromagnetic sector is a one-way process; the decay products of π^0 will not start new hadronic showers.

No precise model exists to describe the purely hadronic part of hadronic shower. Nonetheless, phenomenological descriptions have been developed, such as the spallation model. In this model, the hadronic cascade is seen as the break-up (spallation) of nuclei by fast hadrons transferring some of their momentum to the nucleons within the nucleus. Additional hadrons (mostly pions) are thus produced. The ejected nucleons or nuclear fragments eventually scatter off other nuclei and may cause further breaking-ups. This process is known as fast intra-nuclear cascade. Following this rapid stage of the shower, excited nuclei return to their ground state. This slow phase of nuclear de-excitation consists of nuclei emitting nucleons and photons through successive evaporation steps, until the excitation energy is less than the binding energy of one nucleon.

The scale of the hadronic shower is determined by the nuclear interaction length (λ_I) defined as

$$\lambda_I \approx \frac{35\ A^{1/3}}{\rho\ (\mathrm{g/cm^3})}\ \mathrm{cm}, \tag{3.6}$$

[4] $(99.798 \pm 0.032)\%$ of the time.

where ρ is the density of the material and A its nuclear mass. It represents the mean free path of high energy neutrons between two inelastic interactions in matter. For copper $\lambda_I = 15.1$ cm, and for liquid argon, $\lambda_I = 97.3$ cm. The depth necessary for shower containment scales logarithmically with energy. As a general rule, 95% of the total energy of a hadronic shower is contained longitudinally within a depth of about [28]

$$L(95\%) \approx 2.5\ [0.54 \ln E(\mathrm{GeV}) + 0.4]\ \lambda_I, \tag{3.7}$$

expressed in units of λ_I. Therefore, a shower initiated by an incident 200 GeV hadron on a block of matter should leave 95% of its energy, on average, after traveling through 8.15 λ_I, or 1.23 m in the case of copper.

As mentioned above, typical hadronic showers have $< p_T > \approx 0.35$ GeV/c, which is roughly independent of energy. Approximately 95% of the shower energy is contained in a cylinder of radius λ_I. However, large fluctuations in the lateral spread of hadronic showers have been observed.

The fraction of energy dissipated in electromagnetic subshowers and in the purely hadronic showers formed by a given impinging hadron varies significantly. This leads to very different shower compositions, and corresponding detector responses. This shower component variation can intrinsically limit the performance of hadronic calorimeters.

3.1.3 Sampling calorimetry

A calorimeter can be considered as a block of matter which intercepts a primary particle and causes it to shower. If the block is of sufficient thickness, the cascade of increasingly lower-energy particles eventually stops within the detector, meaning that all of the primary particle energy is dissipated inside the calorimeter. This energy appears mostly in the form of heat. A fraction of this deposited energy (usually very small) can be collected, for example, in the form of Cherenkov light [5]

[5] Cherenkov light is produced in a medium of refractive index n when a charged particle traverses the material with a velocity greater than the speed of light ($v > \frac{c}{n}$). The excited atoms in the vicinity of the particle become polarized and part of the excitation energy reappears as coherent

or ionization charge, which are often the most practical signals. Whereas most other subdetectors are restrained to the detection of charged particles using a magnetic field, calorimeters offer the opportunity to detect neutral particles. Also, the length of calorimeters needs to increase logarithmically with energy, whereas in the case of magnetic spectrometer it increases as $p^{1/2}$. This difference gives calorimeters an increasing advantage over magnetic spectrometers as particle colliders achieve higher energies. The segmentation of calorimeters also allows the determination of the location, angle, and energy of particles entering the detector.

Calorimeters can be divided in two types: total absorption and sampling calorimeters. Since the Hadronic Endcap is of the second type, only sampling calorimetry will be discussed further.

Sampling calorimeters are designed to exploit the properties of electromagnetic and hadronic showers. These detectors are divided in alternating layers of absorbing and active medium. Independent measurements (samples) of the shower are taken throughout its development in each layer of active medium (such as an ionizing liquid/gas or scintillating medium). In other words, only a fraction of the shower energy is sampled. The absorber is responsible for producing showers and enabling the full containment of the showers. It is usually a high-Z material (EM calorimeter), or a dense material with a small interaction length (hadronic calorimeter).

Two important aspects have to be considered in the design of calorimeters: sampling frequency and sampling fraction. These characteristics relate to the number of samples per unit depth, and the ratio of the energy deposited in the active/absorbing media, respectively. In general, a higher sampling frequency and sampling fraction improve the intrinsic resolution of calorimeters.

Iron, copper, tungsten, lead and uranium are typically used as absorbers, depending on the desired radiation or nuclear interaction length. Practical considerations such as the cost and the mechanical properties of the material also influence this decision.

radiation emitted at a characteristic angle $\cos\theta = 1/\beta n$.

3.1.4 Liquid argon calorimetry

A calorimeter that determines energy by detecting ion pairs produced by ionizing particles, such as the Hadronic Endcap, needs to have an active material that collects a reasonable fraction of the deposited charge to enhance the signal to noise ratio [29]. This means that the material must be dense, be an electrical insulator, and have a relatively high electron mobility. In the Hadronic Endcap calorimeter, liquid argon was chosen as the most suitable material.

Liquid argon (LAr) is widely used in calorimetry because of its relatively high electron mobility (5 mm/μs at 1kV/mm), and since it is a noble gas, it does not capture free electrons (no loss of signal). The 23.6 eV ionization potential of LAr allows the production of a large number of electron-ion pairs. Also, liquid argon is much easier to obtain and to purify than other noble gases, such as liquid krypton or xenon, and is thus much cheaper. Finally, LAr is radiation hard, which is important since the level of radiation in the endcap calorimeters will vary between $10^3 - 10^4$ gray (Gy) per year near the beam pipe [10] [6].

In LAr ionization calorimetry, electric fields are applied across LAr gaps, and the currents induced by the motion of ionization electrons are detected (see Figure 3.2). The electrons are produced by the passage of charged particles through the argon creating electron-ion pairs. The total current collected is then proportional to the energy deposited in the argon by a particle passing through the gap. The energy deposited in the absorber is not measured directly, but knowing the sampling fraction, this lost energy can be calibrated out on average. It is therefore possible to reconstruct the total energy lost by a particle in the calorimeter.

Because of the differences in the processes involved in electromagnetic and hadronic showers, the calorimeter's response between electromagnetic and hadronic particle of same initial energy may be different. The ratio of the electromagnetic to hadronic response is called e/h. Its value is determined by several factors: the Z of the absorber

[6] This is the γ dose for a normal high luminosity year. About 10^{14} 1 MeV neutrons also will go through this region of the calorimeter. Note that 1 Gy = 100 rad = 1 joule/kg = 6.26×10^{12} MeV/kg deposited energy [21].

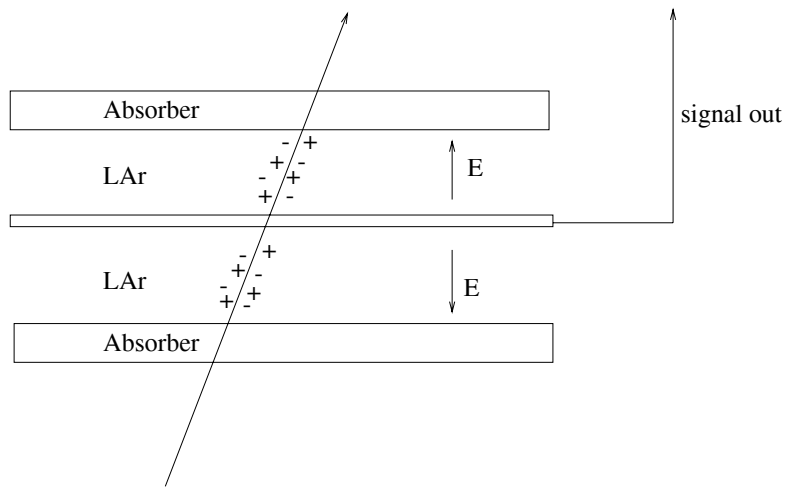

Figure 3.2: Schematic drawing of a liquid argon (LAr) ionization chamber. Shown is a single particle traversing the LAr gap, producing free charges (electrons). The drifting electrons then induce a signal on the central readout plane.

material, the thickness of the passive and active layers, the signal integration time of the detector, and the properties of the readout material. It has been shown that e/h values are larger than 1.0 for any calorimeter using liquid argon readout [26]. This difference arises mainly from the energy loss occurring in nuclear reactions, such as the energy spent in breaking up nuclei (binding energy) and the energy transferred to neutrons, which are abundantly produced in these reactions. Also, several reactions caused by hadronic showers generate "invisible energy", which cannot be detected. In fact, most of the ν's and μ's produced in the cascade generally escape the detector without interacting with the material.

Strategies have been devised to enhance the signal from neutrons such that the e/h ratio of calorimeters is or is approximately 1. Such detectors are described as compensating, and are well described in [26]. However, the Hadronic Endcap Calorimeter is non-compensating.

3.1.5 Resolution

The response of the calorimeter to an incident particle of a given energy follows approximately a normal distribution if the shower is fully contained. The performance

of the calorimeter can be assessed by its energy resolution σ/E, where σ is the width of the response distribution at which the energy E of a particle can be measured.

The resolution of the calorimeter can be parameterized as a function of energy as

$$\frac{\sigma}{E} = \frac{A}{\sqrt{E_0}} \oplus B \oplus \frac{C}{E}, \tag{3.8}$$

where E is the measured energy, E_0 is the initial particle energy, and $\oplus$ means addition in quadrature. The three distinct terms in the parameterization are referred to as the sampling, constant and electronic noise terms, respectively. The sampling term is primarily determined by the sampling quality (fraction and frequency) of the calorimeter and, in the case of hadronic calorimeters, by non-compensation. The constant term depends mainly on mechanical imperfections, incomplete shower containment and also non-compensation. Finally, C reflects the electronic noise impact on the resolution.

With higher energy, the resolution improves and becomes more sensitive to the constant term, while the effect of the electronic noise on the width of the response is energy independent. Since the electronic noise is energy independent, the contribution of C on the resolution is greater at lower energies.

3.2 Design

The two Hadronic Endcap Calorimeters are located in the forward region behind the electromagnetic accordion calorimeters (EMEC) and are sharing two 43 m^3 liquid argon cryostats with the EMEC and FCAL (see Figure 2.3). The hadronic endcaps cover the pseudorapidity region $1.5 < |\eta| < 3.2$, and have a total thickness of 10 interaction lengths (λ_I), which allow nearly full longitudinal containment of hadronic showers (see Section 3.1.2).

3.2.1 Copper plate absorbers

Each endcap consists of two independent wheels of outer radius 2.03 meters; each of these wheels is segmented radially in 32 pie-shaped modules as shown in Figure 3.3.

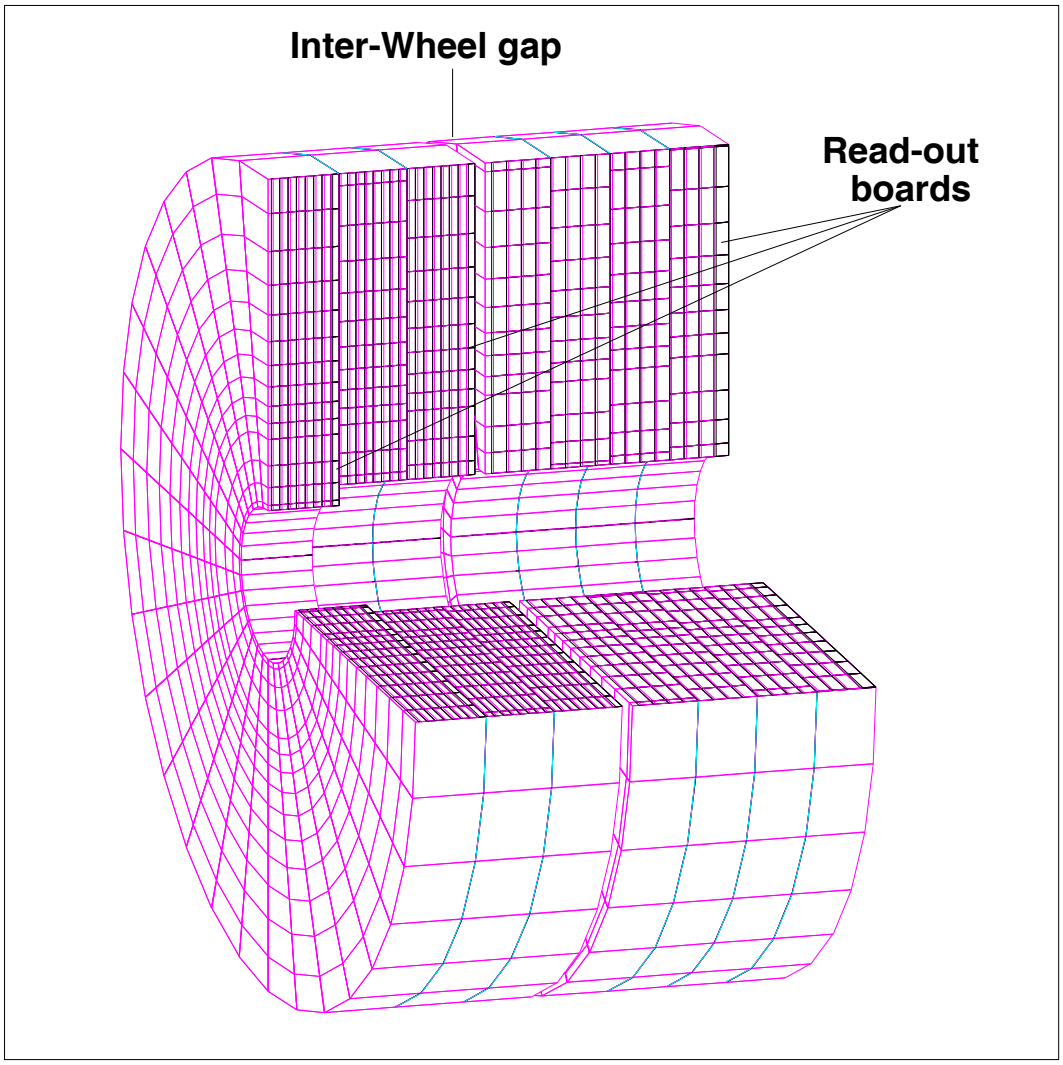

Figure 3.3: Three dimensional view of the ATLAS Hadronic Endcap calorimeter. The outer radius is 2.03 meters. Each wheel (front and rear) has 2 readout segments. The front wheel has 25 mm thick Cu plates absorbers and 24×8.5 mm gaps of argon (active material) for a total weight of 67 tons. The rear wheel has 50 mm thick Cu plates and 16×8.5 mm gaps of argon, weighing a total of 90 tons.

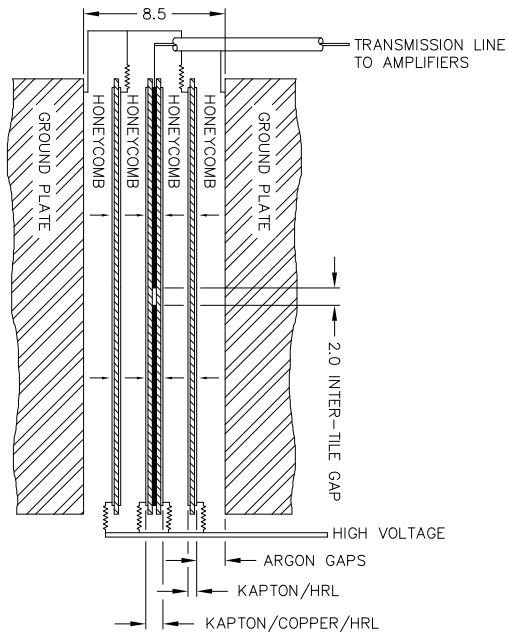

Figure 3.4: Structure of the liquid argon gaps. The PAD boards are made up of layers of kapton (insulator), copper (readout electrode) and high resistive carbon loaded kapton (HRL). The total width of the gap is 8.5 mm.

Each wheel (front and rear) has 2 readout segments. The front wheels (the wheels closer to the interaction points) have 25 mm thick copper plates as absorbers, and 24×8.5 mm gaps of liquid argon as active material. The absorbers for the rear wheels are 50 mm thick copper plates. The rear wheels contain 16×8.5 mm gaps of argon.

3.2.2 The liquid argon gaps

Within the 8.5 mm gaps between consecutive copper plates, three parallel boards separated by 1.8 mm honeycomb layers effectively split the gap into 4 drift spaces as shown in Figure 3.4. The central board, or PAD board, is composed of the readout electrode separated by kapton from two high voltage electrodes. The transverse readout segmentation is thus defined by the PAD board readout electrode structure. Each readout electrode is segmented longitudinally into 2 ϕ regions. It is also transversally divided into 13 η regions for modules of the front wheels, and in 12 η

regions for modules in the rear wheels. The segmentation of the readout electrode for a module is clearly displayed in Figure 4.1.

The remaining two boards are composed of a high-voltage and a ground electrode separated by kapton and they are known as an electrostatic transformer (EST) structure. By making the argon gap behave as a double 4 mm gap, the EST structure offers two advantages. First, it reduces by half the high voltage needed to achieve the electric field required (1kV/mm, see Section 3.1.4). Secondly, the drift distance electrons have to travel is reduced as well, staying clear of ion build-up problems.

3.2.3 Performance goals

The Hadronic Endcap calorimeter has been designed primarily to perform jet reconstruction and E_T^{miss} measurements. In fact, jet identification and measurement, as well as the reconstruction of jet-jet mass and E_T^{miss}, will play a crucial role in searches for heavy Higgs boson and supersymmetric (SUSY) particles. The performance of the HEC calorimeter is required to provide an energy resolution for jets of [30]

$$\frac{50\%}{\sqrt{E_0(\mathrm{GeV})}} \oplus 3\% \leq \frac{\sigma}{E}(\mathrm{jets}) \leq \frac{100\%}{\sqrt{E_0(\mathrm{GeV})}} \oplus 10\%. \tag{3.9}$$

where E_0 is the initial energy of the jets and E is the reconstructed energy in the calorimeter.

Chapter 4

Beam Tests

During the summer of 1999, 6 complete modules (3 front and 3 rear wheel modules), or 3/32 of the Hadronic Endcap Calorimeter, were assembled and set in a beam test cryostat. This was the first time that production modules (modules which will be used in the construction of ATLAS) were tested and the first time that the ATLAS calibration procedure and cabling system were used. In April and August of 1998, the first Hadronic Endcap modules built to the final ATLAS design specifications were tested. But with only four ϕ segments, lateral leakage of hadronic showers occurred [31]. Negligible lateral leakage was expected in 1999 for beams centered on the calorimeter.

Beam tests are essential to control the quality of the production and in evaluating the performance of the calorimeter. In this work, the energy scans performed with electron and pion beams at several impact positions are studied to assess the energy response and resolution of the calorimeter. These results are compared with the values obtained by Monte Carlo simulations. Vertical and horizontal electron beam scans are also used to determine the spatial uniformity of the calorimeter response.

In this chapter, the procedures followed during beam tests and production of Monte Carlo simulations are discussed. In Section 4.2, the beam test setup is presented. Signal reconstruction is discussed in Section 4.3. Sections 4.4 and 4.5 cover the effects of electronic noise, and the generation of Monte Carlo simulations.

4.1 Setup

The beam tests were conducted on the H6 beam line of the SPS at CERN. The modules of the Hadronic Endcap were installed in a cryostat which was later filled with liquid argon maintained at (90.0 ± 0.1) K. Several subdetectors, such as trigger counters and multi-wire proportional chambers, were installed in the beam-line to track particles. This section describes the beam test setup: the layout of the modules, the trigger system, the processes followed for readout and calibration, and finally, the various particle beams used.

4.1.1 Modules layout

During the 1999 beam tests, the calorimeter was segmented in 4 readout depths: two in the front wheel (z=1 and z=2) and two in the rear wheel (z=3 and z=4). The first readout segment (z=1) consists of 8 LAr gaps, each separated by 2.5 cm of copper. The second segment (z=2) consists of 16 LAr gaps also separated by 2.5 cm of copper. Both of the last two readout segments (z=3 and z=4) consist of 8 LAr gaps separated by 5 cm of copper. A readout cell is defined as a pointing tower spanning a longitudinal readout segment. Figure 4.1 shows the layout of the readout cells for the first depth. The cryostat window, the region where the beam could be set to enter the calorimeter, is also indicated. The beam was set to enter the calorimeter at different locations, or impact points. In this work, 5 impact points were studied and correspond to beams centered on readout cells 61, 57, 37, 33, and 29. These impacts are referred to as impact B, C, F, G and H, respectively.

The Hadronic Endcap calorimeter is designed to provide a semi-pointing geometry in pseudorapidity. However, because of space constraints within the cryostat, the modules could not be positioned in the proper pointing orientation. Instead, the beam entered parallel to the symmetry axis which resulted in showers depositing energy in a larger number of cells than they would in ATLAS (see Figure 4.2). As a consequence, the reconstruction of the energy required larger clusters (groups of cells), which means that the electronic noise contribution to the energy resolution

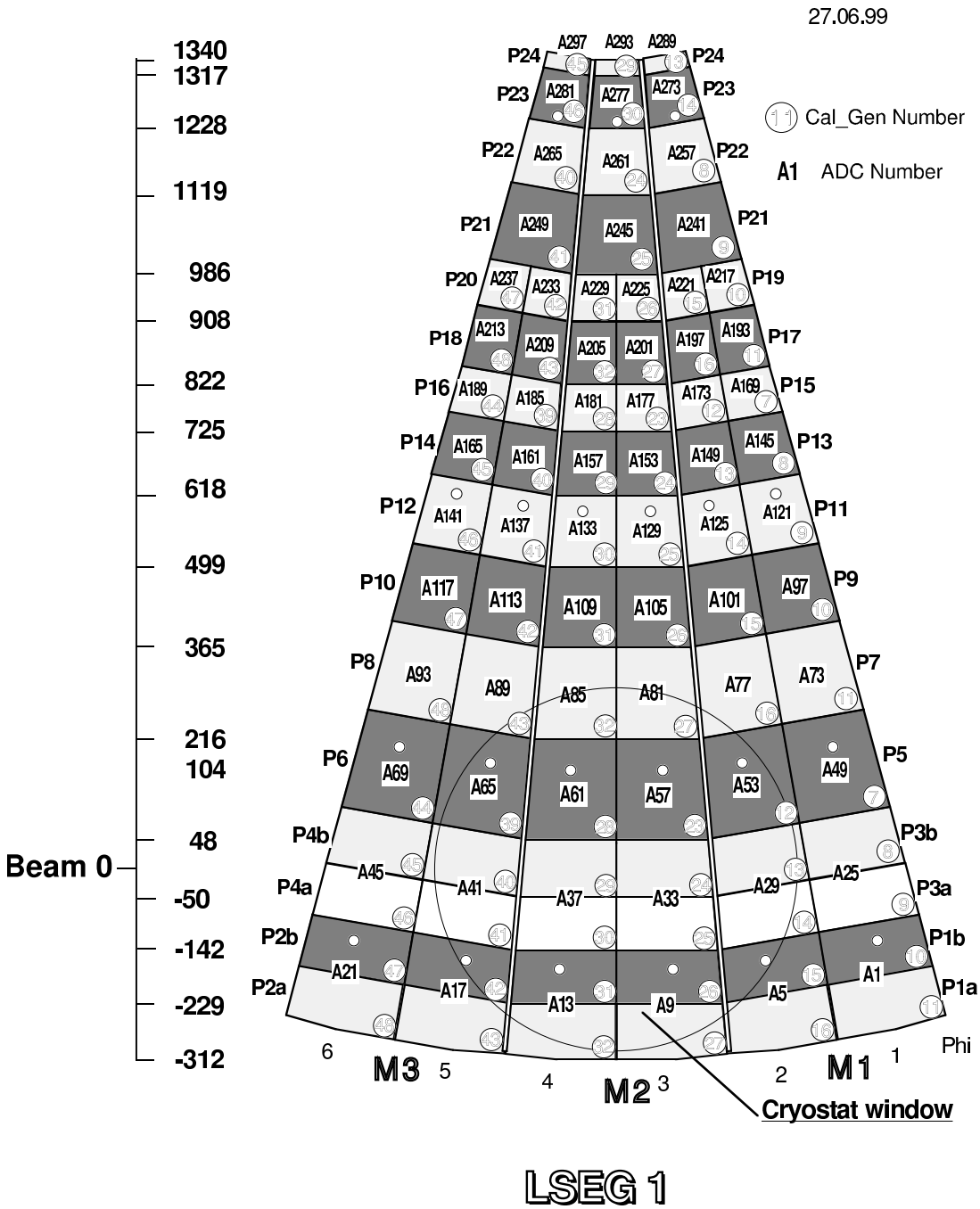

Figure 4.1: The geometric layout of the readout cells for the first depth (z=1). The beam enters in a direction perpendicular to the surface shown, in a region behind the cryostat window. The numbers appearing in the squares and preceded by an "A" are identifying the channels used for the readout cells; the circled numbers are identifying the channels from the calibration generator. The layout of the readout cells for the remaining 3 depths is presented in Appendix B. The impact points used in the analysis correspond to beams centered on readout cells 61, 57, 37, 33, 29 and are referred as impact points B, C, F, G and H, respectively. Scale in mm.

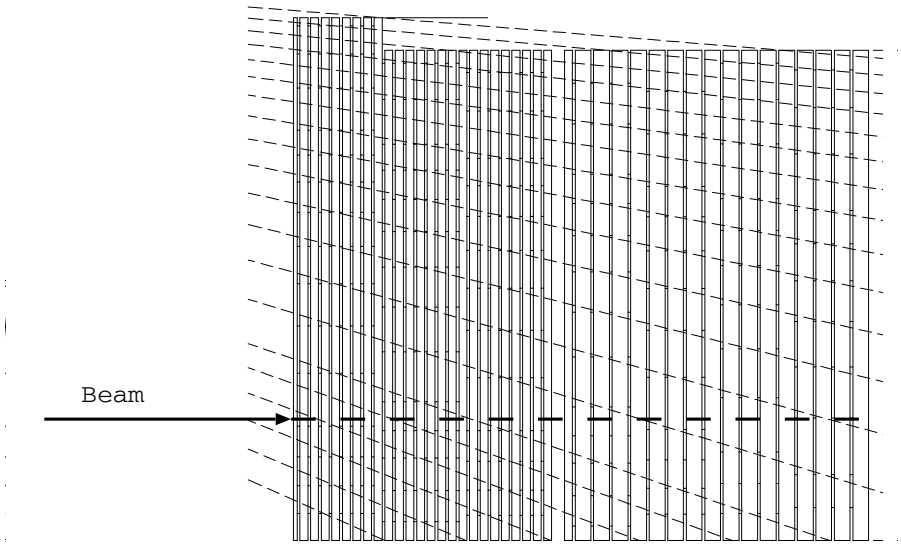

Figure 4.2: Comparison between the orientation of the beam and the semi-pointing geometry of the Hadronic Endcap calorimeter. The dashed lines represent possible trajectories of a particle traveling in a straight line from the ATLAS vertex (constant pseudorapidity). The readout cells are positioned accordingly to these pseudorapidity lines in a stepped fashion, creating a semi-pointing geometry. The thick line represents the incident particles during the 1999 beam tests.

is increased compared to what it would be for ATLAS.

4.1.2 Trigger system

In order to eliminate undesirable events, such as those caused by particles coming from the beam halo (periphery of the beam), several detectors were added in front and behind the cryostat. Figure 4.3 shows a schematic view of the setup giving the location of the different triggering detectors. B1, F1 and F2 are scintillating detectors, located upstream from the cryostat. F1 and F2 are oriented perpendicularly to one another, and effectively define the transverse size of the beam (a square of about 2.5 cm $\times$ 2.5 cm). Both are mounted on a motorized table (y-table) which can be displaced in the vertical direction. VM and *hole* are both scintillating counters used to eliminate or "veto" particles from the beam "halo", that is, particles coming from the periphery of the beam creating a signal in the VM and hole counters.

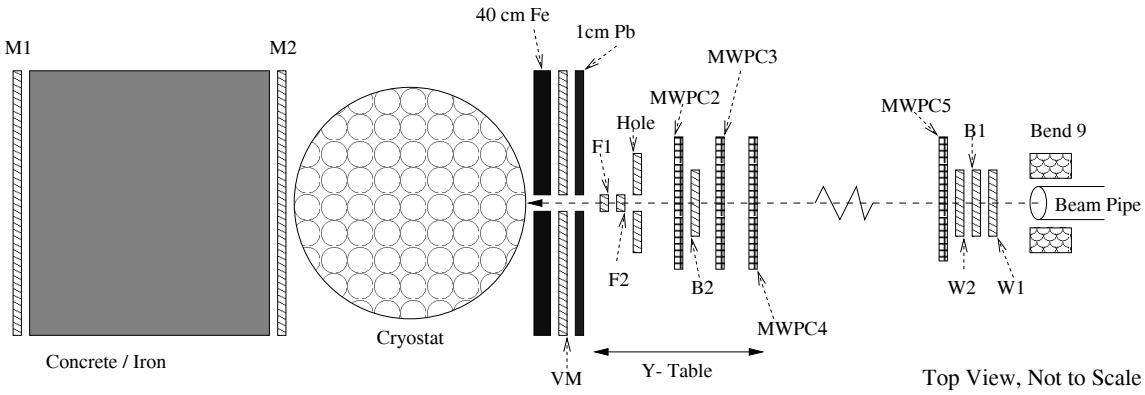

Figure 4.3: Setup of the HEC beam tests. The detectors shown in the diagram are: bend 9: final bending magnet; W1,B1,B2,W2: beam counters; MWPC : multi-wire proportional counters (beam chambers); F1,F2: finger counters which define transverse size of the beam; VM: muon veto; M1,M2: muon counters.

The pre-trigger, or the presence of a signal in the B1, F1 and F2 detectors upstream from the cryostat, was the first condition to keep any event for this analysis. Also, events were not recorded whenever two events occurred too closely in time, creating an overlap of signal in the detector (pile-up). Finally, events arising from random triggers were discarded. Events passing all of the above cuts are called physics events.

Since the Cherenkov detector (CEDAR) efficiency is limited to low energy particles, it was impossible to distinguish electrons from pions via the trigger system for most of the runs. The CEDAR separates particles according to the Cherenkov opening angle (see Section 3.1.3), and the difference between electron and pion angles gets smaller at higher energies. In practice the separation limit is around 80 GeV [32]. But, as it will be shown later, software selection criteria were sufficient.

M1 and *M2* are also scintillating detectors located behind the cryostat. They are used, together with the VM, to identify muons.

When studying the uniformity of the calorimeter (Section 5.6), the multi-wire proportional counters (beam chambers) were also used to determine the exact location of the beam particle impact on the calorimeter. The position was calculated via the beam chamber reconstruction package included in the HEC beam test software

package [35].

4.1.3 Readout and calibration

Figure 4.4 shows the various electronic components for the calibration and readout of the HEC during the 1999 beam test. The signal produced in each of the calorimeter readout cells is sent via what are known as return cables and the shapers of the Front End Boards (FEBs) before being read out by fast analog digital converters (flash ADCs). For the beam tests, the same cabling system as the one to be used in ATLAS (for example the same cable length) was installed. ATLAS FEBs, which contain the pre-shapers, shapers and line drivers, were used for the first time (see Figure 4.4). FEBs were installed for the beam tests shortly after they were produced, and hence were not fully studied until after the beam test period was over. Several problems were then noted: the gain and integration time of the pre-shapers were outside the design values, some of the shapers were not working properly, and finally, the drivers were observed to have a different transfer function than expected. These problems caused the readout of the channels close to the edge on the FEB connectors to have an increased level of noise. The signal reconstruction is discussed in detail in Section 4.2.

In order to obtain a relationship between the current measured on the readout boards and the electronic signal, each of the readout cells was calibrated individually. To do so, external calibration generators injected known current pulses to all of the readout electrode by a network of coaxial cables and strip lines. The relationship between the injected current and the resulting ADCs signal produced (after pedestal subraction and digital filtering, see Section 4.2) was then parameterized in terms of a 3rd order polynomial with different parameters for each readout cell. As a result, the cell-to-cell differences in the electronics gain were corrected. This calibration allows the energy in ADC counts to be converted to energy in units of current (nA) produced in the gaps by ionization [1].

[1] Typically, 1 ADC count$\approx$50 nA and 1 nA$\approx$0.0038 GeV.

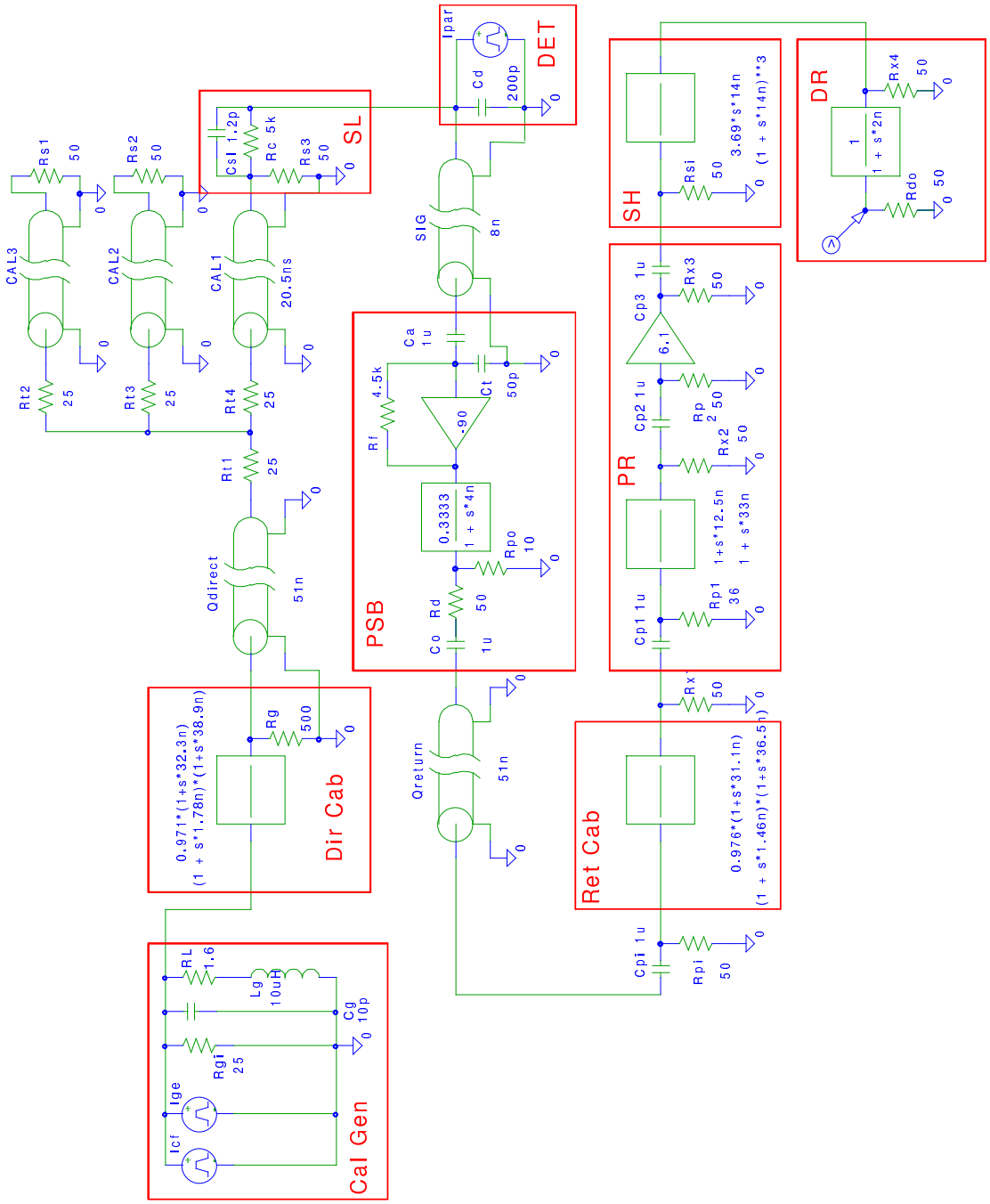

Figure 4.4: The various components of the HEC electronic chain as modeled for analytic calculation of its performance. The calibration generators (Cal Gen) current is transmitted to the detector (DET) by the calibration cables (Dir Cab) and striplines (SL). The signals produced at the PAD boards (PSB) exit the cryostat via the return cables (Ret Cab) and are shaped by the FEB boards (preshaper (PR), shaper (SH), and driver (DR)). Finally, the signal is digitized by fast analog digital converter (flash ADC's) every 25 ns, and readout by the data acquisition system.

In 1999, the ATLAS calibration procedure was followed for the first time [34]. The production of calibration parameters for the HEC was the responsability of the Institute of Experimental Physics of the Slovak Academy of Sciences, Kosice. Also, the length of the calibration cables were set to match exactly the length they will be in ATLAS. To describe the calibration response of this new, more complicated chain, the old electronics model had to be improved substantially. Unfortunately, no modifications were made by the Kosice group for the 1999 beam tests, which influenced the quality of the calibration. Recalibrating the HEC electronics is outside the scope of this thesis.

4.1.4 Beam production

450 GeV proton beams are first produced in the SPS, the Super-Proton-Synchrotron. The H6 and H8 beam lines in the EHN1 experimental area (North Area) provide both secondary and tertiary electron, pion and muon beams by using a common target, and an array of magnets and collimators. The primary target is used to produce electrons and pions (see Sections 3.1.1 and 3.1.2) of a wide range of energies, the upper limits being 300 GeV for H8 and 200 GeV for H6 for standard running conditions.

Low momentum particle beams ($10 < p < 100$ GeV [2]) are produced when the H6 beam-line is used in tertiary mode, that is, when a second target is introduced into the beam-line. This second target is either a block of 9 mm thick lead (for pion selection), or a piece of polyethylene (for electron selection). In this mode, the first part of the beam (between the two targets) is tuned for the highest possible momentum (200 GeV), while the second part is tuned for the requested low momentum. Momenta from 10 to 80 GeV can be selected by the user simply by loading the corresponding beam files, which set the magnets and collimators properly. The drawback in using tertiary beams is a loss in intensity. Typical beam intensities range from a few 10^2 p.p.s (particle per second) for 10 GeV (tertiary) beams to a

[2] The momentum throughout this work is always expressed in natural units: $\hbar = c = 1$.

few 10^4 p.p.s for 200 GeV (secondary) beams [32].

The separation of electrons from hadrons ($\pi^{\pm}$) is achieved by synchrotron radiation energy loss in a series of magnets followed by the collimation of the hadrons. At 200 GeV, the separation is 16 mm at a distance of $\sim$ 350 m [3]. The momentum resolution is given by a set of two collimators and is of the order of $\delta p/p = 0.3\%$ for a standard setting of the collimators. This means that the error on the beam energy is negligible compared to the calorimeter resolution, and will thus be ignored in the analysis.

4.2 Signal reconstruction

As was mentioned in the previous section, the signal from each readout cell for each event is recorded in ADC counts every 25 ns for a total of 400 ns, or 16 time samples. In Figure 4.5, a typical signal shape from a data sample is shown. The first 5 time samples, called the pedestal region, occur before the signal rise and are used to compute the base level of the ADC for zero input, known as pedestals; the signal maximum was set to occur close to the 9th time sample.

From the readout cell signal time profile, the cell response is computed as follow:

- First, the pedestal is averaged over the entire run [4].
- The pedestal is then subtracted from the cell signal for all time samples.
- The digital filtering method (described in Section 4.2.2) is then applied to calculate the cell response.
- Finally, the response is converted from ADC to nA using the calibration coefficients.

[3] $\delta E = \frac{4\pi}{3}\frac{e^2}{R}\beta^3\gamma^4$ and $E = \gamma mc^2$ meaning that $\delta E \propto 1/m^4$. Therefore, synchrotron radiation loss is $\approx 10^{10}$ less in $\pi^{\pm}$ than in $e^{\pm}$.

[4] Data was taken and recorded in runs, that is, files were created for each beam setup (same impact point, particle type and energy) and contained typically 10,000 events.

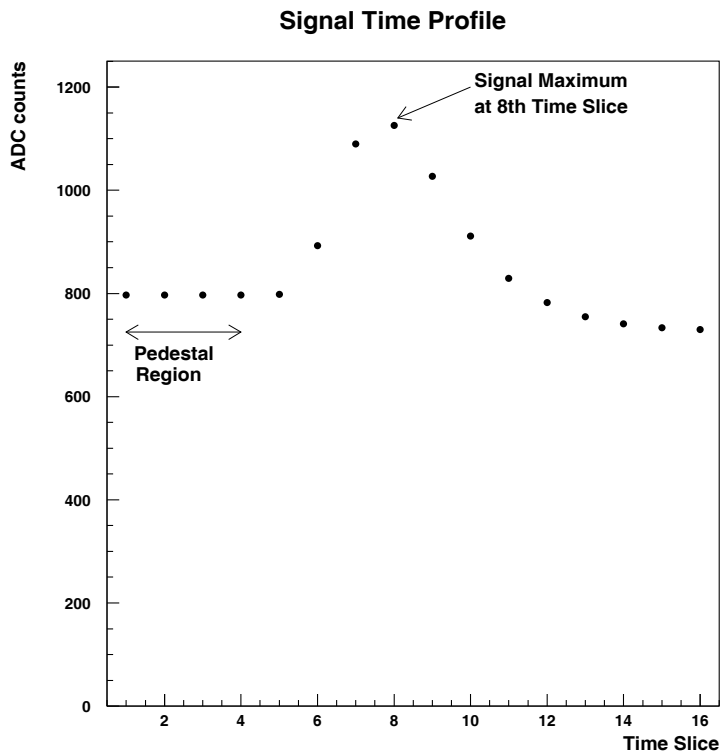

Figure 4.5: Time profile of a typical readout cell signal from a sample (or slice) of the 1998 electron runs data [36]. The pedestal region (time samples 1-5) is important in calculating the electronic noise. In 1999, the timing of the signal maximum was set to occur in the 9th time sample to ensure that no signal was present in the pedestal region, and to study the electronic noise.

Readout depth (z)	EM weights
1	1
2	1
3	2
4	2

Table 4.1: Electromagnetic (EM) depth weights applied to the readout cells for calibrated signals (nA). These weights originate from the difference in the sampling fraction between the front and rear wheels.

Additional correction factors were also applied on the response of specific cells because of differences in sampling fraction and because of a few high voltage (HV) problems. The sampling fraction in the front wheel is twice that of the rear wheel so that, for showers, a factor of two must be applied to the energy measured in the third and fourth depths (z=3 and z=4). These depth weights are presented in Table 4.1.

Some HV problems were experienced during the 1999 beam test and required disconnecting five of the EST boards. The faulty EST boards were disconnected by turning off the corresponding HV channels from the HV generators. As it was shown in previous years, correction factors completely restore the response and resolution. The only noticeable consequence of the HV problems is a corresponding rise of electronic noise [31] [33]. In order to compute the correction factors, the number of HV channels turned off in each readout depth was taken into account. There are four HV sources per depth. Hence, if one (two) of the HV channels is turned off in a readout depth, 1/4 (1/2) of the signal is lost. The necessary correction factor is therefore 4/3 (4/2). HV correction factors are summarized in Table 4.2. The readout cell 61, located in the first depth of module 2, needed an additional correction factor of 2.00. This additional factor was necessary to correct for a damaged output connector [34].

A software package [35] was written by the University of Victoria ATLAS group to compute the response of the readout cells. In the following sections, the procedure used by this software package to calculate the pedestals and the energy deposited

Module	Segment (z)	Correction factor
1	2	1.33
2	4	1.33
3	2	2.00
3	4	1.33

Table 4.2: Location of the disconnected EST boards, and corresponding correction factors. Note that in the second depth (z=2) of module 3, two EST boards were disconnected. Because of amplification problems, readout cell 61 needed an additional correction factor of 2.00.

are discussed.

4.2.1 Pedestal computation

Different ways of evaluating the pedestals have been tested. In this work, the pedestals for each cell were determined from the average of the signal in the first time sample (in ADC) over all physics events (events that passed the triggers) within a run.

In previous analyses, the pedestals were calculated from random events (within particle runs) or from dedicated noise runs with no particle beam (see Section 4.3). In both cases, the events were produced by software triggers when no beam was entering the calorimeter. The two methods led to different results, by an average of (0.3 $\pm$0.1) ADC. Eventually, these two methods were discarded when it appeared that they were overestimating the pedestals, causing a large offset in the response. The pedestals used in this analysis (using the physics events) are compared with the pedestals obtained from random events in Figure 4.6. The pedestals from random events are shown to be overestimated on average by (2.5 $\pm$0.1) ADC. This difference has not been understood.

4.2.2 Digital filtering

The digital filtering method applies weights, computed using the time sample autocorrelation function, to the signal of five time samples. It gives the best possible

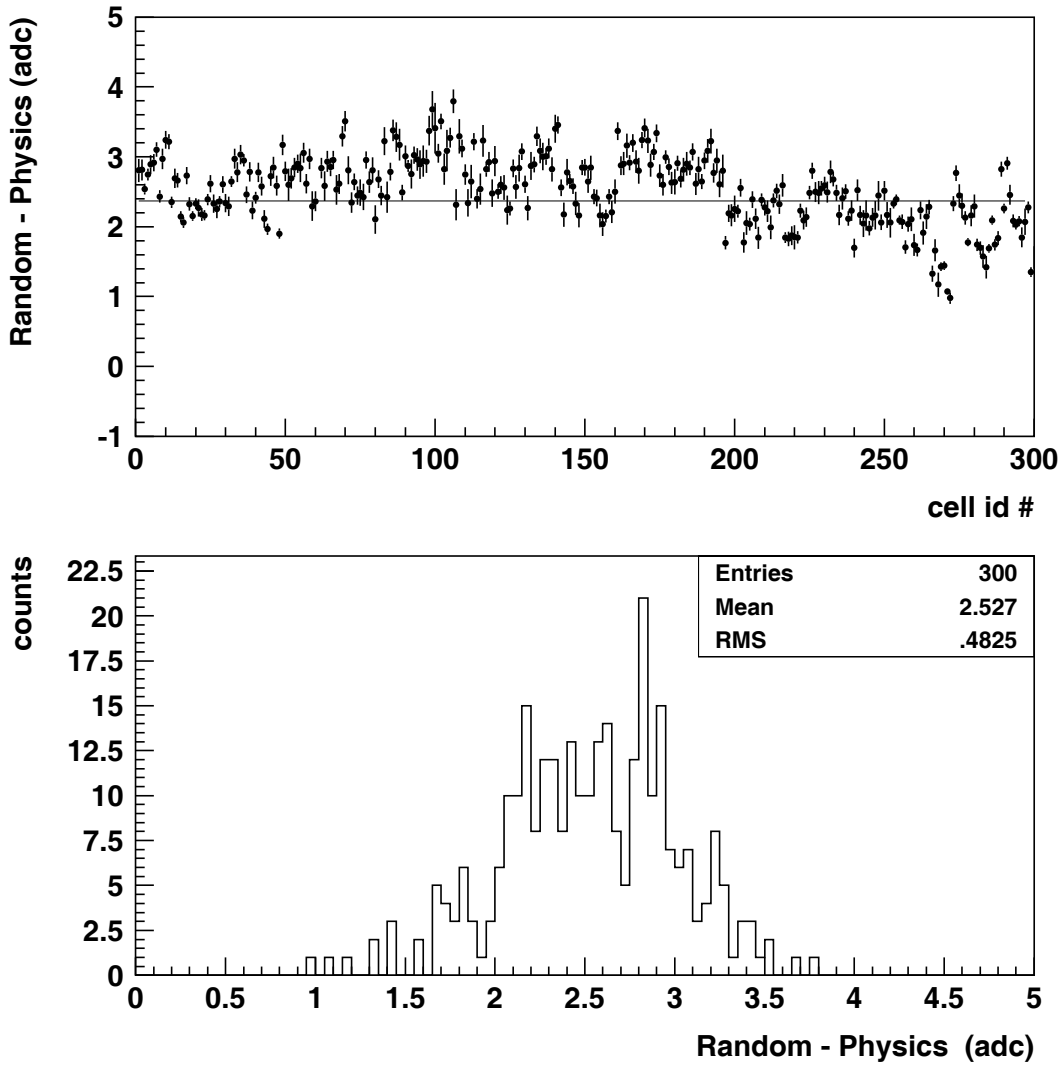

Figure 4.6: Difference in the value of the pedestals computed from random events and from physics events for run 9171 (193.1 GeV electrons at impact position C). The overall average difference is of (2.5 $\pm$0.1) ADC. The error bars shown are purely statistical.

signal to noise ratio for the determination of the signal height and time for those 5 time samples [35] [38]. To calculate the response of the readout cell for a shower event, the digital filtering method is applied over the 5 time samples centered on the signal maximum (9th time sample).

4.3 Electronic noise

In order to verify the intrinsic characteristics of the Hadronic Endcap calorimeter, the electronic noise present in the response must be measured to extract the sampling and constant term from the overall energy resolution.

In this analysis, the electronic noise of a channel is evaluated from the distribution of the signal in the pedestal region over an entire run. The signal is obtained by applying the digital filtering method to the pedestal subracted ADC signal over the first 5 time samples for physics events, events which passed the trigger cuts (see Section 4.1.2). Also, the calibration coefficients, EM weights and correction factors used in calculating the cell response to showers were applied when needed (Section 4.2). The width of the distribution obtained was defined as the electronic noise. This process was then repeated to every particle beam run analyzed.

The distribution of the signal in the pedestal region (also referred to as noise distribution) was observed to be non-Gaussian. This is shown in Figure 4.7 for several cells, where non-Gaussian positive tails can be seen. It was also noted that the most probable value (current) of the distribution was non-zero and negative for most cells: between -20 and 0 nA (within errors). The variation in the noise values shown in Figure 4.7 can be explained by the channels in the second layer having twice as many preamplifier connected together than the other channels, resulting in a noise $\sqrt{2}$ times greater.

The energy deposited by an electromagnetic or hadronic shower as it propagates through the calorimeter is distributed over several cells that form a cluster. To reconstruct the energy of an electron or pion shower, the energy of each cell in the cluster must be summed. The cluster electronic noise will then have contributions

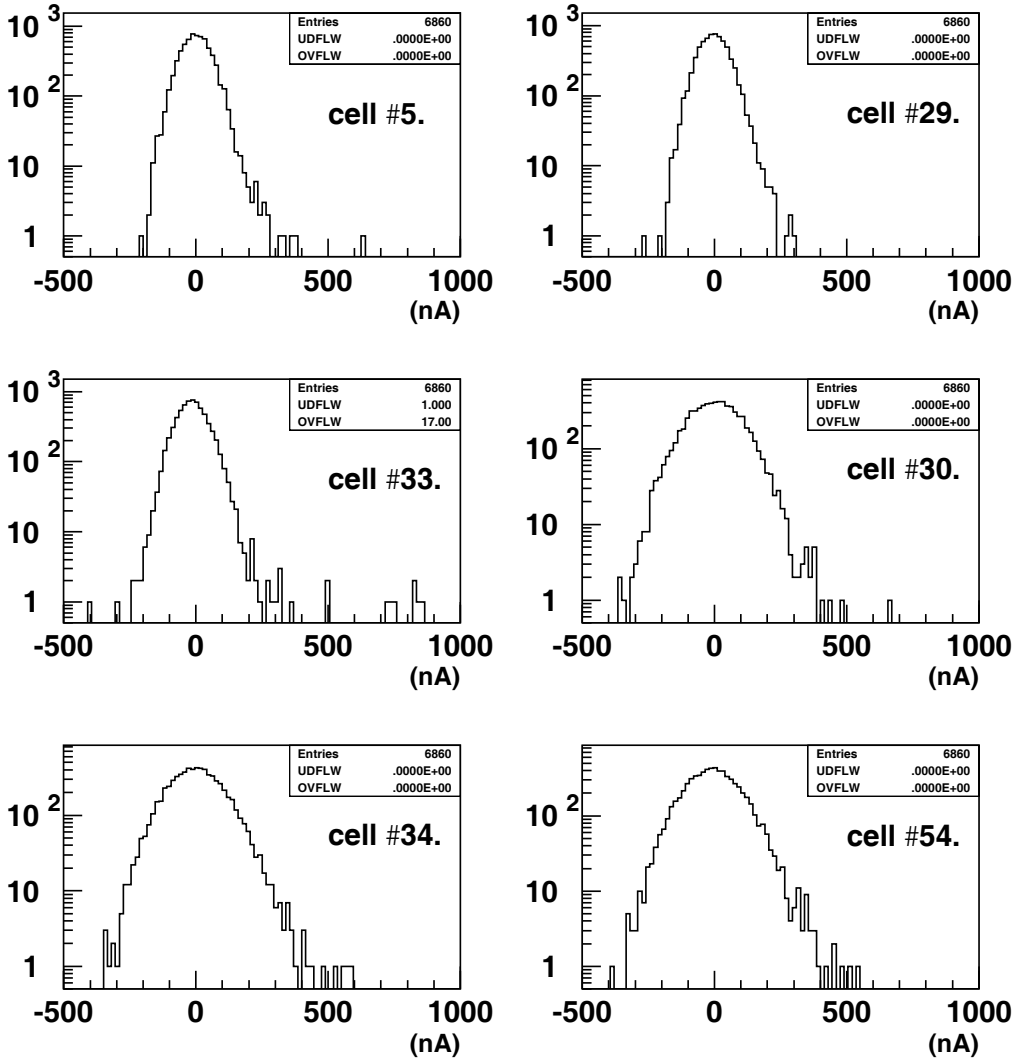

Figure 4.7: Distribution of the signal (in nA) in the pedestal region for various cells for run 9011 (10 GeV electrons). The width of these distribution is the electronic noise. For most cells, non-Gaussian positive tails are observed, and the most probable value of the distribution is negative. The cell identification number is also given. Note that cells 5, 29 and 33 are from the 1st depth; cells 30, 34 and 54 are from the 2nd depth (see Appendix B).

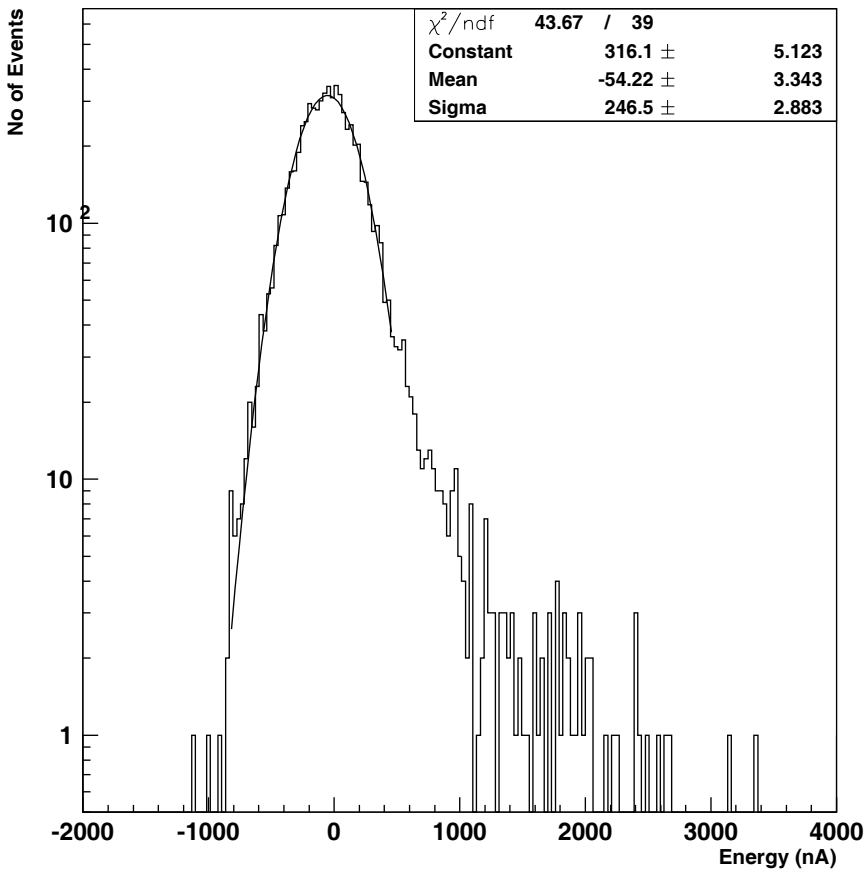

Figure 4.8: Cluster electronic noise in units of current for run 9011 (10 GeV electrons). The cluster is made of 9 readout cells. A non-Gaussian positive tail can be seen, and the most probable value of the distribution is negative. A Gaussian fit was performed on the region located between -3σ and +2σ of the most probable current, and the distribution appears to be truly Gaussian on the negative side.

from all the cluster cells. Figure 4.8 shows the cluster electronic noise for a 9 cell cluster used in the analysis of electron data. Here again, the electronic noise distribution displays a non-Gaussian positive tail and the most probable current is non-zero and negative. The cluster and cell noise distribution were found to be truly Gaussian on the negative side as shown in Figure 4.8. It was found that events with large cell noise lead to events with large cluster noise.

The cluster electronic noise in each event was then compared to the measured cluster energy as shown in Figure 4.9. An excess of events with high electronic noise can be observed on the high energy side of the cluster energy distribution. This

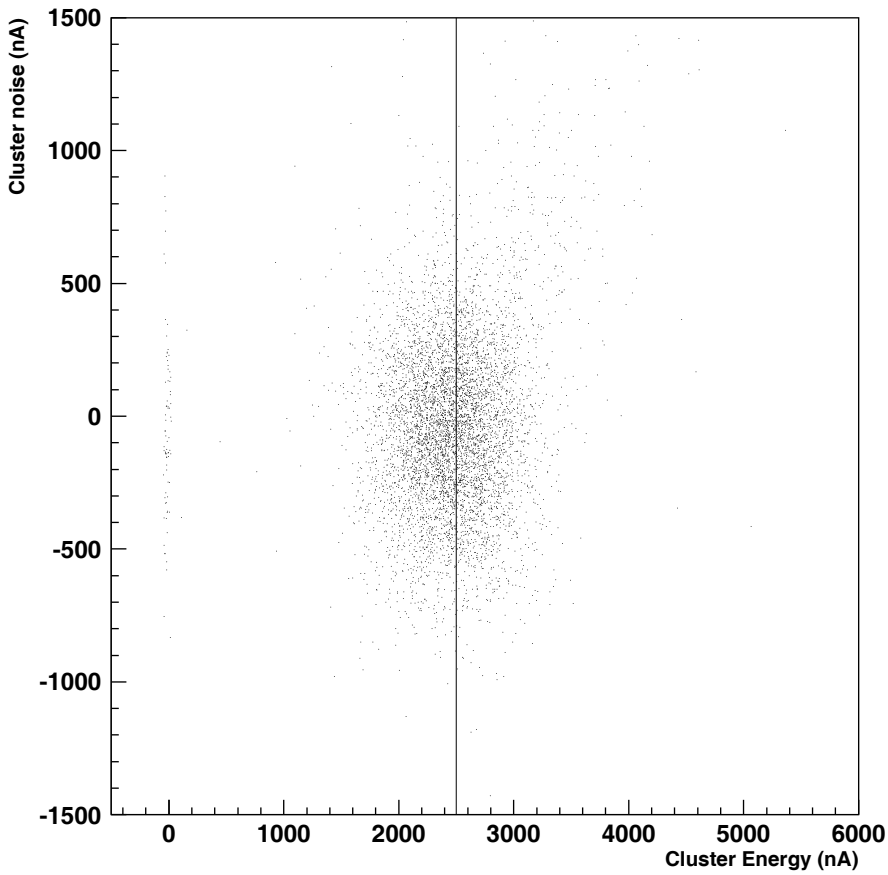

Figure 4.9: Cluster electronic noise vs. reconstructed energy in units of current for run 9011 (10 GeV electrons). The cluster is made of 9 readout cells. The vertical line shows the average energy in the cluster. A correlation between high electronic noise and high signal (energy) in the cluster can be observed.

excess shows the correlation between high electronic noise and high signal in the cluster.

The origin of the positive tails in the electronic noise distribution was investigated by asking the following questions :

- Are the tails caused by the digital filtering method ?
- Are the tails caused by the ADC to nA calibration ?
- Is there a leakage of the shower signal in the pedestal region of the signal time profile ?

Data analysis revealed that:

- The same distribution is present when the average signal over the first 5 times samples is used to calculate the noise, instead of using the digital filtering method.
- The same distribution is obtained by performing the analysis in ADC (that is without the use of calibrations), with or without applying the digital filtering method.
- The same distribution is present after removing the events for which the signal in the 5th time sample is the greatest of the 5.

Therefore, the hypotheses above failed to explain the problems observed in the electronic noise distribution. It is postulated that the positive non-Gaussian tails are caused by some positive signal [5] picked-up by all time samples for many events. This working hypothesis can explain the correlations between high electronic noise and high signal in the cluster.

To go around this problem in assessing the HEC intrinsic performance, Gaussian fits, for which the data range is not centered on the most probable value, are used to estimate the most probable current (μ) and the electronic noise (σ) of the true distribution. The asymmetric fits are first performed on a 4σ range at different locations over the distribution until a minimum χ^2 is reached. The systematic errors on μ and σ are estimated as the difference between this best asymmetric fit obtained and the values obtained from a Gaussian fit performed in the region $\pm 2\sigma$ about the most probable current. The values of μ and σ are presented in Figures 4.10 and 4.11 for all of the electron and pion runs, respectively. The clusters for electron and pion data analysis are described in Section 5.2 and 6.2.

As can be seen in Figures 4.10 and 4.11, the electronic noise was not constant during the data taking period and is therefore found to depend on the beam energy. The exact causes of these noise variations are still unknown. It was first

[5] Overlap of events (pile-up) caused by undetected particles.

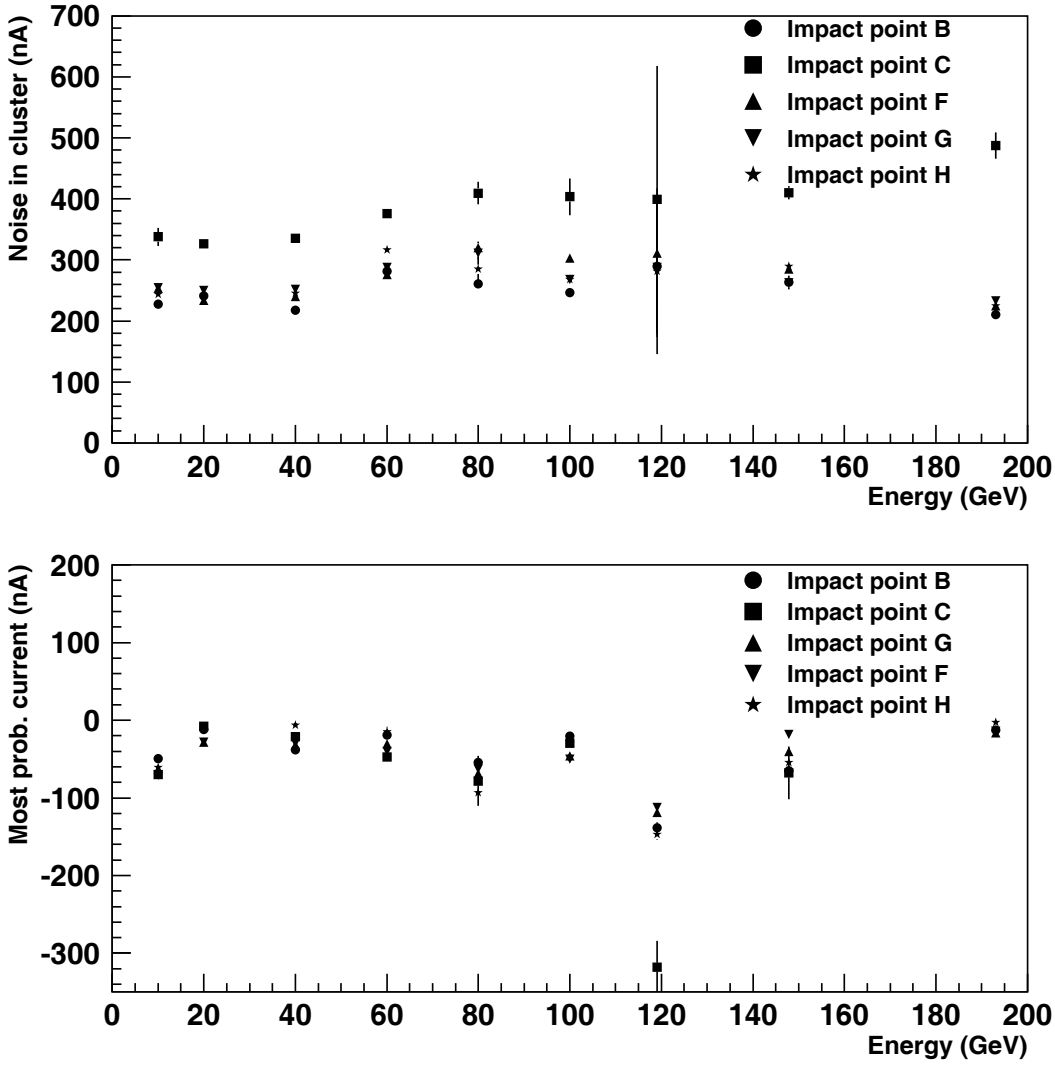

Figure 4.10: Cluster electronic noise σ and most probable current μ for all the electron runs studied. The clusters are made of 9 readout cells, except for beams at impact point C (12 readout cells). The electronic noise and most probable current are obtained from asymmetric Gaussian fits. The error bars shown include the statistical and systematic errors.

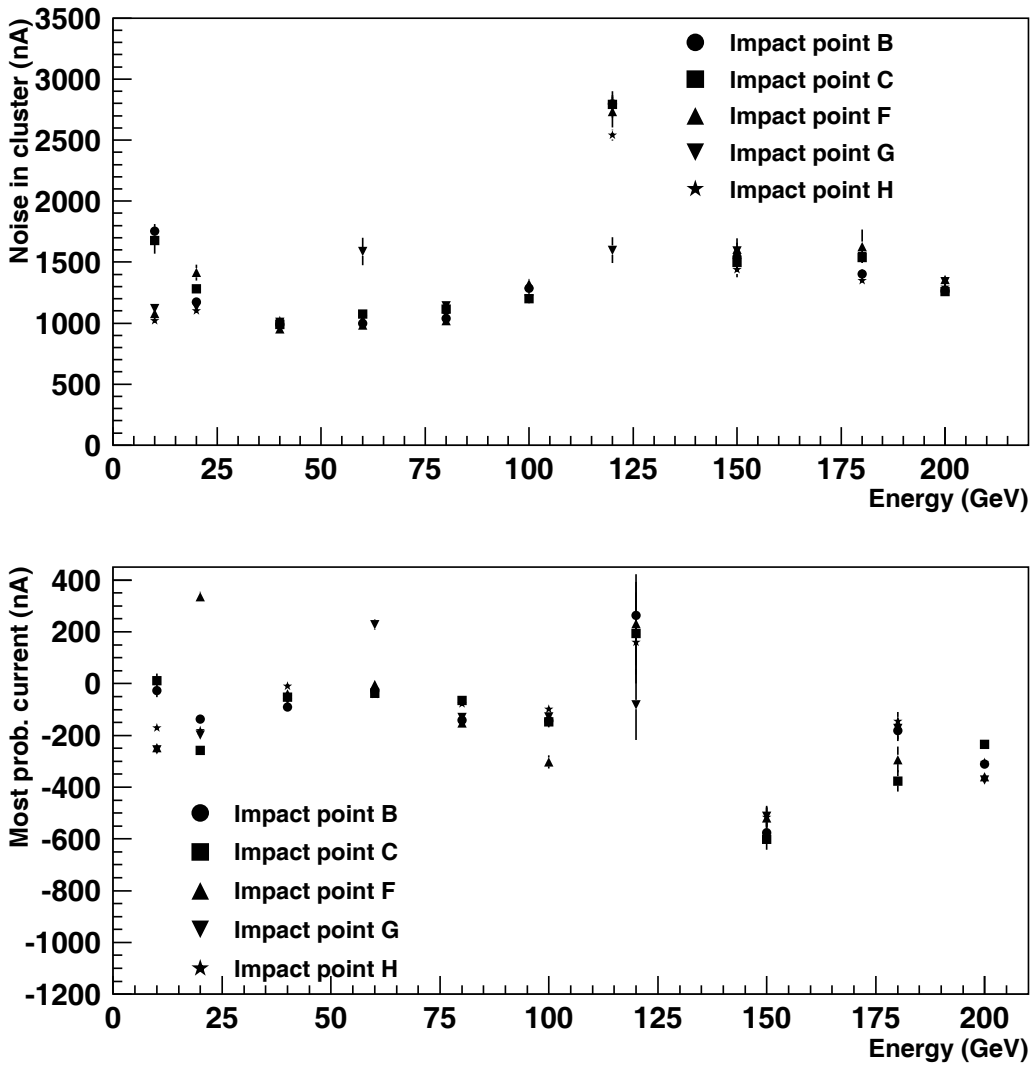

Figure 4.11: Cluster electronic noise σ and most probable current μ for all the pion runs studied. The clusters are made of 53 (B and C) or 54 (F, G and H) readout cells. The electronic noise and most probable current were obtained from asymmetric Gaussian fits. The error bars shown include the statistical and systematic errors.

thought that temperature fluctuations in the experimental hall (especially the difference between day and night) might have affected the results, but no correlations were found between the temperature of the electronics and the noise. Similarly, no major changes in the liquid argon temperature nor in the EST boards voltage were observed. Further studies were made by electronic experts, and it was noted that the noise depended mainly on a few very noisy channels [34]. In these channels, instability in the pre-shapers, shapers, or line drivers of the FEBs caused the output signal to be either delayed and/or under-amplified. This change in the output signal contributed to the variation of the noise.

4.4 Monte Carlo simulation

In order to pin-point specific problems, the evaluation of the Hadronic Endcap performance requires the comparison of experimental data with detailed simulations using the Monte Carlo method [27]. A first Monte Carlo package was released in 1996 to study the prototype modules. Since then, several changes have been implemented to the simulations. For example, Monte Carlo events now store additional quantities, such as leakage energy, which are not available in experimental data [39]. In 1999, a new version of the simulation package was released that includes all of the geometry and layout details of the August 1999 beam tests. Simulations are performed for electron and pion beams of different energies, and for different impact points on the calorimeters.

4.4.1 Electron simulation

Electron beam events are simulated for two beam locations, corresponding to impact points C and G (see Section 4.1.1). There are no geometrical differences between modules 1 and 3 in the setup of the Monte Carlo. Therefore, the results obtained from simulations at points C and G are also used to study points B and F, respectively. The energies of the electron beam are set to nine different values, between 10 to 193 GeV, corresponding to the ones used in the beam test. For each run, 2000

events are simulated. The analysis procedure consists of three main steps: event selection, energy reconstruction, and parameterization of the resolution.

In the case of simulated electron and pion runs, one and only one hit is required to occur in each plane of MWPCs to prevent an overlap of events. Other software trigger selections are applied and are described elsewhere [40]. Their effect is rather minimal, affecting less than 1% of the events in a run. On average, 85% of the events pass all the cuts. The events produced are translated to the same format as the one used for the beam test data, so that exactly the same analysis procedure can be followed. The analysis procedure is described in detail in Chapter 5, and the resolution of the calorimeter obtained from simulations is presented in Section 5.5 together with the electron beam test results.

4.4.2 Pion simulation

Pion beam events are also simulated at impact points C and G using the hadronic simulation package G-CALOR [41]. In the case of pions, each run are made up of 4000 events. The simulations are done for ten different energies, from 10 to 200 GeV, corresponding to the ones used in the beam test. The analysis procedure is the same as for electrons. First, events selection is applied, then the events are translated to a format compatible with the one used for the beam test data. Finally, the events are processed as described in Chapter 6 such that the hadronic resolution of the calorimeter can be evaluated. The pion resolution obtained from simulated events and from beam test data are presented in Section 6.4.

Chapter 5

Analysis of Electron Beam Test Data

In order to study the electromagnetic performance of the Hadronic Endcap Calorimeter, experimental data were taken for different electron beam energies. For each of the selected impact locations, the modules were subjected to electron beams of 10, 20, 40, 60, 80, 100, 119.1, 147.8 and 193.1 GeV. Each run is typically made up of 10,000 events, of which 65% to 92% pass the trigger cuts. The readout cell signal for each event is reconstructed using the digital filtering method (Section 4.2.2), and a cell cluster is formed, as explained in Section 5.2. The linearity of the response and hence the electromagnetic scale α_{em} (Section 5.3) are extracted from the mean signal produced for each beam energy. The constant α_{em} is the factor needed to translate the current (nA) measured in the calorimeter to the incoming particle energy (GeV). Pion contamination of the beams is observed, but its effect on the present analysis is found to be negligible (Section 5.4). To study the intrinsic characteristics of the HEC, the energy resolution is extracted after subtracting the measured electronic noise. Finally, the spatial uniformity of the response of the HEC is surveyed (Section 5.6). The results obtained are compared in each section with the ones obtained in 1998, and with the values from Monte Carlo simulations. Note that the HEC calorimeter is not optimized for the detection of electrons. Indeed, the electromagnetic showers in ATLAS will rarely penetrate through the electromagnetic endcap to reach the HEC. Nonetheless, the performance of the calorimeter to electron beams is

crucial because hadronic showers have an intrinsic electromagnetic content, mainly in the form of $\pi^0 \rightarrow \gamma\gamma$.

5.1 Trigger cuts

As explained in Section 4.1.2, the trigger system was used to select the events to be recorded, as well as to further refine the event selection offline. After applying the trigger cuts to the electron runs and keeping only the physics events, 6000 to 9200 events remained to be processed in the analysis. Pion events were still present in the electron sample, but as it will be shown in Section 5.4, software cuts were sufficient to eliminate them.

5.2 Clustering

The calorimeter modules are divided in readout cells, each calibrated independently (see Section 4.1.3). The energy deposited by an electromagnetic shower as it propagates through the calorimeter is distributed over several cells or cluster. The calorimeter energy associated to the incoming electron is the sum of all the corresponding cell energies. The cluster size and shape are chosen such that the electromagnetic shower is fully contained. Typically, clusters for the electron runs are composed of 9 cells. Figure 5.1 shows such a cluster, selected for impact point G. Insignificant amount of energy is deposited in the fourth layer, therefore no cells for this layer are in the cluster.

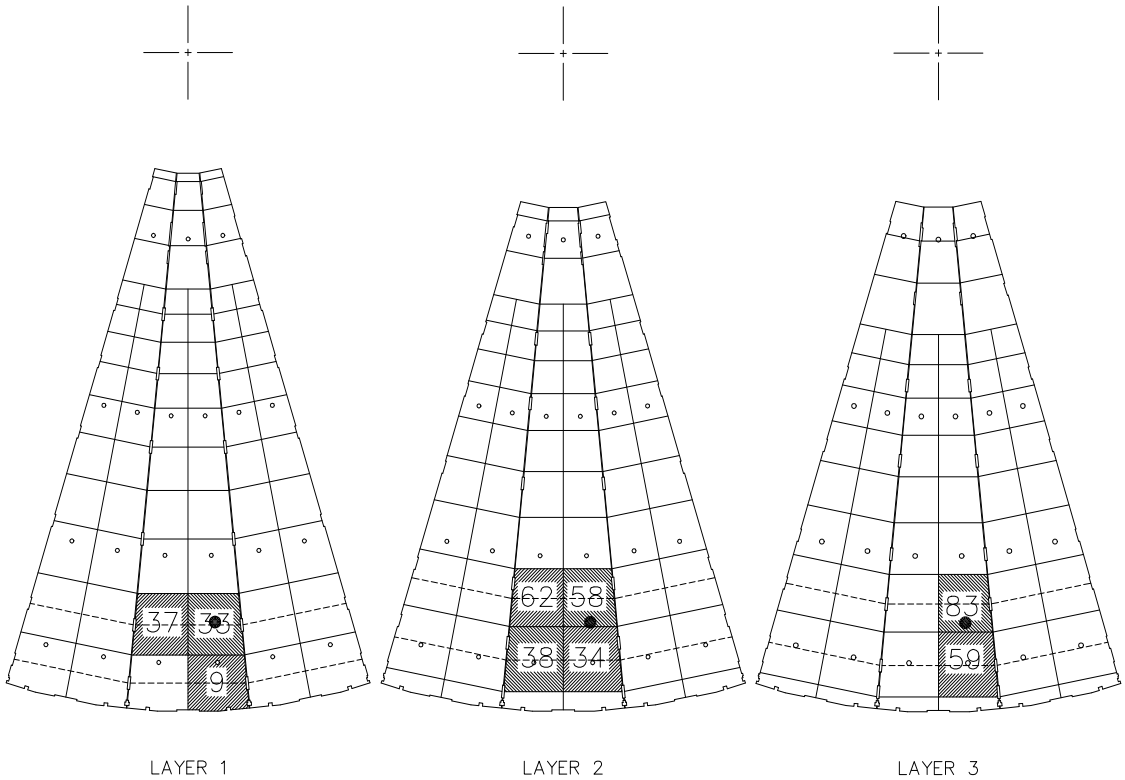

Figure 5.1: Distribution of a 9 cell cluster designed for electron runs at impact point G. The beam path through the calorimeter is denoted by a bullet. The shaded cells are used in the cluster. The number appearing at the center of each cell corresponds to the readout channel number. No cells from the fourth layer are used. The cross indicates the center of the beam pipe.

5.3 Response and α_{em} constant

The readout cell response is calculated using the method described in Section 4.2. The response of the HEC is then computed as the difference between the total energy deposited in the cluster and the cluster noise most probable current (observed in the pedestal region, see Section 4.3).

Figure 5.2 shows the energy deposited (expressed in equivalent nA) in a cluster for different beam energies. In each case, the energy follows the Gaussian distribution as expected. A fit on the region contained between $\pm 2\sigma$ from the mean is also displayed for each histogram. For the 10 and 20 GeV runs, tails are visible on the high energy side of the energy distribution and are caused by high electronic noise, as described in Section 4.3. These tails do not significantly affect the values of the mean (μ_E) and width (σ) of the responses obtained from the Gaussian fits that are used to calculate the electromagnetic constant.

The electromagnetic constant, α_{em}, allows the conversion of energies from nA to GeV for an electromagnetic shower and is expressed as

$$E = \alpha_{em} E(\text{nA}), \tag{5.1}$$

where E is the reconstructed energy in GeV, and $E(\text{nA})$ is the cluster mean response (after subtracting the cluster noise most probable current, see Appendix C). This constant is evaluated by constructing and minimizing

$$\chi^2 = \sum_i \frac{(E_i - E_{0i})^2}{\sigma_i^2}, \tag{5.2}$$

where E_{0i} are the beam energies in GeV. The value of α_{em} obtained for all impact points are shown in Table 5.1.

Figure 5.3 is a comparative plot showing the ratio between the reconstructed and beam energies. Some discrepancies are observed at energies less than 40 GeV. Nonetheless, most reconstructed energies are within one percent of the beam energies after correcting the cluster response. This correction is done by subtracting the cluster most probable current from the cluster response (see above).

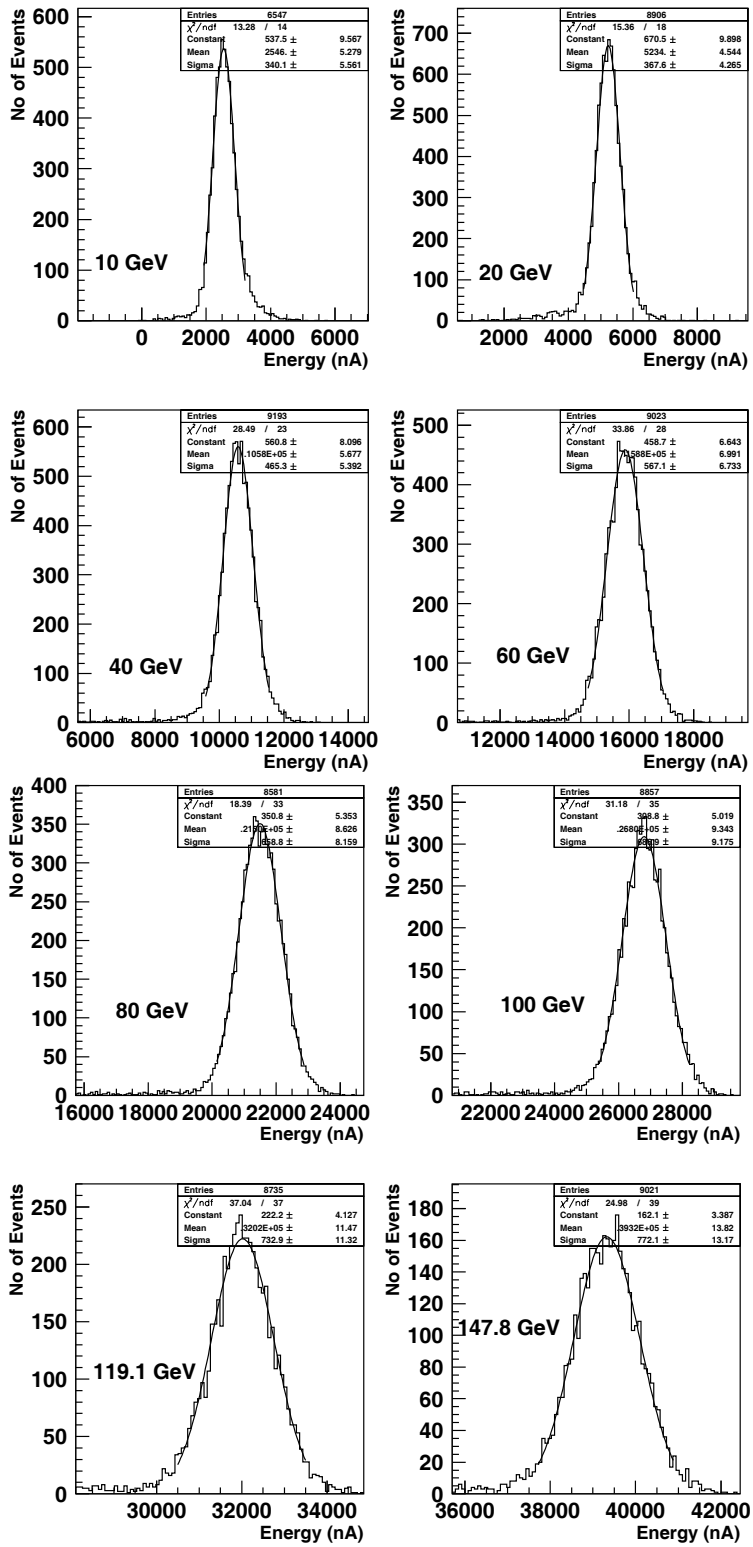

Figure 5.2: Response of the Hadronic Endcap Calorimeter in units of current measured at impact point G to 10, 20, 40, 60, 80, 100, 119.1, and 147.8 GeV electrons.

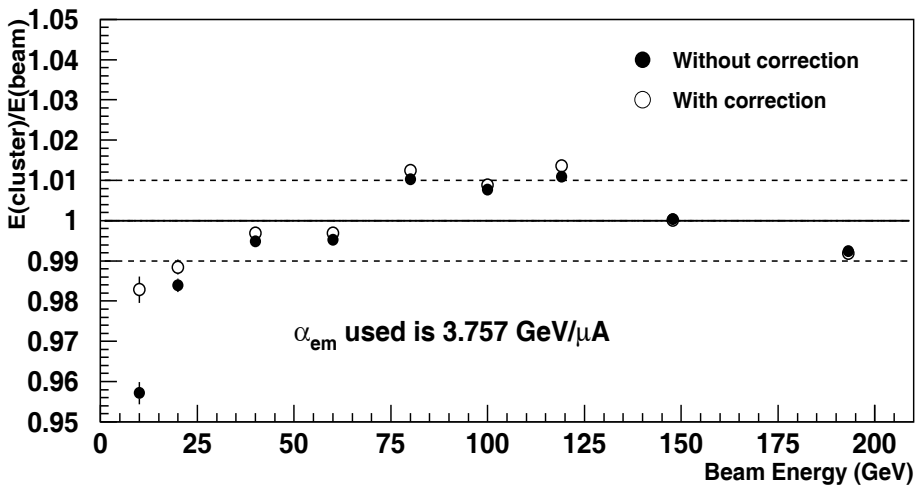

Figure 5.3: Reconstructed electron energy vs. beam energy at impact point G. The dashed lines represent a 1% variation. The correction on the response (empty circle) was done by subtracting the cluster noise most probable current observed in the pedestal region. This correction improves significantly the linearity of the response at low energy.

In an attempt to improve the linearity of the response, the HEC response to electrons was also parameterized using

$$E = \alpha_{em}\ E(\mathrm{nA}) + b, \tag{5.3}$$

where b is a constant offset. No significant changes were observed in the reconstructed energy and the offset was found to be consistent with zero. The difference in α_{em} calculated from Equations 5.1 and 5.3 was defined as a systematic error. Nonetheless, the systematic error from the observed small non-linearity dominates the final error on α_{em} and is included in the errors shown in Table 5.1. This error was calculated as the RMS deviation observed in the linearity of the response (Figure 5.3). Figure 5.3 shows how the linearity of the response improves when the cluster noise most probable curent observed in the pedestal region is subtracted from the response signal.

As can be seen in Table 5.1, the value of α_{em} is higher at impacts B and C because of the nearness of the beam with the tie-rods at those locations [1]. The

[1]The tie-rods are steel bars holding each of the calorimeter modules together. There are 7 of

Impact point	α_{em} (GeV/μA)	Cluster size (# of cells)
B	4.15 ± 0.11	9
C	3.93 ± 0.05	12
F	3.84 ± 0.05	9
G	3.76 ± 0.04	9
H	3.87 ± 0.04	9
Combined (F,G,H)	3.82 ± 0.04	

Table 5.1: The electromagnetic scale obtained for each of five beam impact positions. The averaged α_{em} comes from the weighted average for impacts F, G, and H only. The observed small non-linearity dominates the final error on α_{em}. Impact points B and C suffer from their nearness with the tie-rods and were not included in the average.

beam is not point like, but has an effective diameter of about (2.5 ± 0.01) cm (see Section 4.1.2). Hence, for some events, a sizeable fraction of the electromagnetic shower energy was deposited in the rods, and the HEC response was thus reduced. The effect of the tie-rods on the response is discussed later in Section 5.6.

The average α_{em} obtained in this analysis is (3.82 ± 0.04) GeV/uA [2], and is different from previous measurements. In fact, measurements of α_{em} in 1998 yielded an average value of 16% less [31]. The electromagnetic constant is determined by the structure of the calorimeter, the liquid argon ionization and the electric field. It should be the same for all modules at all times, independently of the electronics used. It is one of the fundamental measurements which will be of use when the ATLAS detector becomes operational in 2005. This change in the EM scale has caused some concern amongst the HEC group since its origin has not yet been fully understood [3] [33]. It is thought to be due to inadequate calibration procedures before 1999.

them per module, identified by empty circles in Figure 4.1

[2]The systematic error from the observed small non-linearity dominates the final error on α_{em}. Hence, the error on the average α_{em} is taken as the average of the errors obtained at each impact point.

[3]Andrei Minaenko calculated a value of $\alpha_{em} \approx 3.95$ GeV/μA.

5.4 Beam contamination

Excess of events in the low energy tail of the response distributions can be seen in Figure 5.2, especially in the case of the 147.8 GeV electron beam run. These low energy signals come from pion contamination in the beam. Using the same cluster as for the electrons, the study of pion beam data reveals the energy distribution due to pions in the region where the electron signal lies. Figure 5.4 shows such distribution obtained from 150 GeV pions, with a fit describing a Gaussian distribution summed with a first degree polynomial:

$$P_\pi(E) = Ae^{-\left(\frac{E-\mu}{\sqrt{2}\sigma}\right)^2} + mE + b, \tag{5.4}$$

where E is the measured energy in nA, and m and b are the slope and intercept of the polynomial. Finally, A, μ, and σ are the amplitude, mean and standard deviation of a normal distribution, respectively. This empirical function is found to fit the pion data well.

The response energy distribution, $R(E)$, observed for the 147.8 GeV electron run can now be parameterized as the sum of the energy distribution to the pions $P_\pi(E)$ and electrons $P_e(E)$:

$$R(E) = SP_\pi(E) + P_e(E) \tag{5.5}$$

where S is a scaling factor applied to the pion energy distribution, and $P_e(E)$ is simply a Gaussian distribution of mean μ and width σ. Figure 5.5 shows the result obtained after applying this parameterization. The function used to describe the energy distribution agrees with the data. Figure 5.6 displays again the 147.8 GeV electron beam energy distribution, but the parameterization is performed using the electron distribution $P_e(E)$ only, on a range of $\pm 3\sigma$ around μ.

The results obtained for the mean and width of the electron signal Gaussian distribution are the same using either a $\pm 3\sigma$ Gaussian fit on the electron peak, or a fit using an empirical function describing the pion contamination on the low energy data as well as to the electron peak. The pion contamination of the electron beams is therefore ignored in the analysis.

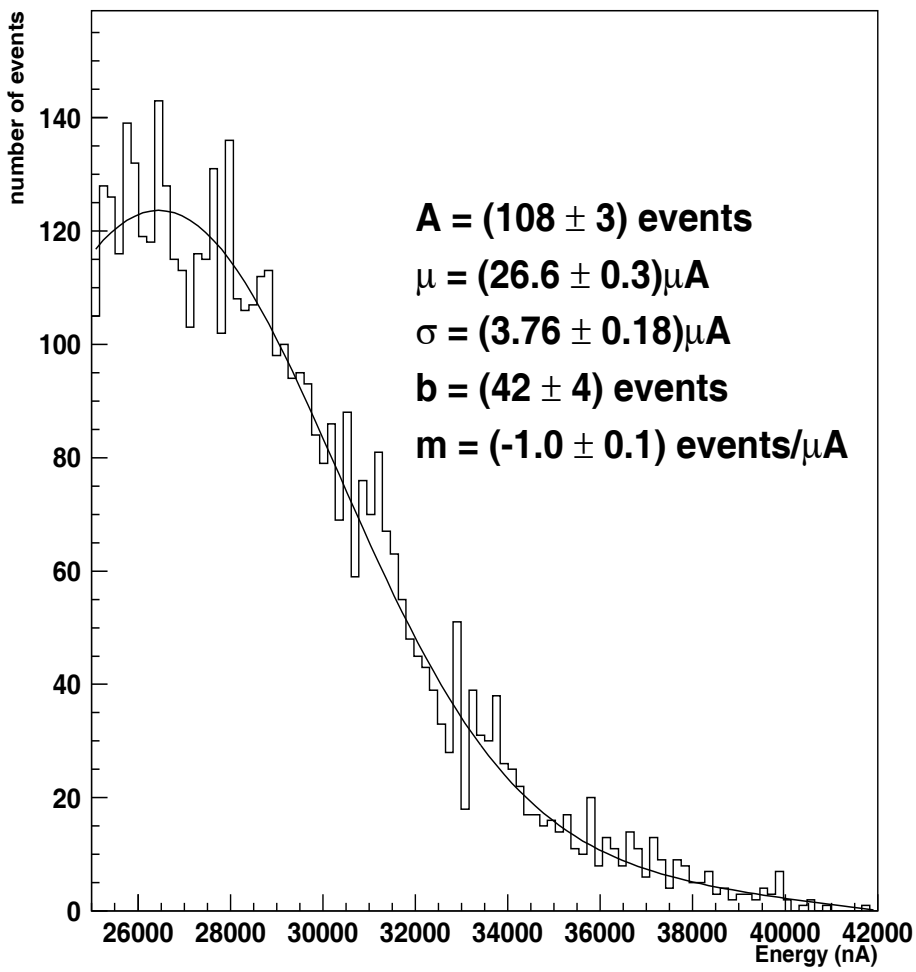

Figure 5.4: 150 GeV pion energy distribution using an electron cluster at impact point H. The empirical function used for the fit is a Gaussian (amplitude "A", mean "μ", and width "σ") summed with a first degree polynomial (slope "m", and intercept "b"). Note that $\chi^2/\text{ndf} = 92/88$.

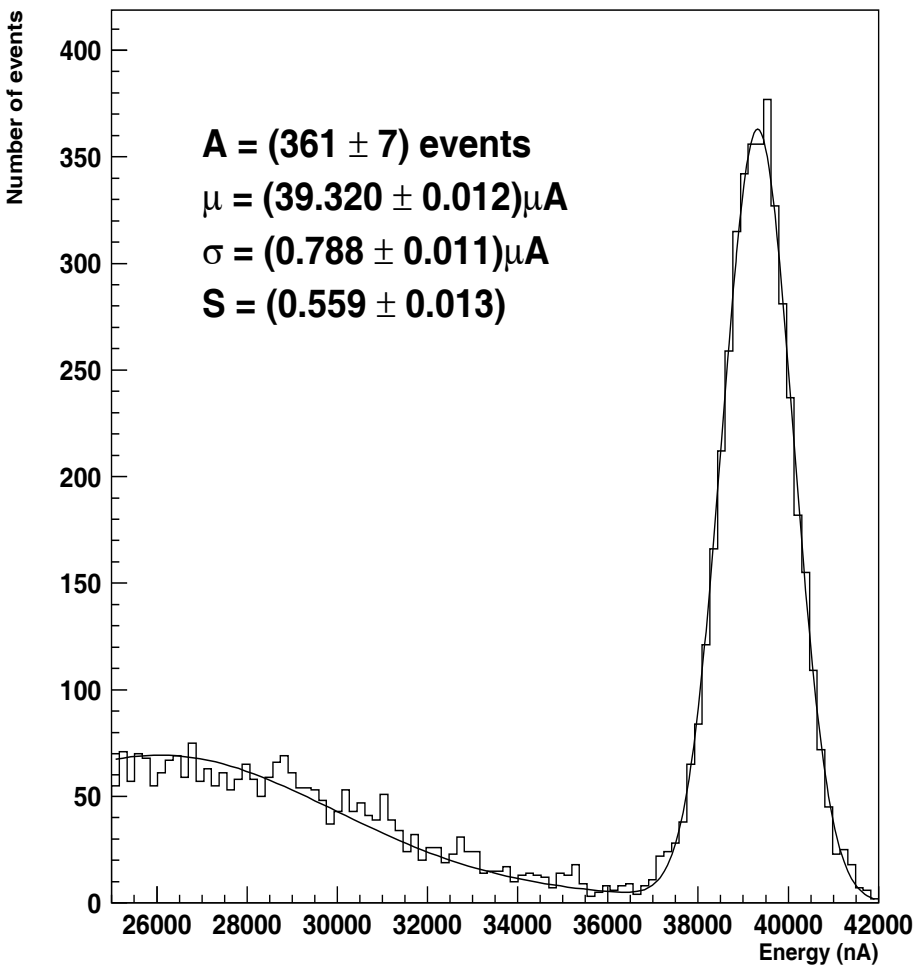

Figure 5.5: 147.8 GeV electron beam energy distribution. The curve represents a fit for the function describing the pion contamination and the electron signal. The function used for the fit is a Gaussian $P_e(E)$ (amplitude "A", mean "μ", and width "σ"), summed with the pion contamination function $P_\pi(E)$ scaled by a factor "S" (see text). $\chi^2/\text{ndf} = 105/96$.

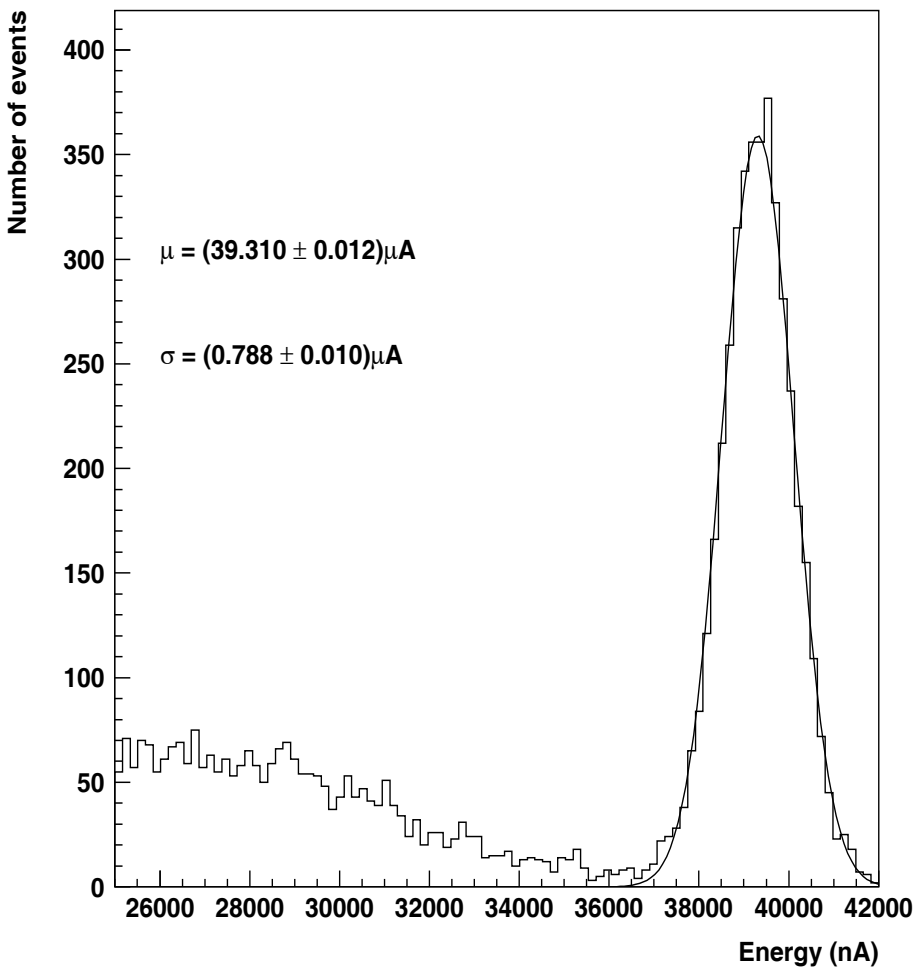

Figure 5.6: 147.8 GeV electron beam energy distribution with a simple normal distribution fit. The mean, $(39.310 \pm 0.012)\mu$A, and standard deviation, $(0.788 \pm 0.010)\mu$A, are within errors of the ones computed with the function describing the pion contamination (see Figure 5.5).

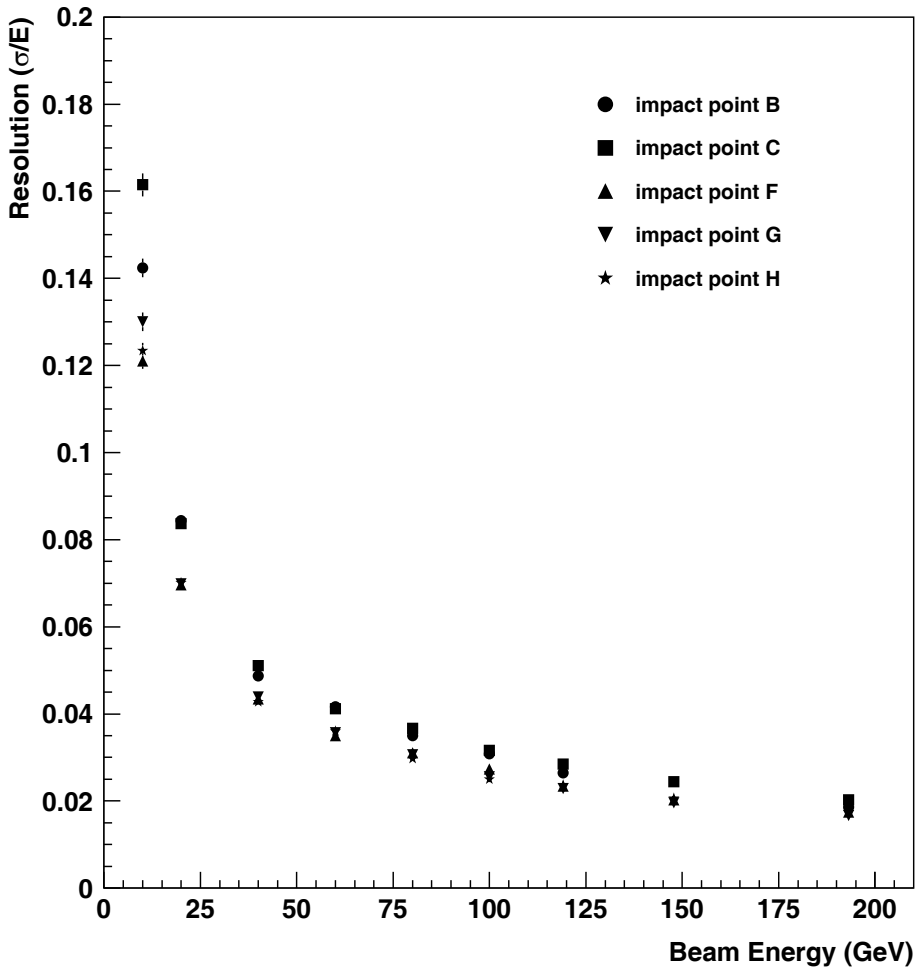

Figure 5.7: Electron energy resolution (σ/E) for all of the studied impact points. The parameters σ and E were obtained from the Gaussian fits performed on the energy distribution (Section 5.3).

5.5 Resolution

In order to evaluate the performance of the HEC, the energy resolution to electrons is studied. The energy resolution, σ/E, is calculated from the width, σ, and response, E(nA), obtained in Section 5.3. Figure 5.7 summarizes the resolution obtained for every beam energy at the 5 impact points studied. The resolution is worse at B and C due to the nearness of the beam with the tie-rods at those locations [33], causing a loss of energy (see Section 5.3). The effect of the tie-rods on the calorimeter response is examined in Section 5.6.

The energy resolution can then be parameterized as a function of energy as

$$\frac{\sigma}{E} = \frac{A}{\sqrt{E_0}} \oplus B \oplus \frac{C}{E}, \tag{5.6}$$

where E_0 is the electron initial energy (see Section 3.1.5). The parameterization assumes that the electronic noise is constant, but it was observed that the noise, σ_n varied through time, and is therefore different for each energy (see Section 4.3). However, since the electronic noise has been calculated separately, the noise term can be subtracted out in quadrature from the resolution such that only the intrinsic components are left. The intrinsic resolution is then expressed as

$$\frac{\sigma'}{E} = \frac{\sigma \ominus \sigma_n}{E} = \frac{A}{\sqrt{E_0}} \oplus B, \tag{5.7}$$

where the prime indicates that the electronic noise has been removed. The intrinsic resolution was thus calculated using the values of the electronic noise obtained in Section 4.3. Figure 5.8 shows the HEC intrinsic energy resolution at the 5 impact points studied as a function of the beam energy. The errors shown include the statistical and systematic errors. Details of the calculation of the intrinsic resolution error are discussed in Appendix C.

The sampling constant A and the constant term B for each impact point are obtained from a fit, and are presented in Table 5.2. The values of the sampling constant A are consistent for impact points F, G and H, whereas impact points B and C display a worse resolution and sampling term as expected.

A combined fit is made on the overall electron energy resolution and is presented in Figure 5.9. Only impacts F, G and H are used. The parameterization on the combined average yields

$$\frac{\sigma'}{E} = \frac{(23.29 \pm 0.09)\%}{\sqrt{E_0(\mathrm{GeV})}} \oplus (0.00 \pm 0.13)\%, \qquad \frac{\chi^2}{\mathrm{ndf}} = 23.4/7 \tag{5.8}$$

This result is incompatible with the values calculated using the April 1998 beam test data [31] [36][4]. The differences are mainly caused by the calibration procedure

[4] $\frac{\sigma'}{E} = \frac{(21.5\pm0.4)\%}{\sqrt{E_0(\mathrm{GeV})}} \oplus (0.0 \pm 0.4)\%$ (O'Neil), and $\frac{\sigma'}{E} = \frac{(22.0\pm0.1)\%}{\sqrt{E_0(\mathrm{GeV})}} \oplus (0.0 \pm 0.2)\%$(Dobbs et al.).

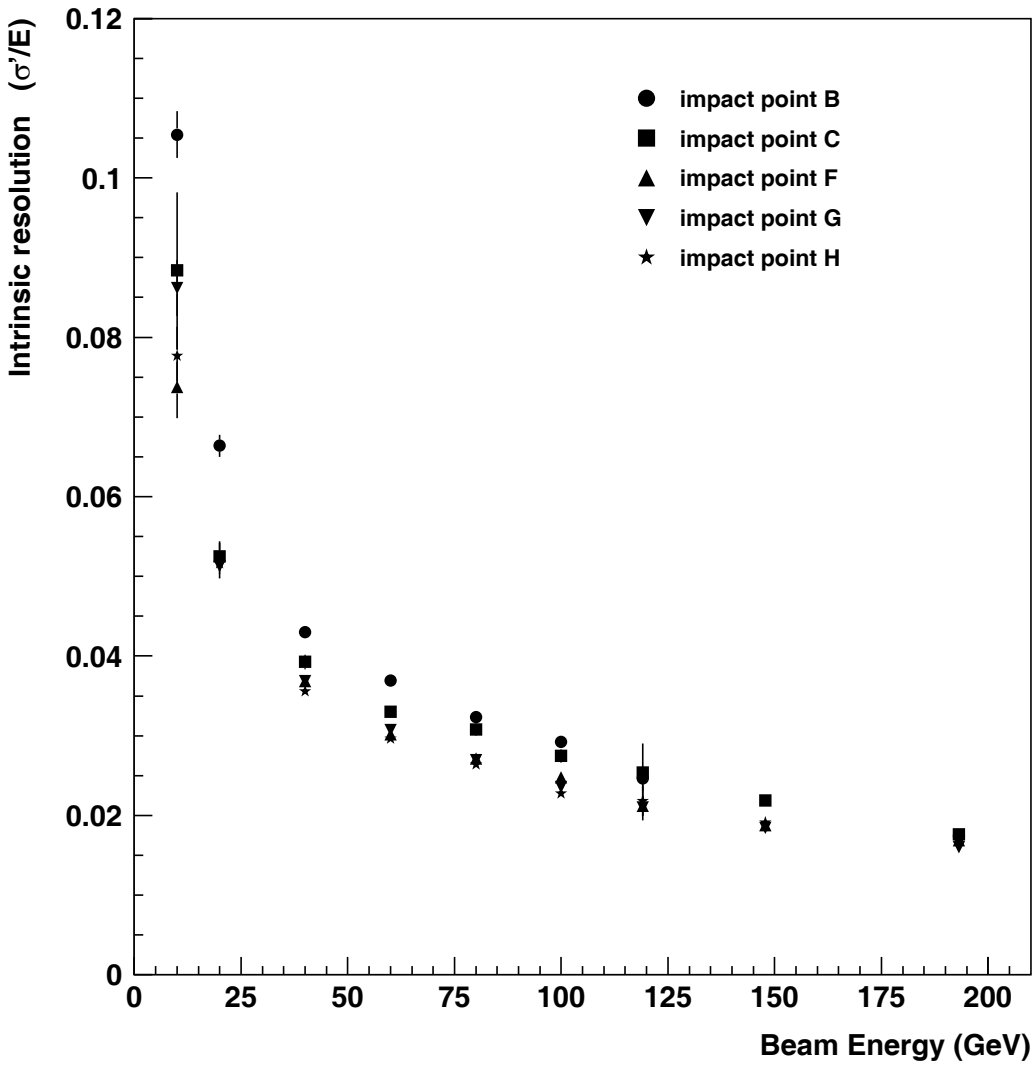

Figure 5.8: Electron intrinsic energy resolution (electronic noise subtracted) vs beam energy for the 5 impact points studied. The error bars include the statistical and systematic errors.

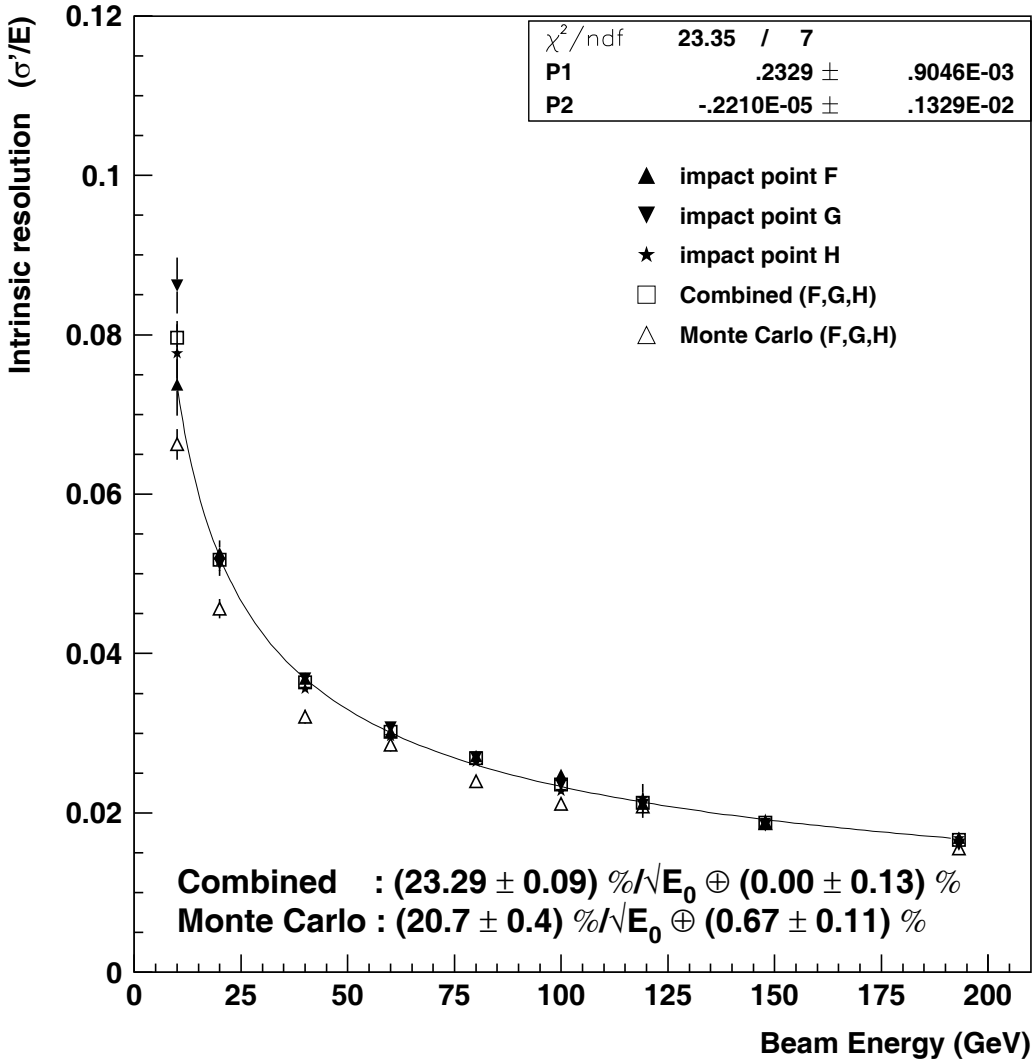

Figure 5.9: Combined electron intrinsic energy resolution (electronic noise subtracted) vs beam energy at impact points F, G, and H. The error bars are calculated from the RMS deviation of the resolution at the impact positions F, G, and H. The resolution from Monte Carlo simulations is also displayed.

Impact point	Sampling coef. (A) ($\%\sqrt{\text{GeV}}$)	Constant term (B) (%)	χ^2/ndf
B	27.1 ± 0.4	0.00 ± 0.14	56.2/7
C	25.5 ± 0.6	0.2 ± 0.6	27.1/7
F	23.65 ± 0.16	0.0 ± 0.4	13.5/7
G	23.18 ± 0.15	0.0 ± 0.12	33.6/7
H	22.8 ± 0.3	0.36 ± 0.15	6.01/7
Combined (F,G,H)	23.29 ± 0.09	0.00 ± 0.13	23.4/7
Monte Carlo (F,G,H)	20.7 ± 0.4	0.67 ± 0.11	11.0/7

Table 5.2: Resolution parameters for electrons for the 5 impact points studied. Impact points B and C suffer from their nearness with the tie-rods.

not being adequate in 1999 (Section 4.1.3), which caused the response to be different from one readout cell to another as will be shown in Section 5.6. Furthermore, the treatment of non-Gaussian tails in this analysis may lead to an underestimate of the effective electronic noise.

Monte Carlo electron studies of the calorimeter were also performed for impacts F, G and H and yielded an intrinsic resolution of

$$\frac{\sigma'}{E} = \frac{(20.7 \pm 0.4)\%}{\sqrt{E_0(\text{GeV})}} \oplus (0.67 \pm 0.11)\%, \qquad \frac{\chi^2}{\text{ndf}} = \frac{11.0}{7}. \tag{5.9}$$

The intrinsic resolution was obtained directly from σ/E [5] since neither electronic noise nor cell miscalibration were simulated in the Monte Carlo. The latter mainly accounts for the discrepancies between the Monte Carlo and the beam test data results.

[5] $\sigma/E = \sigma'/E$ for Monte Carlo simulations

5.6 Uniformity

Another point of interest for electron data is the uniformity of the response of the calorimeter. How does the response vary when electrons impinge on the calorimeter between two cells, or near a tie-rod ? To answer these questions, horizontal (X) and vertical (Y) scans with 147.8 GeV electron beams were performed. These scans are a collection of runs where the impact point of the beam is changed by steps of 10.0 mm. Using the multi-wires proportional chambers (MWPCs), it is possible to know where each electron enters the calorimeter with a precision of ($\pm 1/\sqrt{12}$) mm [44]. Figure 5.10 shows how the relative response (energy reconstructed using the average α_{em} over the energy of the beam) varies with the impact point as the electron beam moves from cell 33 to cell 37. X = -5.1 mm is located between cells 33 and 37, in the central module (see Figure 5.1) and is plotted in Figure 5.10 as a vertical line. The difference in response comes mainly from the miscalibration of cells 33 relative to cell 37, where most of the electron energy is measured, as shown in Figure 5.11. The range in the difference of the response is around 2.4%. This change in the response agrees with the 2.3% difference between the electromagnetic scales computed for impact points G and F (see Table 5.1) which correspond to a beam centered on cells 33 and 37, respectively.

A vertical scan with a 147.8 GeV electron beam was also made in the same manner described above, between locations corresponding to the area covered by cells 33 and 57 (impact points G and C). Using this scan, the effect of the tie-rod in the response of the calorimeter is studied. Figure 5.12 shows how the response behaves as electrons approach a tie-rod. The tie-rod is located in cell 57, as shown in Figure 4.1, at about Y = 16.0 cm. The response starts dropping dramatically around Y = 14.0 cm (the location of impact point C is at Y = 13.4 cm) and goes down by nearly 20% at the tie-rod. Since the beam has a radius of about 1.25 cm (see Section 4.1.2), some of the electrons for a beam collimated at impact C are within the effective drop-off range of the tie-rod. This effect explains why α_{em}

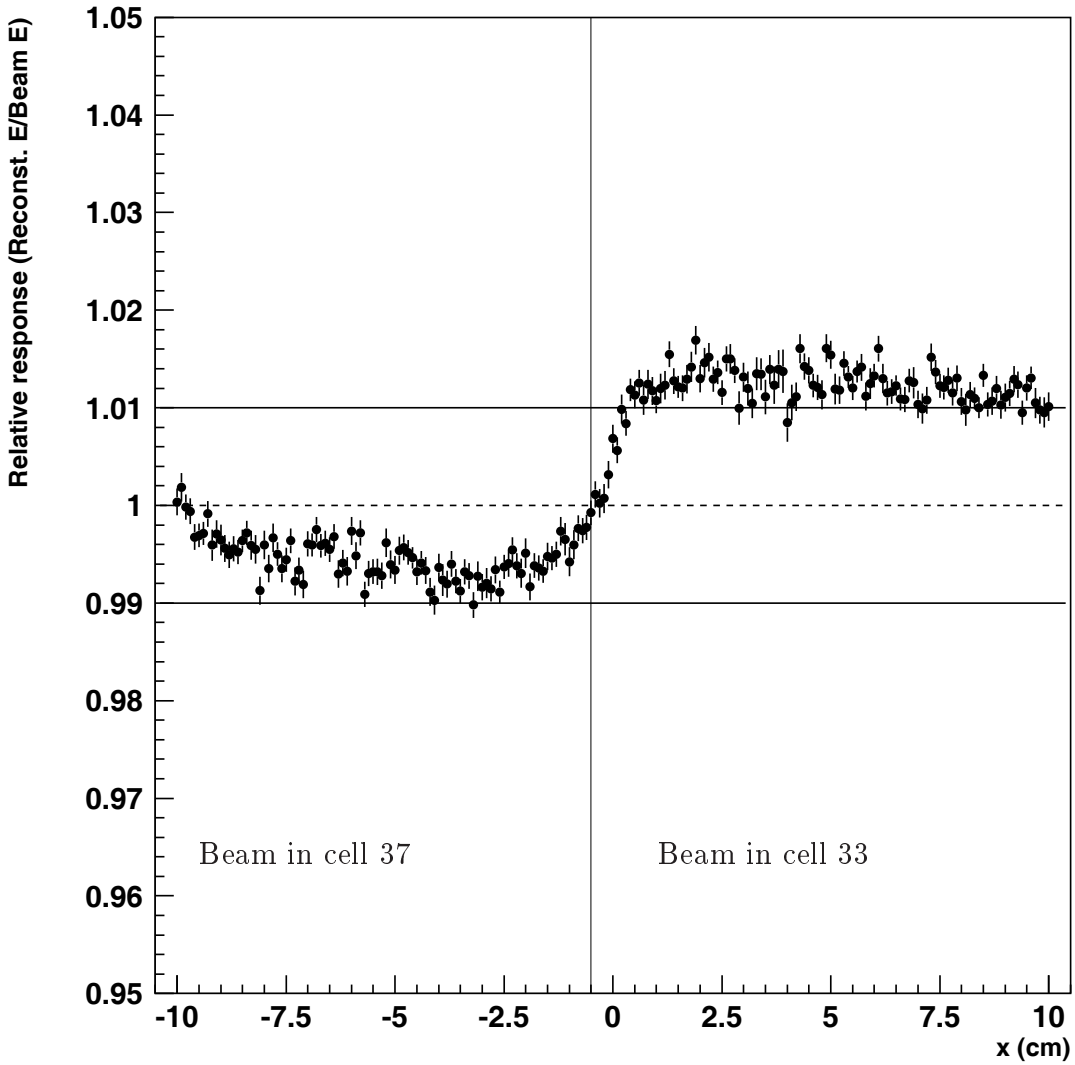

Figure 5.10: Relative response of the calorimeter vs. beam location for 147.8 GeV electrons. The cluster selected for reconstruction was the same for all events and all positions. The error bars shown are purely statistical. Y = -39 mm.

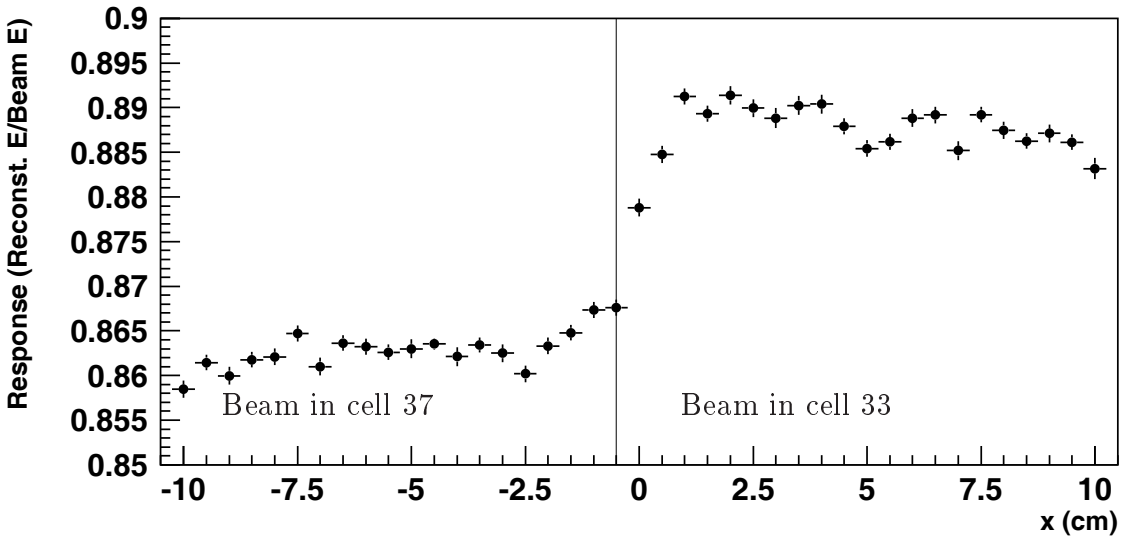

Figure 5.11: Relative response from cells 33 and 37 vs. Beam location for 147.8 GeV electrons. The response is the sum of the signal from cells 33 and 37 only. The difference between the signal across the symmetry axis (X = -5.1 mm) is about 2.4%. The error bars shown are purely statistical.

is higher for impact points B and C than for the three other impact points (see Table 5.1). It is also the reason why the resolution and the sampling constant term at points B and C are larger than the value obtained by the combined fit.

From previous beam test analyses, the problems encountered in the uniformity of the response of the calorimeter to electrons are understood to be due to cell miscalibration. This affects the calculation of α_{em} and the resolution. The presence of tie-rods near impact points B and C has an even greater effect on the response of the calorimeter. But this effect will be less noticeable in ATLAS since particles will not come in a direction parallel to the rods (see Figure 4.2), but at an angle. In fact, in ATLAS, the tie-rods of the HEC will be parallel to the beam pipe, meaning that any particle/shower will cross the tie-rods at an angle (see Figure 2.2). Furthermore, the showers measured in the Endcap will be hadronic, such that the shower will spread much more than in the case of electromagnetic showers (Sections 3.1.1 and 3.1.2). Therefore, a smaller fraction of the total shower energy will be 'lost' in the tie-rods.

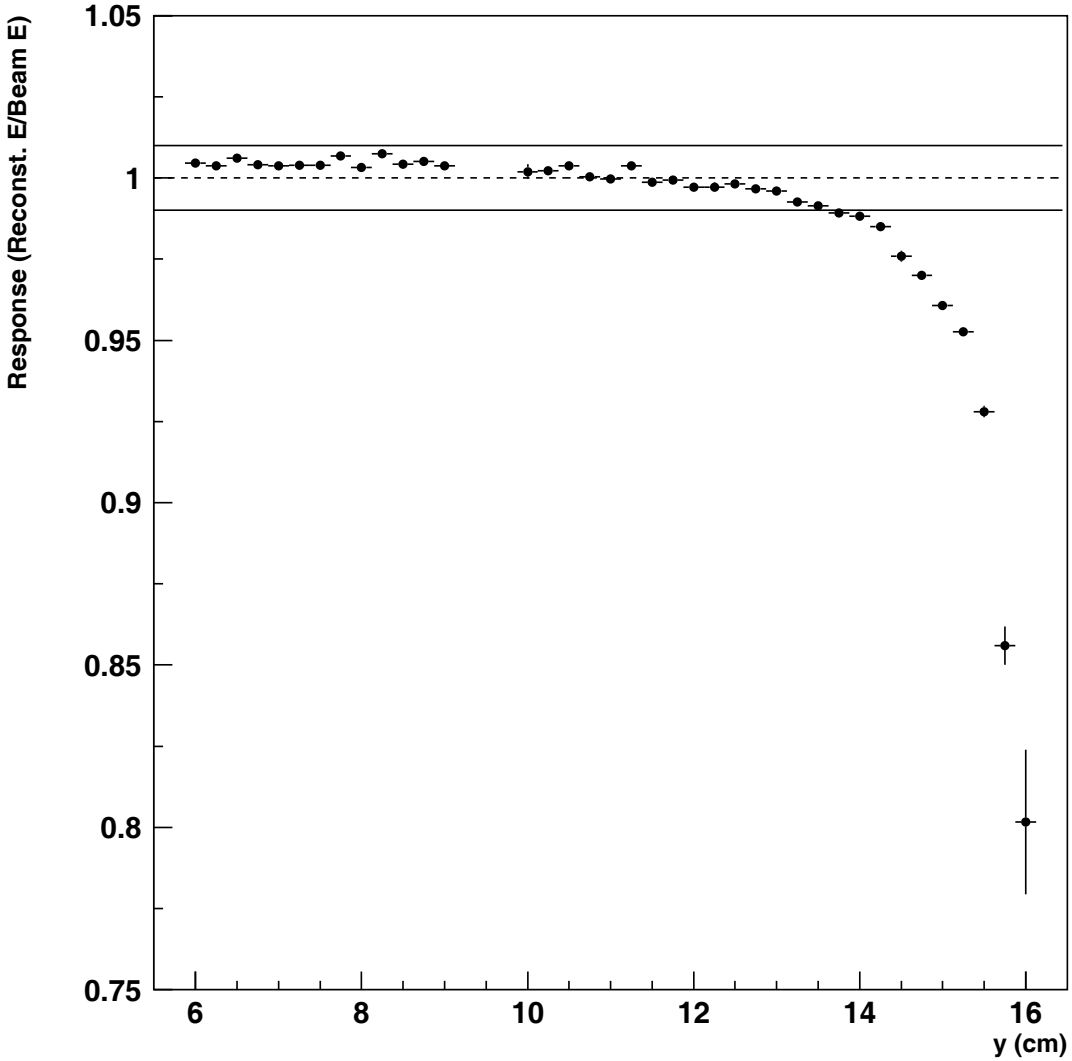

Figure 5.12: Response of the calorimeter vs. beam impact for 147.8 GeV electrons. The cluster selected for reconstruction is the same for all events and all positions. The error bars shown are purely statistical. X = 80 mm. Note how the response drops as the electrons are getting closer to the tie-rod (Y = 16.0 cm).

Chapter 6

Analysis of Pion Beam Test Data

The intrinsic performance of the Hadronic Encap Calorimeter to hadrons is determined by studying the response and resolution of the calorimeter to pions. For each of the selected impact locations, the modules were subjected to pion beams of 10, 20, 40, 60, 80, 100, 120, 150, 180, and 200 GeV. Each run is typically made up of 10,000 events, of which 25% to 90% pass the trigger cuts. The readout cell signal for each event is reconstructed using the digital filtering method (Section 4.2.2). Because of the different nature of the processes involved in hadronic showers, larger clusters were used to achieve full or nearly full containment of the showers. The response and the intrinsic energy resolution of the HEC to pions is presented in this chapter and the resolution is compared with the values obtained from Monte Carlo simulations. Finally, the electromagnetic to hadronic response ratio, e/h, is evaluated.

6.1 Trigger cuts

In order to remove impurities from the pion sample, the triggers presented in Section 4.1.2 were applied and include a physics trigger requirement (pre-trigger), and a pile-up and random veto. Again, the limitation of the Cherenkov detector to low energies prevented its use in eliminating electron impurities from the beam. Nonetheless, software cuts were sufficient to remove electrons from the pion data sample. Muon events were removed by using the muon trigger, but some impurities

were observed for low energy runs. The number of pion events satisfying the above cuts ranged from about 2600 to 9200 events for all of the runs.

6.2 Clustering

Full or nearly full containment of the hadronic showers has to be achieved in order to study the intrinsic properties of the calorimeter. Hence, 54 cells clusters are used to reconstruct the energy of the pions. Figure 6.1 displays the distribution of the cells for such a cluster, selected for impact point G. In the case of impacts B and F, 53 cells clusters are used because of a dead ADC channel (cell 91) in the 3rd depth. The clusters used for pion data analysis are much larger than the ones used for electron runs because the hadronic showers are developing much further in the detector and are much broader (see Section 3.1.2). The down side of using these large clusters is that the total electronic noise is much greater than the one in electron clusters (see Section 4.3).

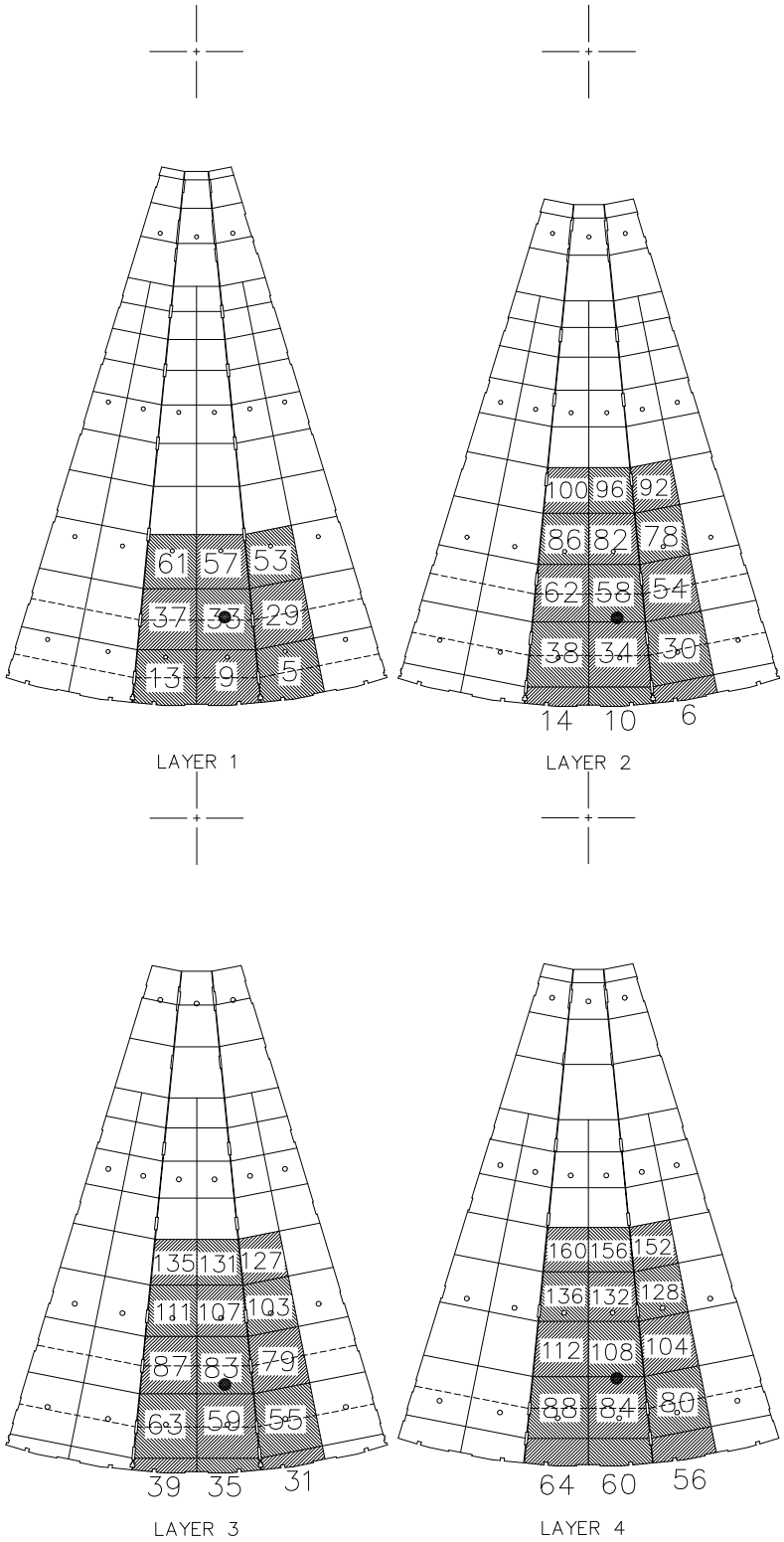

Figure 6.1: Distribution of a 54 cell cluster designed for pion runs at impact point G. The beam path through the calorimeter is denoted by a star. The shaded cells are cells used in the cluster. The number appearing at the center of each cell corresponds to the readout channel number.

6.3 Response

In order to calculate the response of the HEC to pions, the procedure described in Section 4.2 is used. As for the electron analysis (Section 5.3), the response of the HEC to pion is then corrected by subtracting the cluster noise most probable current from the cluster signal (observed in the pedestal region, see Section 4.3). This correction increases the response significantly at low energy, as it was shown in Figure 5.3.

Figure 6.2 shows the energy deposited (expressed in nA) in a cluster for 10 to 150 GeV pion beam. Muon events can be seen for beams of low energy (peak centered near 0 GeV). Non-Gaussian tails are also present on the high energy side of the energy distribution and are caused by high electronic noise as discussed in Section 4.3. These tails do not significantly affect the values of the mean (μ_E) and width (σ) of the pion response obtained from Gaussian fits. These fits are performed on a region contained between $\pm 2\sigma$ from the mean. For the 10 and 20 GeV pion beams, the fits are done from -1.75σ to +2σ to avoid muon contamination.

Since the HEC is non-compensating, the response to hadrons is not linear, but increases with energy [1]. This phenomenon was described in Section 3.1.4 and can be observed in Figure 6.3. The left axis on Figure 6.3 shows the pion response after subtracting the cluster noise most probable current, E(nA) (or π), plotted on an electromagnetic scale [2], which contains information about the degree of non-compensation of the calorimeter. The values of α_{em} at each impact position (Table 5.1) are used to reconstruct the pion energy, which reduces calibration problems. On the right axis, the response using the pion scale is shown.

Even though the calorimeter provides good longitudinal containment of hadronic showers, Monte Carlo studies show that there is some leakage of energy, mainly at the bottom of the calorimeter. The total energy loss is about $(3.2 \pm 0.5)\%$ [3].

[1] f_{π^0} is proportional to the logarithm of the energy, such that the shower electromagnetic content and hence the response increase.

[2] In other words, the response is calculated as $\alpha_{em}\pi/E_0$.

[3] This value is independent of the beam energy, and is in agreement with previous results [18].

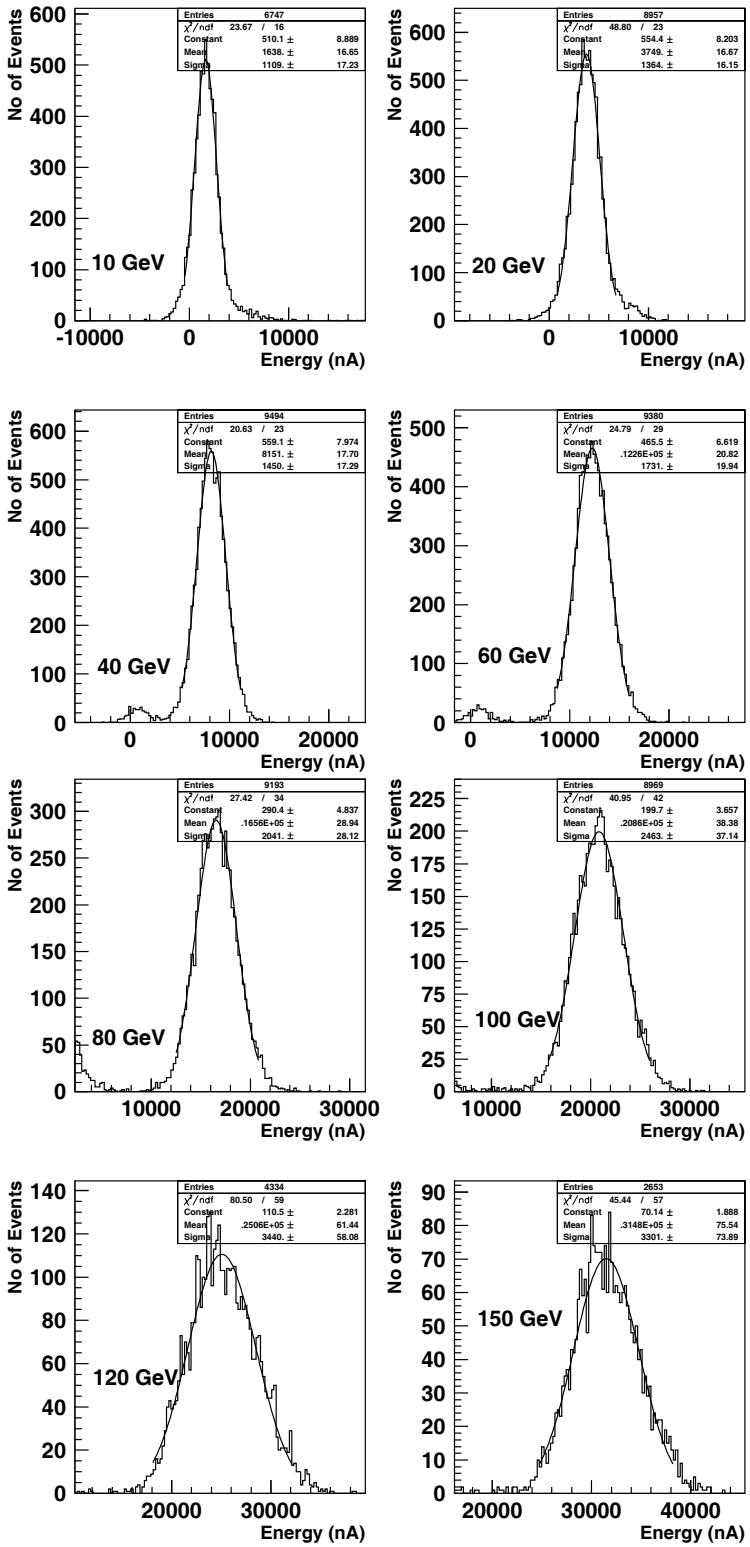

Figure 6.2: Response of the HEC to pion beams in units of current measured at impact point G for 10, 20, 40, 60, 80, 100, 120 and 150 GeV. A Gaussian fit was performed on a region between $\pm 2\sigma$ of the most probable signal for runs with beam energy greater than 20 GeV, and from -1.75σ to $+2\sigma$ for the 10 and 20 GeV beams.

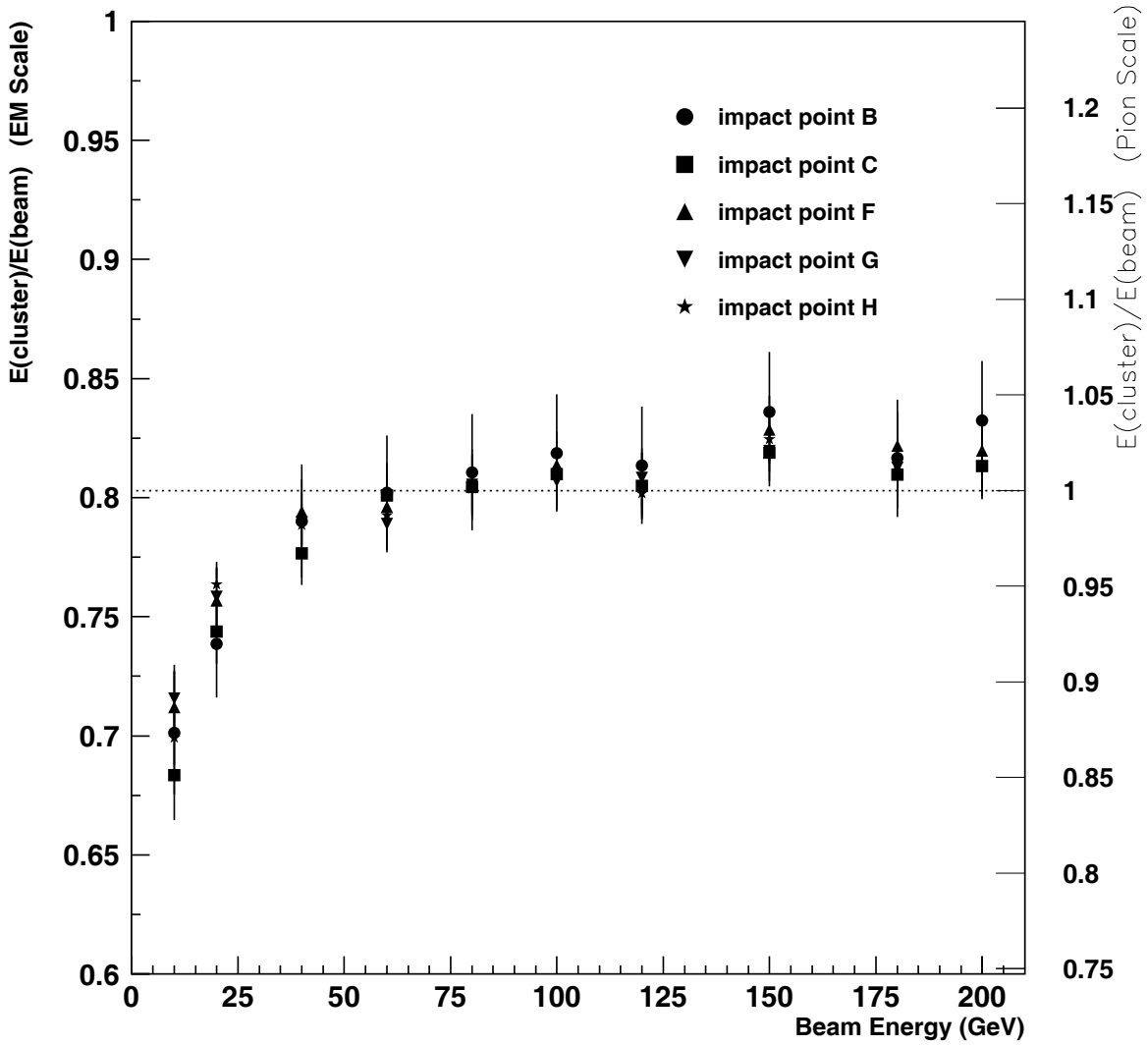

Figure 6.3: HEC response to pion vs. beam energy using the electromagnetic scale (left) and pion scale (right). The electromagnetic scale factors are presented in Tables 5.1. The pion scale, which allows one to convert the pion cluster energy from nA to GeV, is calculated using Equations 5.1 and 5.2 applied to pion data. It is only an approximation since the calorimeter response to pion is not linear.

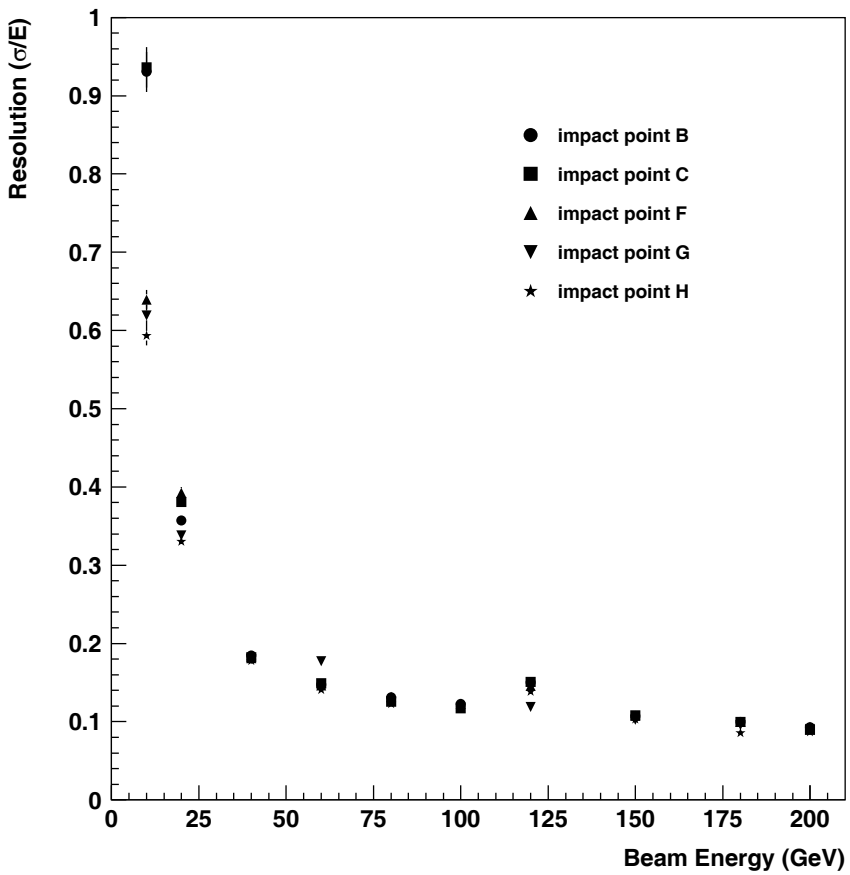

Figure 6.4: Pion energy resolution vs. beam energy for the 5 impact points studied. The error bars include the statistic and systematic errors. The parameters σ and E were obtained from the Gaussian fits performed on the energy distribution.

6.4 Resolution

The performance of the calorimeter is also assessed in terms of the HEC energy resolution to pion. The energy resolution is calculated using the values of σ and E(nA) [4] obtained in the previous section (Section 6.3). Figure 6.4 displays the resolution obtained for every beam energy at each of the 5 impact points studied. The resolution is shown to be consistent for impact points B and C, and for impact points F, G and H.

As discussed previously in Section 5.5, the electronic noise can be subtracted out

[4] E(nA) is the response of the calorimeter after subtracting the cluster noise most probable current, as described in Appendix C.

in quadrature from the resolution. By doing so, only the intrinsic components of the resolution are left and the parameterization reduces to the expression presented in Equation 5.7. The intrinsic resolution was thus calculated using the values of the cluster electronic noise obtained in Section 4.3. Figure 6.5 shows the HEC intrinsic energy resolution at the 5 impact points studied as a function of beam energy. The errors shown include the statistical and systematic errors. Details of the calculation of the intrinsic resolution error are reviewed in Appendix C.

The sampling constant A and the constant term B for each impact point are obtained from a fit, and are presented in Table 6.1. The values of the sampling constant A are consistent for impacts B and C, and for impacts F and G, whereas impact point H displays a better resolution.

As it can be seen in Table 6.1, the resolution obtained in beam test for each impact point is worse than the resolution obtained by Monte Carlo simulations using G-CALOR. This may be due again to the electronic noise and cell miscalibration not being included in the simulations. The latter mainly accounts for the discrepancies between the Monte Carlo and the beam test data results. It was also shown previously that hadronic simulations overestimated the calorimeter response, and hence produced a better resolution [18].

Combined fits are performed using the weighted average resolution for each energy for impacts B and C, and F, G, and H. The results obtained are shown in Figures 6.6 and 6.7 respectively. The overall combined average parameterization of the resolution obtained from experimental data is

$$\frac{\sigma'}{E} = \frac{(76.2 \pm 0.9)\%}{\sqrt{E_0(\mathrm{GeV})}} \oplus (6.68 \pm 0.09)\%. \qquad \frac{\chi^2}{\mathrm{ndf}} = 15.37/8 \tag{6.1}$$

The sampling constant A is compatible with the value obtained in 1998 [5] [36], but the constant term B is 33% larger than previously. This difference in the constant term is mainly caused by the calibration procedure not being adequate in 1999 (Section 4.1.3). Moreover, the treatment of non-Gaussian tails in this analysis may

[5] $\frac{\sigma'}{E} = \frac{(78\pm2)\%}{\sqrt{\mathrm{E_0(GeV)}}} \oplus (5.0 \pm 0.3)\%$.

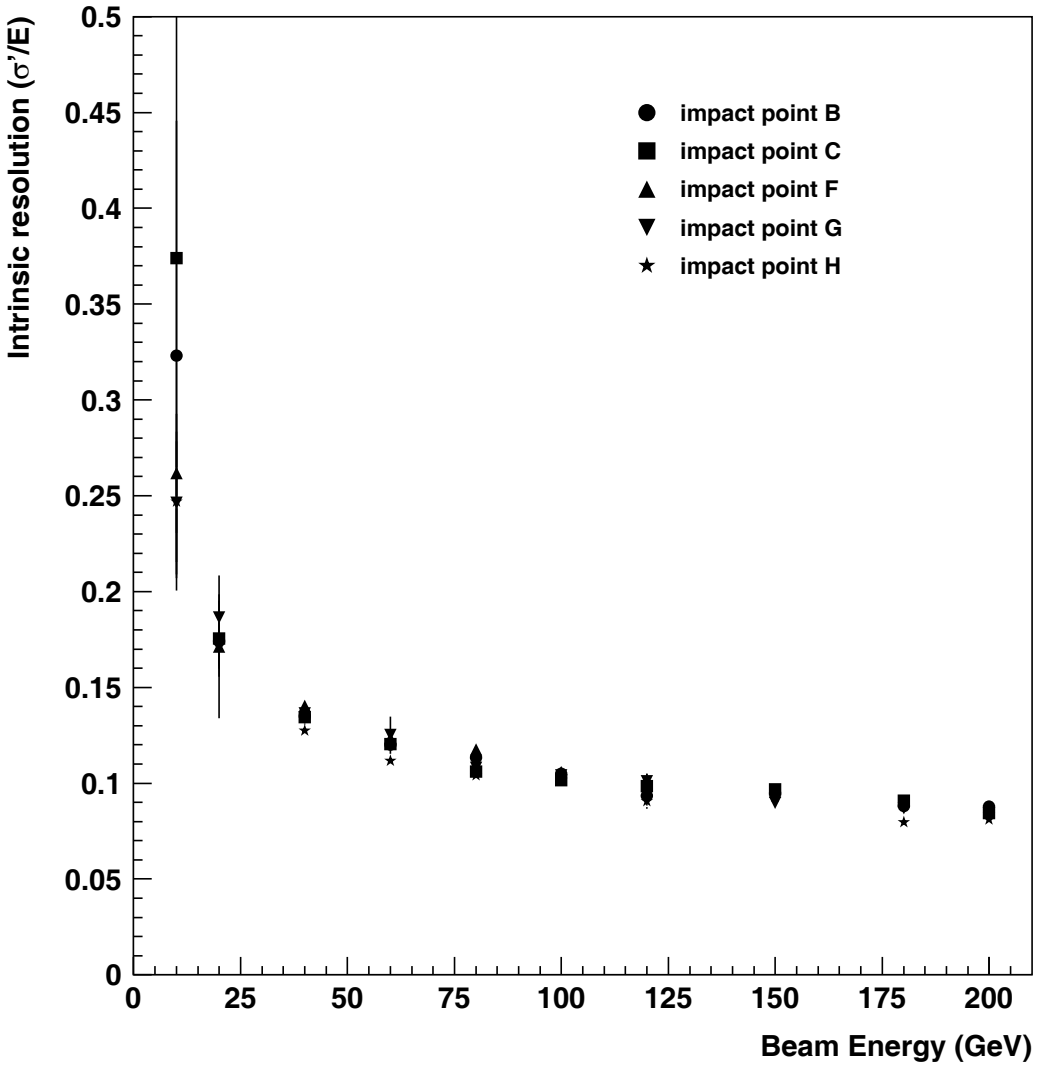

Figure 6.5: Pion intrinsic energy resolution vs. beam energy at the 5 impact points studied. The error bars shown include the statistical and systematic errors.

Impact point	Sampling coef. (A) ($\%\sqrt{\text{GeV}}$)	Constant term (B) (%)	χ^2/ndf
B	76 ± 2	7.0 ± 0.2	6.42/8
C	76 ± 2	6.7 ± 0.2	9.08/8
Combined (B,C)	75.6 ± 1.5	6.85 ± 0.15	7.57/8
Monte Carlo (B,C)	64.5 ± 0.8	5.51 ± 0.10	17.1/8
F	80 ± 2	6.8 ± 0.2	8.06/8
G	77 ± 2	6.6 ± 0.2	4.47/8
H	72 ± 2	6.4 ± 0.2	16.6/8
Combined (F,G,H)	76.6 ± 1.2	6.57 ± 0.12	12.7/8
Monte Carlo (F,G,H)	65.7 ± 0.9	5.87 ± 0.11	9.03/8
Combined (B,C,F,G,H)	76.2 ± 0.9	6.68 ± 0.09	15.4/8

Table 6.1: Resolution parameters obtained for $\pi^{\pm}$ beams for the 5 impact points studied. The combined average for the calorimeter is given. The corresponding Monte Carlo results are also presented.

lead to an underestimate of the effective electronic noise. An analysis conducted at the Max-Plank-Institut für Physik also yielded a larger constant term for 1999 [6] [33].

6.5 Determination of e/h

The ratio of electromagnetic to hadronic response, e/h, is a fundamental parameter which sets the limits on the calorimeter's intrinsic resolution to hadrons. As mentioned in Section 3.1.4, the HEC is expected to be non-compensating ($e/h > 1$). This ratio cannot be measured directly, since the electromagnetic component f_{π^0} of hadronic shower varies as the logarithm of the energy (see Equation 3.1.2). The ratio e/h can be estimated by studying the response of the calorimeter to pions, π. The latter is a combination of the purely electromagnetic (e) and hadronic (h) responses

$$\pi = e f_{\pi^0}(E) + h(1 - f_{\pi^0}(E)), \tag{6.2}$$

[6] $\frac{\sigma'}{E} \approx \frac{75\%}{\sqrt{E_0(\text{GeV})}} \oplus 6\%$.

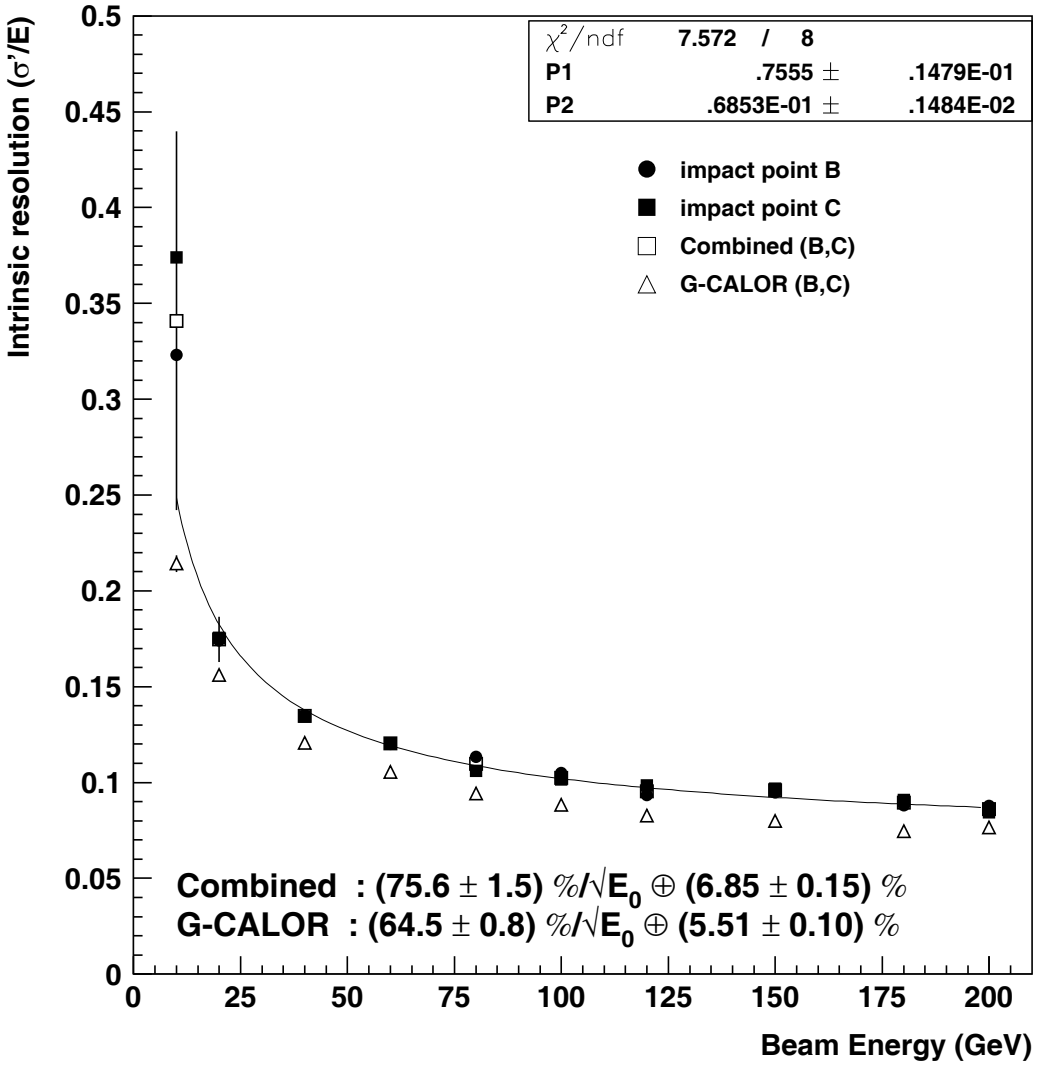

Figure 6.6: Combined pion intrinsic energy resolution vs. beam energy at impact points B and C. The error bars were calculated from the RMS deviation of the resolution at impact points B and C. The resolution from Monte Carlo (MC) is also displayed.

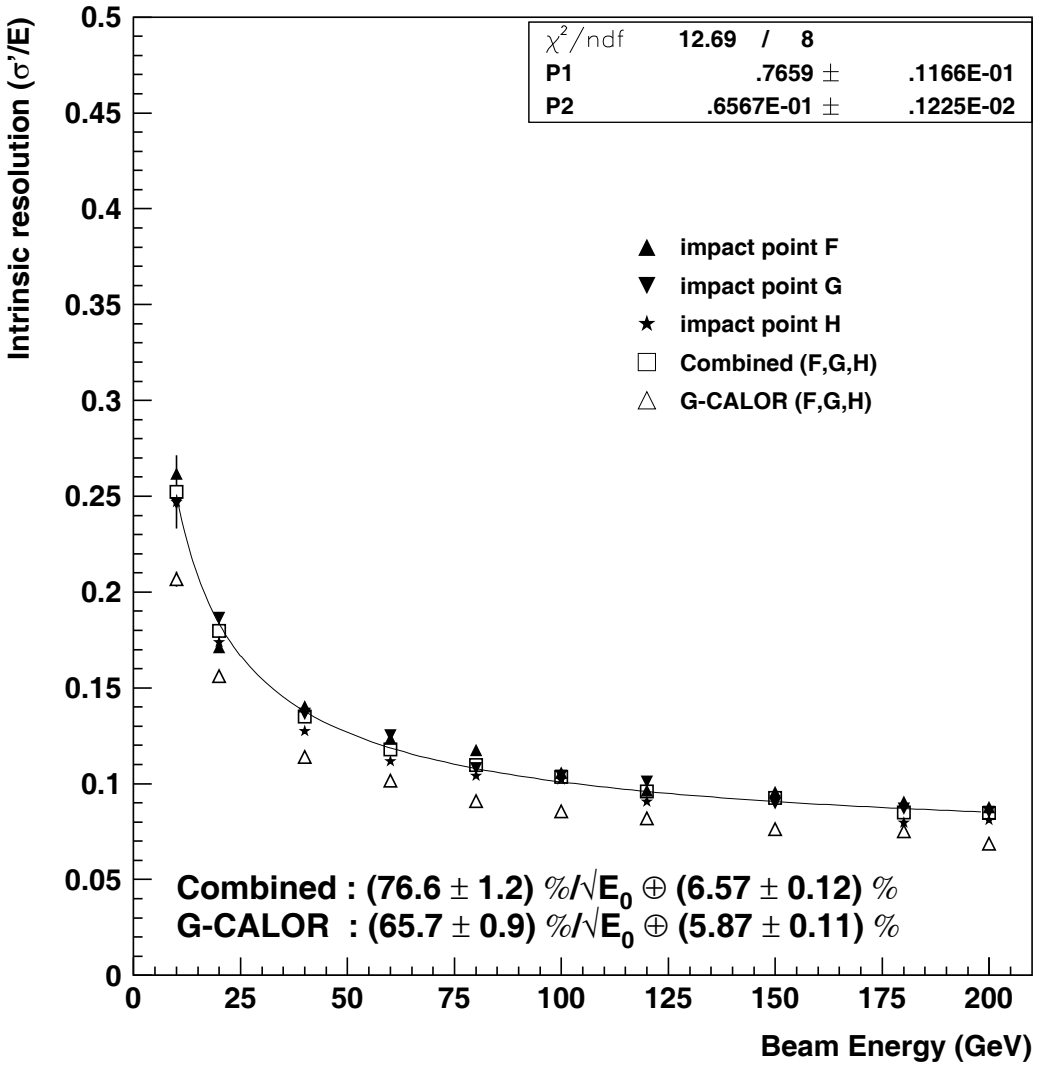

Figure 6.7: Combined pion intrinsic energy resolution vs. beam energy at impacts F, G and H. The error bars were calculated from the RMS deviation of the resolution at impact points F, G, and H. The resolution from Monte Carlo (MC) is also displayed.

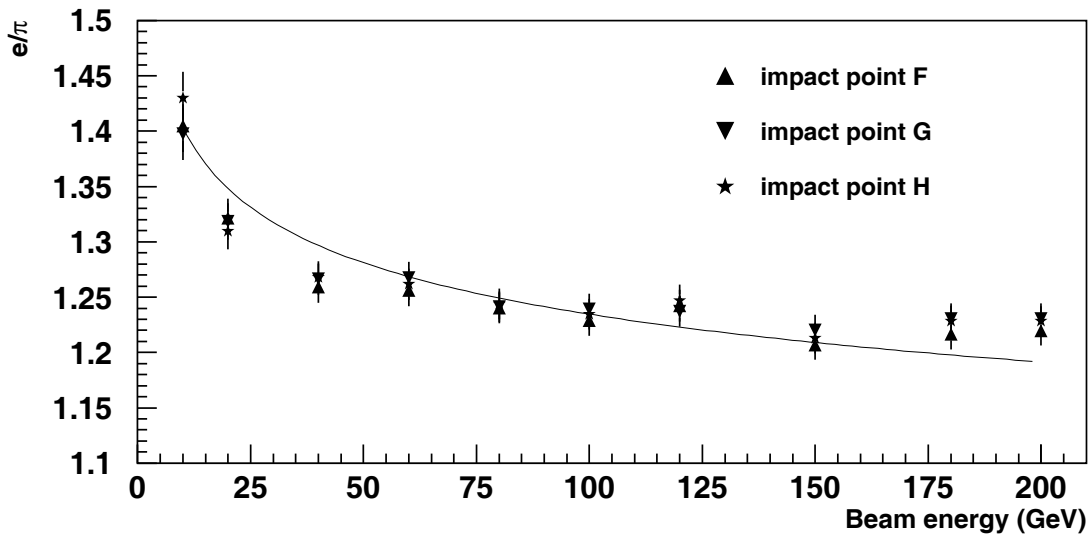

Figure 6.8: Energy dependence of the electron to pion response ratio *before* energy leakage corrections. The ratios for impact points F, G and H are presented. The line is the result of a fit to all the data points using Wigman's parameterization. The values of e/h obtained are presented in Table 6.2.

such that

$$\frac{e}{\pi} = \frac{e/h}{1-(1-\frac{e}{h})f_{\pi^0}(E)}, \tag{6.3}$$

where $f_{\pi^0}(E) = 0.11\ln(E(\text{GeV}))$ [26]. The response to pions, $E_\pi(\text{nA})$, measured in Section 6.3 corresponds to π. Similarly, the response to electrons, $E_e(\text{nA})$, measured in Section 5.3 corresponds to e. The ratio of the electron to pion response is then

$$\frac{e}{\pi} = \frac{\alpha_{em}E_e(\text{nA})}{\alpha_{em}E_\pi(\text{nA})} = \frac{E_0}{\alpha_{em}E_\pi(\text{nA})}. \tag{6.4}$$

After evaluating $f_{\pi^0}(E)$ at each energy and substituing Equation 6.4 into Equation 6.3, e/h is the only unknown left in Equation 6.3. It can be extracted by a fit over the e/π data, as shown in Figure 6.8. Only the data for impacts points F, G and H are displayed. The analysis is not performed for impacts B and C because of their nearness with tie-rods which caused problems in evaluating α_{em} (see Section 5.3). Equation 6.3 used to estimate e/π, and hence e/h, assumes that the shower is fully contained within the detector. But Monte Carlo studies indicate that in the 1999 HEC beam test there is a leakage of the hadronic shower energy at the bottom of the

Impact Position	e/h_{eff}	χ^2/ndf	e/h	χ^2/ndf
F	1.611 ± 0.014	17.6/9	$1.499 \pm 0.014 \pm 0.016$	9.70/9
G	1.626 ± 0.015	23.8/9	$1.513 \pm 0.014 \pm 0.016$	11.0/9
H	1.628 ± 0.014	26.6/9	$1.514 \pm 0.014 \pm 0.016$	15.8/9
Combined (F,G,H)	1.622 ± 0.014	21.7/9	$1.509 \pm 0.014 \pm 0.016$	11.3/9

Table 6.2: Electromagnetic to hadronic response ratio with energy leakage corrections (e/h) and without (e/h_{eff}). The correction for the energy leakage significantly improves the agreement with the parameterization. The systematic error on α_{em} dominates the final error on e/h_{eff}, whereas the error on e/h also depends significantly on the error on the energy leakage correction (second error).

calorimeter of about $(3.2 \pm 0.5)\%$ for any given beam energy (Section 6.3). This loss of energy produces an overestimate of the true e/h. The ratio of electromagnetic to hadronic response measured in Figure 6.8 can then be seen as the effective ratio of the responses, e/h_{eff}. The systematic error on α_{em}, mainly due to the observed small non-linearity of the electron response (see Section 5.3), dominates the final error on e/π. Since this error is highly correlated for all impact points at a given energy, a combined fit is performed on the average e/π calculated over impact points F, G, and H for each energy. The error on this average is taken from the average error on e/π for the 3 impact points. The results obtained for the 3 impact points studied and the combined fit are shown in Table 6.2.

The pion response is then corrected by including the leakage energy. The results obtained after correction are presented in Figure 6.9. The values of e/h extracted for the 3 impact points studied are shown in Table 6.2. The theoretical model is shown to agree better with the data after applying the correction as seen by the improved χ^2. The second error shown is due to the uncertainty on the energy leakage correction, and is estimated by varying the energy leakage by one standard deviation and re-performing the fits. The overall parameterization yields a ratio of $e/h = 1.509 \pm 0.021$, which is in agreement with the 2000 measurement [7] [46]. The e/h was also measured at each energy as shown in Figure 6.10.

[7] A. Minaenko obtained an average measurement of $e/h = 1.50 \pm 0.05$.

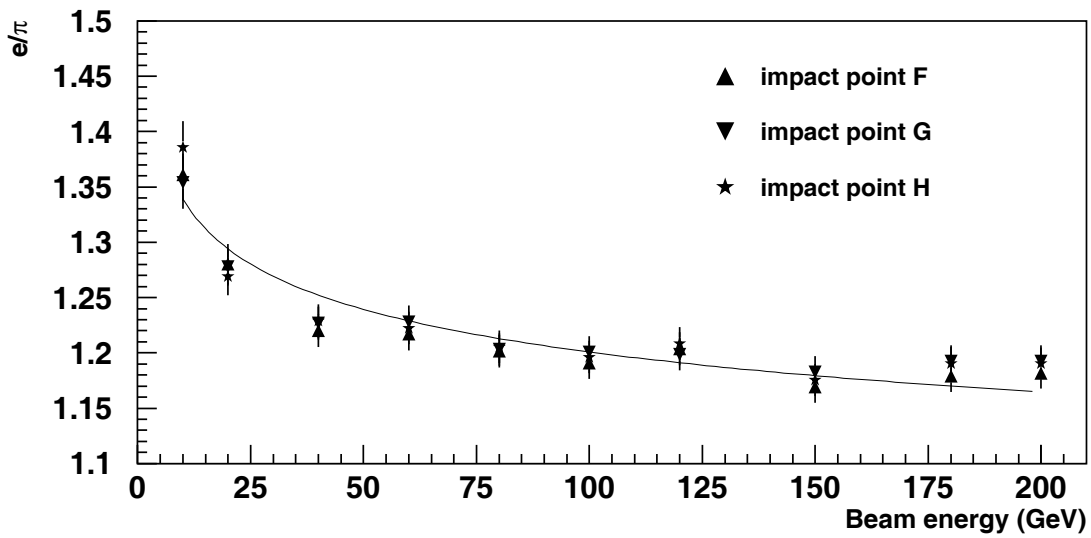

Figure 6.9: Energy dependence of the electron to pion response ratio *after* energy leakage corrections. The ratios for impact points F, G and H are presented. The line is the result of a fit to all the data points using Wigman's parameterization. The results obtained for e/h are presented in Table 6.2.

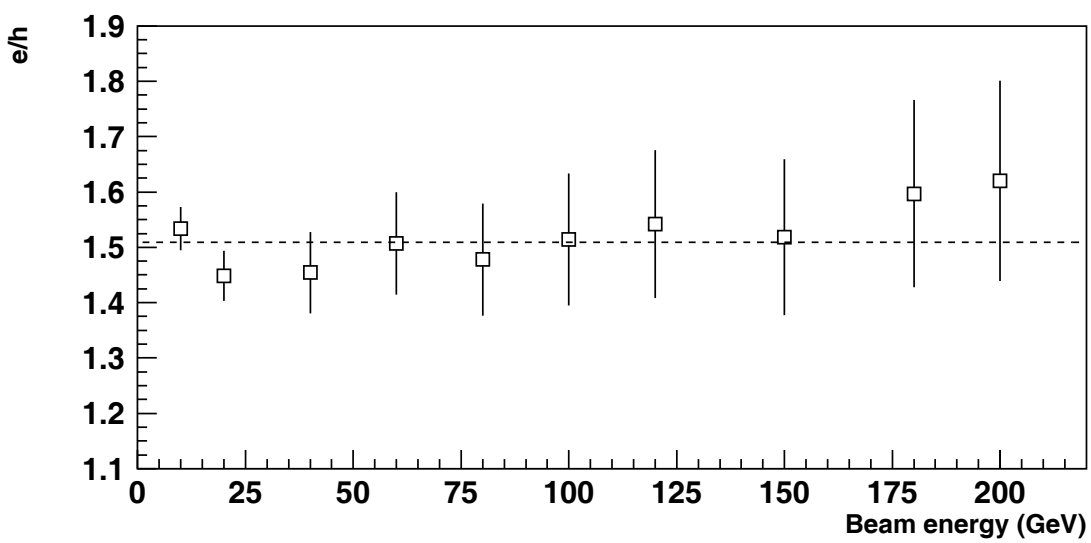

Figure 6.10: Individual measurement of e/h *after* energy leakage corrections for each of the 10 beam energies. The ratios obtained for impact point G only are presented. The dotted line represents the average e/h measured from a fit on all the data points using Wigman's parameterization.

Studies of the ATLAS calorimetry system have shown that measurements of e/h for fast readout calorimetry tends to be overestimated because of low energy cut-off and charge collection time [47]. Since the hadronic showers spread to several readout cells, the signal-to-noise ratio is poor in many of those readout cells creating a low energy cutoff, which leads to an overestimate of e/h. Also, the ATLAS hadronic calorimeters have been designed to operate with fast-readout of the signals, which causes the slow component of hadronic shower to be missed (see the discussion about the spallation model in Section 3.1.2). Since there is no such slow process in electromagnetic showers, this again causes an overestimate of e/h. Although the value of e/h measured in this analysis pertains to the HEC as it will operate in ATLAS, care must be taken when comparing with other calorimeters.

Chapter 7

Conclusions

During the summer of 1999, 6 complete modules (3 front and 3 rear wheel modules), or 3/32 of the ATLAS Hadronic Endcap Calorimeter, were assembled and set in a beam test cryostat. This was the first time that production modules (modules which will be used in the construction of ATLAS) were tested and that the ATLAS cabling system were used. Some of these new electronic components, such as the Front End Boards, were not fully tested before the beam test and caused an increase of the electronic noise compare to previous years. The ATLAS calibration procedure was also followed for the first time.

The performance of the Hadronic Endcap Calorimeter is first evaluated using 10 to 193.1 GeV electron beams for five different impact positions. The response of the calorimeter is shown to be linear with energy within about one percent, and the electromagnetic constant is found to be $\alpha_{em} = (3.82 \pm 0.04)$ GeV/μA, which differs from previous measurements.

The intrinsic resolution (the resolution after eletronic noise subtraction) of the calorimeter to electrons is then measured to be

$$\frac{\sigma'}{E} = \frac{(23.29 \pm 0.09)\%}{\sqrt{E_0(\mathrm{GeV})}} \oplus (0.00 \pm 0.13)\%,$$

where E_0 is the initial particle energy, and E is the reconstructed energy. Furthermore, Monte Carlo simulations give an intrinsic resolution of

$$\frac{\sigma'}{E} = \frac{(20.7 \pm 0.4)\%}{\sqrt{E_0(\mathrm{GeV})}} \oplus (0.67 \pm 0.11)\%.$$

Calibration problems are observed when the spatial uniformity of the calorimeter is studied. The response of two adjoining cells is studied and a 2.4% difference is observed. The response is also shown to be reduced for impacts closer to tie-rods, which explains the discrepancy in α_{em} and resolution measured for such impact positions.

The performance of the Hadronic Endcap Calorimeter is then evaluate using 10 to 200 GeV pion beams for five different impact positions. The response is obtained using 54 cell clusters such that nearly full containment of hadronic showers is achieved. However, Monte Carlo simulations show that $(3.2 \pm 0.5)\%$ of the energy escapes, mainly at the bottom of the calorimeter. The intrinsic energy resolution (after electronic noise subtraction) of the calorimeter to pions is measured to be

$$\frac{\sigma'}{E} = \frac{(76.2 \pm 0.9)\%}{\sqrt{E_0(\mathrm{GeV})}} \oplus (6.68 \pm 0.09)\%,$$

whereas Monte Carlo simulation yields an intrinsic resolution of

$$\frac{\sigma'}{E} = \frac{(64.5 \pm 0.8)\%}{\sqrt{E_0(\mathrm{GeV})}} \oplus (5.51 \pm 0.1)\%.$$

Previous studies have shown that Monte Carlo simulations tend to give a better resolution [18].

The differences observed between the results obtained in this analysis and previous measurements, or results from Monte Carlo simulations, are mainly due to the calibration procedure not being adequate in 1999 which caused the response to be different from one readout cell to another. The treatment of non-Gaussian tails in this analysis may have led to an underestimate of the effective electronic noise.

Finally, a study of the ratio of electromagnetic to hadronic response, e/h, is done. The hadronic response is corrected for leakage using Monte Carlo simulation results. This correction is found to improve the agreement between the theoretical model and the data, and yields

$$e/h = 1.509 \pm 0.021.$$

Bibliography

[1] Glashow, S.L., "Partial Symmetries of Weak Interaction", *Nuclear Physics* (International), *Vol 22 No 4* (1961) 579-588.

[2] Weinberg, S., "A Model of Leptons", *Physical Review Letter* **19** (1967) 1264-1266.

[3] Salam, A., *Elementary Particle Theory*, N. Svartholm, ed. (Stockholm: Almquist and Wiksell, 1968).

[4] G. Arnison et al., *Phys. Lett.*, **1**22B, 103, 1983.

[5] M. Banner et al., "Observation of Single Isolated Electrons of High Transverse Momentum in Events with Missing Transverse Energy at the CERN $p\overline{p}$ Collider", *Phys. Lett.*, **1**22B, 476, 1983.

[6] G. Arnison et al., *Phys. Lett.*, **1**26B, 398, 1983.

[7] P. Bagnaia et al., "Evidence for $Z_0 \to e^+e^-$ at the CERN $p\overline{p}$ Collider", *Phys. Lett.*, **1**29B, 130, 1983.

[8] CDF Collaboration, *Physical Review Letters* **7**4 (1995) 2626.

[9] ATLAS Collaboration, "ATLAS Letter of Intent", CERN/LHCC/92-4, 1992.

[10] ATLAS Technical Proposal, CERN/LHC/94-43, 1994.

[11] LHC Collaboration, "LHC White Book", CERN/AC/93-03.

[12] LHC Collaboration, "LHC Conceptual Design Report", CERN/AC/95-05.

[13] The LHC Study Group, "Design Study of the Large Hadron Collider (LHC)", CERN/91-03, 2 May 1991.

[14] CMS Collaboration, "CMS Letter of Intent", CERN/LHCC/92-3, 1992.

[15] LHC-B Collaboration, "LHC-B Letter of Intent", CERN/LHCC/95-5, 1995.

[16] ALICE Collaboration, " Technical Proposal for A Large Ion Collider Experiment at the CERN LHC", CERN/LHCC/95-71, 1995.

[17] ATLAS Collaboration, "ATLAS detector and physics performance, Technical Design Report, Volume II", *CERN/LHCC/99-15*, 1999.

[18] ATLAS Collaboration, "ATLAS detector and physics performance, Technical Design Report, Volume I", *CERN/LHCC/99-15*, Chapter 1, 25 May 1999.

[19] ATLAS Collaboration, "Liquid Argon Calorimeter Technical Design Report", *CERN/LHCC/96-41*, 15 December 1996.

[20] ATLAS Collaboration, "Tile Calorimeter Technical Design Report", *CERN/LHCC/96-42*, 15 December 1996.

[21] D.E. Groom et al., "Review of Particle Physics", *The European Physical Journal*, **C15** (2000) 1.

[22] W.R. Nelson et al., "Electron-Induced Cascade Showers in Copper and Lead at 1 GeV, *Physical Review Vol 149* (1966), 201-208.

[23] Perkins, D., "Introduction to high energy physics, (3rd ed.), Addison-Wesley, 1987.

[24] Mockett, P.M., "A review of the physics and technology of high-energy calorimeter devices", *University of Washington*, 1983.

[25] Fabjan, C., " Calorimetry in high-energy physics", *Experimental Techniques in High Energy Physics*, Adison-Wesley, 1987.

[26] Wigmans, R., "On the energy resolution of uranium and other hadron calorimeters", *Nucl. Ins. Meth.*, **A259** (1987) 389-429.

[27] Particle Data Group, "Particle Physics Booklet", *European Physical Journal*, C3, 1998.

[28] Amaldi, U., "Fluctuations in calorimetry measurements", *Physica Scripta*, Vol. 23, pp. 409-424, 1981.

[29] W.J. Willis and V. Radeka, "Liquid Argon Ionization Chambers as Total Absorption Detectors", *Nucl. Inst. and Meth.*, Vol. 120 (1974) 221-236.

[30] ATLAS Collaboration, "Calorimeter performance, Technical Design Report", *CERN/LHCC 96-40*, January 1997.

[31] O'Neil, D., "Performance of the ATLAS Hadronic Endcap Calorimeter and The Physics of Electroweak Top Quark Production at ATLAS", Ph. D. Thesis, University of Victoria, 1999.

[32] Experimental Area Group, "Secondary Beamlines", information on the web at *http://sl.web.cern.ch/SL/eagroup/beams.html*

[33] Minaenko, A., "Analysis of August 99 TB data", Max-Plank-Institut für Physik, *HEC TB meeting*, December, 1999.

[34] Kurchaninov, L., "Electronics in TB-99, Max-Planck-Institut für Physik, *HEC/FCAL TB Analysis Meeting*, December, 1999.

[35] M. Lefebvre, D. O'Neil and C. Sbarra, "The hec_adc package Version 3.8", update of *ATLAS HEC-Note-069*, p.18, November 2, 1999.

[36] M. Dobbs, M. Lefebvre and D. O'Neil, "Pion and Electron Energy Scan Analysis from April 1998 Testbeam Data", *ATL-LARG-99-001*, January 27, 1999.

[37] Duboc, J., "A Pedagogical Experiment Using Bubble Chamber Pictures: WA73", *SPS/EBS/Note/81-5*, May 1981.

[38] W.E. Cleland and E.G. Stern, "Signal processing considerations for liquid ionization calorimeters in a high rate environment", *Nucl. Inst. and Meth.*, **A338** (1994) 467-497.

[39] A. Kiryunin and D. Salihgic, "Monte Carlo for the HEC Prototype: Software and Examples of Analysis", Max-Planck-Institut für Physik, *ATLAS HEC-Note-063*, November 25, 1998

[40] Kiryunin, A., "Test-Beam MC Simulation: Pions and Electrons", Max-Planck-Institut für Physik, *ATLAS HEC-Note-055*, September 24, 1998

[41] T.A. Gabriel and C. Zeitnitz, *Nucl. Inst. and Meth.*, **A349** (1987)

[42] L. Kurchaninov and P. Strizenec, "Calibration of TB-99 Data", Max-Planck-Institut für Physik, *HEC/FCAL TB Analysis Meeting*, December, 1999.

[43] Dobbs, M.A., "Performance of the ATLAS Hadronic Endcap Calorimeter in Particle Beams", University of Victoria, April, 1999.

[44] Schacht, P., in a private discussion.

[45] ATLAS Collaboration, "ATLAS detector and physics performance, Technical Design Report, Volume I", *CERN/LHCC/99-15*, pp. 11-16, 25 May 1999.

[46] Minaenko, A., "HEC: Electron and Pion results from June 2000", Max-Plank-Institut für Physik, *HEC/FCAL TB Meeting*, September 20th, 2000.

[47] Juste, A., "Analysis of the Hadronic Performance of the TILECAL Prototype Calorimeter and Comparison with Monte Carlo", ATLAS Internal note, *TILECAL-95-069*, 1995.

Appendix A

The Elementary Particles

In the Standard Model, there are three types of particles: the spin-$\frac{1}{2}$ fermions (leptons and quarks) that constitute all matter, the spin-1 gauge bosons that mediate the three forces, and the spin-0 Higgs boson. There are in total 12 fermions divided in 3 families (or generations) as can be seen in Table A.1. The u, c, and t quarks carry a charge of $\frac{2}{3}e$ each; whereas the d, s, and b are quarks with an electrical charge of $-\frac{1}{3}e$. The e, μ, and τ are charged leptons, whereas all of the neutrinos (ν_e, ν_μ and ν_τ) are electrically neutral. Each of these particle has an antiparticle.

Both leptons and quarks can interact via the electroweak force which is mediated by the vector bosons (γ, $W^{\pm}$, Z^0). Leptons do not feel the strong force which acts only on quarks that carry one of three charge values called "colour". The strong force is mediated by the exchange of coloured gluons (g), which binds quarks to produce colourless particles called hadrons. Quarks can therefore combine in two different ways to preserve the colourless. A quark can combine with an antiquark to produce integer spin particles called mesons, such as the π^+ ($u\overline{d}$) and the π^- ($\overline{u}d$).

Families	1st	2nd	3rd
Quarks	u	c	t
	d	s	b
Leptons	e	μ	τ
	ν_e	ν_μ	ν_τ

Table A.1: The three fermion families.

Bosons	Force mediated
γ	Electromagnetic
Z^0	Neutral weak
$W^{\pm}$	Charged weak
g	Strong

Table A.2: The vector gauge bosons.

It is also possible for three quarks (or antiquarks) to combine and form an half-integer spin particle called baryons, such as the proton (uud) and neutron (udd). A summary of the vector bosons and the force they mediate is presented in Table A.2.

Appendix B

Layout Geometry of the HEC Readout Cells

The following figures display the geometric layout of the readout cells for the calorimeter. Figure B.1 show the distribution of the readout cells for the second depth (z=2) of the front wheel modules. The layout for the first depth (z=1) was presented in Figure 4.1. The distributions of the readout cells for the rear wheel modules (third and fourth depth) are shown in Figure B.2.

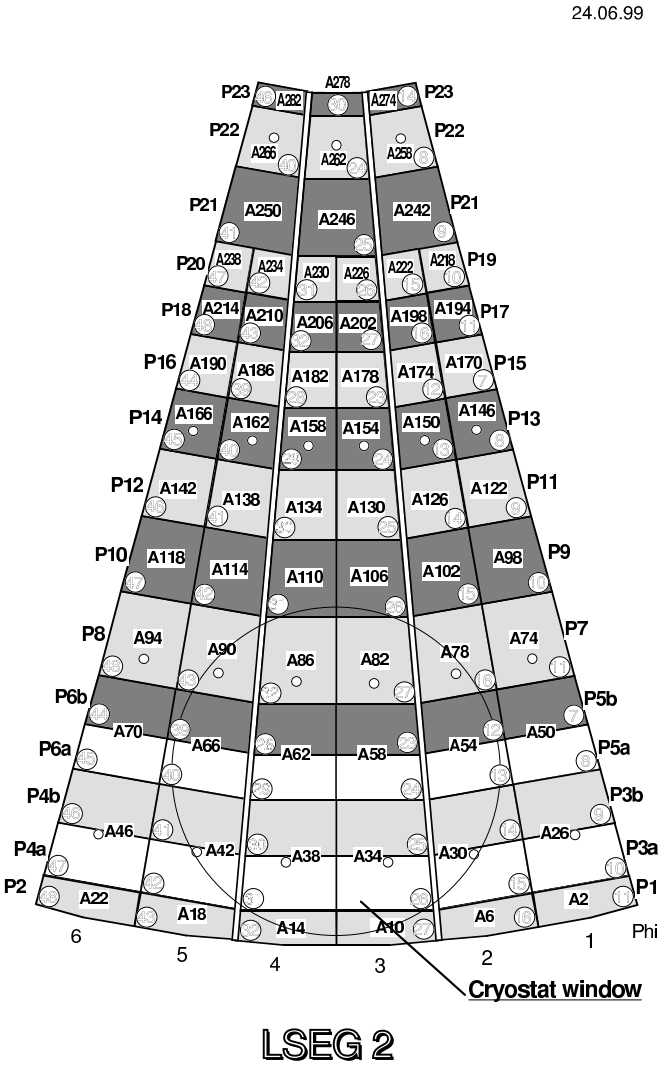

Figure B.1: The geometric layout of the readout cells for the second depth of the front wheel modules (z=2). The beam enters in a direction perpendicular to the surface shown, in a region behind the cryostat window. The numbers appearing in the squares and preceded by an "A" are identifying the channels used for the readout cells; the circled numbers are identifying the channels from the calibration generator.

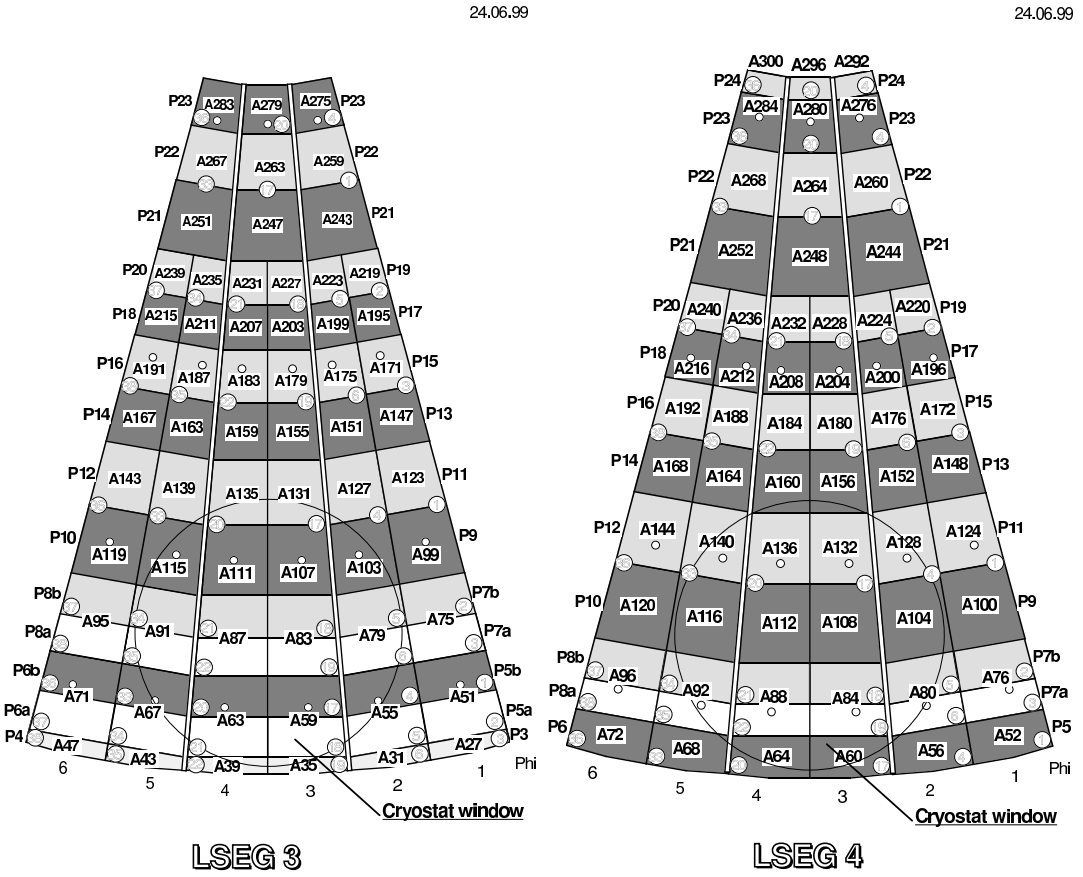

Figure B.2: The geometric layout of the readout cells for the rear wheel modules (z=3 and z=4). The beam enters in a direction perpendicular to the surface shown, in a region behind the cryostat window. The numbers appearing in the squares and preceded by an "A" are identifying the channels used for the readout cells; the circled numbers are identifying the channels from the calibration generator.

Appendix C

Error Analysis for the Intrinsic Energy Resolution

The formula for error expansion are summarized here. They were used in the calculation of the HEC intrinsic energy resolution, $r = \sigma'/E$, to electrons and pions (see Sections 5.5 and 6.4).

In order to extract the intrinsic resolution, the electronic noise, σ_n, is subtracted out in quadrature from the width of the response, σ,

$$\sigma' = \sigma \ominus \sigma_n = \sqrt{\sigma^2 - {\sigma_n}^2}, \tag{C.1}$$

such that the error on σ' is

$$(\Delta\sigma')^2 = \left(\frac{\sigma}{\sigma'}\right)^2 (\Delta\sigma)^2 + \left(\frac{\sigma_n}{\sigma'}\right)^2 (\Delta\sigma_n)^2. \tag{C.2}$$

The error on σ is purely statistical and originates from the Gaussian fit performed on the response, whereas the error on σ_n includes both the statistic and systematic error [1]. Similarly, the HEC cluster response to electrons and pions was corrected for the cluster most probable current observed in the noise distribution (Sections 5.3 and 6.3). The corrected response, E, is

$$E = \mu_E - \mu_n, \tag{C.3}$$

[1] The systematic errors on σ_n and μ_n are estimated as the difference between the best asymmetric fit obtained and the values obtained from a Gaussian fit performed in the region $\pm 2\sigma$ about the most probable current (see Section 4.3). The total error on σ_n and μ_n is the quadratic sum of this systematic and the stastical error.

where μ_E and μ_n are the cluster response and cluster noise most probable current, respectively. The error on μ_n includes both the statistical and systematic error. Therefore, the error on E is

$$(\Delta E)^2 = (\Delta\mu_E)^2 + (\Delta\mu_n)^2. \tag{C.4}$$

Using all of the above results, the error on the intrinsic resolution is then

$$\left(\frac{\Delta r}{r}\right)^2 = \left(\frac{\Delta\sigma'}{\sigma'}\right)^2 + \left(\frac{\Delta E}{E}\right)^2. \tag{C.5}$$

VITA

Surname:	Fortin
Given Names:	Dominique
Place of Birth:	Montréal, Québec
Date of Birth:	January 29, 1975

Educational Institutions Attended:

McGill University	1995-1998
University of Victoria	1998-2000

Degrees Awarded:

B.Sc. (Physics) McGill University	1998

Honours and Awards:

Fonds pour la Formation de Chercheurs et d'Aide à la recherche (FCAR) Scholarship	1998-2000
R.E. Powell Scholarship	1995-1998
Golden Key National Honour Society Membership	1996

Partial Copyright License

I hereby grant the right to lend my thesis to users of the University of Victoria Library, and to make single copies only for such users, or in response to a request from the Library of any other university or similar institution, on its behalf or for one of its users. I further agree that permission for extensive copying of this thesis for scholarly purposes may be granted by me or a member of the University designated by me. It is understood that copying or publication of this thesis for financial gain shall not be allowed without my written permission.

Title of Thesis:

Performance of the ATLAS Hadronic Endcap Calorimeter Modules to Electrons and Pions

Author: _____

Dominique Fortin

December 11, 2000